PROCEEDING OF INTERNATIONAL MECHANCIAL ENGINEERING CONFERENCE -2019

A METICULIOUS APPROACH FOR SELECTION OF AIRFOILS TO PREPARE A BLENDED WING BODY AIRCRAFT

Qais H. Suhail, H. Nayyer, J. Younus, K. Kamal
Engineering Sciences Department, National University of Sciences & Technology (NUST)
Karachi, Pakistan

Tel. +92346-2658855
E-mail Address: qaishassansuhail@gmail.com

ABSTRACT

The concept of Blended Wing Body is not new; NASA has been working on this concept for more than 20 years and many researchers have encouraged its feasibility and efficiency, yet there's much room of research still present in this novel concept. One of the key features of Blended Wing Body is its tail-less delta wing design. Removing the tail brings many advantages to the table, but it comes at a price of reduced stability along-with difficulties in pitch-control and directional control. This paper would focus on circumventing this inherent problem with the tail-less delta for small scaled RC models by employing hybrid aerofoils; one for the central body and one for the outer wing body. Analysis of potential airfoils for the blended wing body design was carried out on XFLR5 and their results were compared to obtain the optimum airfoil as per the design requirement. From the plethora of available airfoils, 6 airfoils were shortlisted for central body and 7 for outer wing section. A hybrid technique was used, as it is relatively simpler yet reliable approach in choosing the aerofoils. The aerofoils were finalized after performing an analysis a CFD Analysis in ANSYS Fluent

Keywords—CFD, Blended Wing Body (BWB), Airfoil, Tail-less Aircraft.

1 INTRODUCTION

The conventional aircrafts with a tubed fuselage, which we are so accustomed to see in the skies, hardly had any changes in their design. The tube fuselage design has been conspicuously same for the past 40 years and now it seems to have reached its capacity zenith [1]. In this dynamic age of aviation, where the hunger for improvement is insatiable and air-traffic increasing at an astounding rate, this design would soon prove to be an anachronism in the decades to come. That being said, aviation industry needs a paradigm shift in the aircraft design which will radically change the output of aircrafts in the years to come [2].

To address this issue, NASA Research Centre funded a project to design an aircraft that would carry 800 passengers over a 7000-mile range in the subsonic region with Mach=0.85 [3]. Advanced technologies were used, and a composite structure was incorporated to design the airframe. The new design was compared with conventional configuration aircrafts and the results were astonishing and beyond expectations. This ground-breaking design is known as the Blended Wing Body. Feasibility and effectiveness of BWB concept have already been studied and published by many authors [4]

BWB is a novel concept and its innovative design sets it apart from its conventional tube and wing counterparts. The BWB structure consists of wings integrated seamlessly with a non-cylindrical section, which translates into a single lift generating body. This unique design does not incorporate the tail-assembly and the engines are placed at the aft end hence control is governed by control surfaces such as rudders and elevons installed at various locations on the aircraft body resulting in a less complex design and significant reduction in drag and weight.

However, the concept of BWB for small scaled planes and RC models hasn't been studied much despite of their tremendous advantages, this paper presents an effective approach for selecting the right airfoils for small scaled RC models on BWB concept. Section II covers the advantages of BWB aircrafts, section III and IV presents the nomenclature and technical details of an airfoil, in

section V we decide the constraints for shortlisting the aerofoils and further sections includes the analysis and results of selected airfoils.

2 ADVANTAGES OF A BLENDED WING BODY

2.1 Higher Lift-Drag Ratio

The empennage in a blended wing body aircraft is removed, rendering the aircraft tail-less. This tail-less design significantly reduces the interference drag because of the absence of tail and its associated drag [3].

2.2 Increased Payload

As the whole airframe of the Blended Wing Body is blended into a single structure and all of it is responsible for generating lift, almost the whole aircraft can be used for payload. This remarkably increases the payload of a BWB aircraft. A recent study shows that a sustainable double decker Blended Wing Body aircraft can be made to carry more than 800 passengers [3].

2.3 Noise Mitigation

The blended wing body design offers a low acoustic profile without any sound treatment. Because of the presence of aft mounted engines, the forward radiated fan noise is offset by the vast center body and the engine exhaust noise is not reflected by the lower surface of the wing.[5]

2.4 Fuel Economy

Due to the less aerodynamic drag and improved design, the engines of a blended wing body burn less fuel per seat per mile. This puts BWB aircrafts at a distinct cost advantage over conventional aircrafts. According to a research, BWB aircrafts burn 27 % less fuel compared to conventional aircrafts. [3].

2.5 Lower Emissions

Even a small reduction in fuel consumption drastically reduces yearly CO2 and NOx emissions in the skies. Since BWB aircrafts burn 27 % less fuel, they also help in reducing the influx of noxious emissions into our environment. According to a study, BWB technology can help to reduce the carbon emissions in the sky by 50 %. [5]

3 NOMENCLATURE OF AIRFOIL

Most aircraft manufacturers design their own customized airfoils according to their requirements;

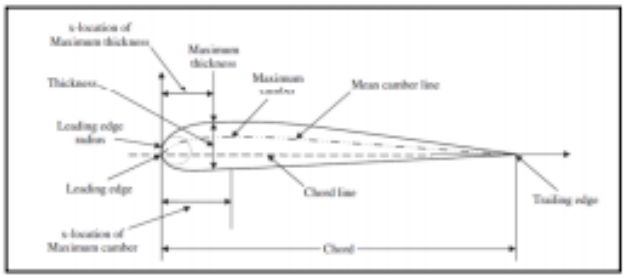

Figure 1 Nomenclature of an Aerofoil

however, this process is quite complex and require in-depth knowledge of the fundamentals of aerodynamics accompanied by wind tunnel tests [6]. Therefore, it is wiser to choose airfoils from the wide array of pre-designed airfoils available. The most widely used airfoil series were designed by National Advisory Committee for Aeronautics (NACA) in the 1900s. These standard airfoils are still widely used today since they are based on an established nomenclature. Other lesser known airfoils series include Martin Heppler (MH) aerofoils which are mostly used in Delta Wing aircrafts. [7] A typical airfoil section is shown in Fig 1. [6]

The most prominent feature of an airfoil is the mean camber line which is the nexus of points halfway between the upper and lower surfaces. The distance from the leading edge to the trailing edge is known as the chord and camber is the maximum distance between the mean camber and the chord. These parameters along with the thickness govern the flight characteristics and hence, choosing aerofoils with the appropriate parameters is vital in aircraft design. [7]

4 AERODYNAMIC COEFFICIENTS

The coefficient of lift (CL), drag (CD) and moment (CM) are dimensionless variables which aid in dimensional analysis. These coefficients depend on the angle of attack, Reynolds's number and the Mach number. Since the scope of this project lies in the subsonic speed range therefore, the role of Mach number is inconsequential [7]. To improve the aerodynamic efficiency the aerofoil should generate

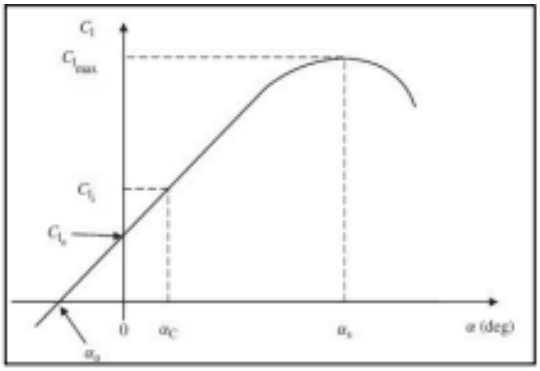

Figure 2 Co-efficient of Lift vs Angle of Attack

maximum lift at certain angle of attacks without stalling, reduce drag to a minimum and ensure that pitching moments remain close or equal to zero, so the flight can be stable. However, in some cases a negative pitching moment is acceptable as it offsets the effects of a disturbance to the angle of attack due to some external factors and provides stability to the airfoil [6]. The most important parameter on which the overall aerodynamic efficiency depends is the lift-to-drag ratio. [7] The variation of these coefficients with the angle of attack plays a vital role in the airfoil selection process and the key relationships are depicted in the Fig.2-5 which were obtained after several wind tunnel tests as said by Sadraey. [6]

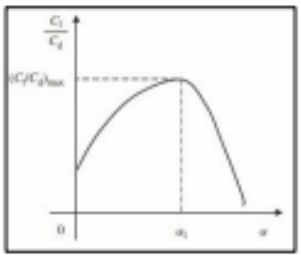

Figure 3 Efficiency vs Angle of Attack

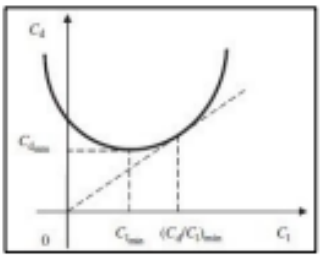

Figure 4 Cd vs Cl

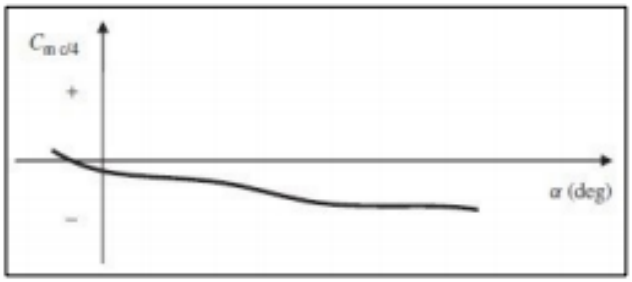

Figure 5 Cm vs Angle of Attack

5 CONSTRAINTS

Coping up with the aerodynamics of a tail-less aircraft like Blended Wing Body is much more complicated than dealing with the aerodynamics of a conventional aircraft. Absence of vertical and horizontal stabilizers, and empennage at the far back end of aircraft creates difficulties with stability, pitch control and directional control; where pitch control is the biggest cause of instability and should be taken care of. [8]. To counteract the effect generated due to the absence of a tail and to produce static longitudinal stability, center of gravity of the plane must be located ahead of the center of pressure and the aerodynamic moments (CM) must be kept minimum. [7], but keeping the aerodynamic moment (CM) low will restrict the aircraft's co-efficient of Lift (CL), as both of them are inversely related [8]. Hence a design trade off must be made between the two, which gives us our first constraint for shortlisting the airfoils.

In BWB, load is concentrated in the center body and wings have control surfaces to maneuver the aircraft [9], which implies that high lift is required by the central body while wings should have more stability. Hence following the hybrid approach is easier that is, selecting two airfoils, one for the central body and one for wings, with high CL and minimum CM for center body and with positive CM for wings to counterbalance the effect generated by center body. [10]. Many airfoils were analyzed in XFLR5, and it was realized that NACA 5 digits' series has very low CM and moderate CL, hence suitable for center body, and Reflexed camber airfoils have higher longitudinal stability and can be shortlisted for outer wing section.

Another constraint of thickness for central body was added. Small RC BWB aircraft should have enough space to accommodate its internal components and must have enough structural strength while maintaining the aerodynamic integrity [11]. A thickness of 11% of root chord was chosen after doing market surveys and analyzing common RC planes model.

6 SHORTLISTED AIRFOILS

Out of many aerofoils which were analysed, 6 aerofoils were shortlisted for central body and 7 for outer wing section, as shown in Table 1, these aerofoils will be further analysed. Note that all these aerofoils have good potential to be used in other BWB models, most feasible of them, according to our requirements, will be selected in this paper.

Table 1 Shortlisted Airfoils

For Central Body	For Outer Wing
a. NACA 25111	a. EPPLER 635
b. NACA 44111	b. ESA 40
c. NACA 55111	c. LA 2573A
d. NACA 64111	d. MH 45
e. MH 60	e. MH 78
f. HS 522	f. MH 80
	g. S5010

Analysis were carried out in XFLR5 at 1 × 106 Reynolds's number and 0.00 Mach number. Variations in aerodynamic co-efficient, CL, CM and CL/CD for Angle of Attack ($0^o \leq \alpha \leq 10^o$) are shown in the Fig. 6-11 for both, central and outer wing body. For Centre Body, results of variation of CL, CM and CL/CM with respect to Alpha are summarized in Table 2 and for outer body in Table 3.

As discussed, we need an airfoil with high CL and minimum CM for central body of our aircraft. It is obvious from Table 2 data that NACA 64111 has the highest CL and CM close to zero.

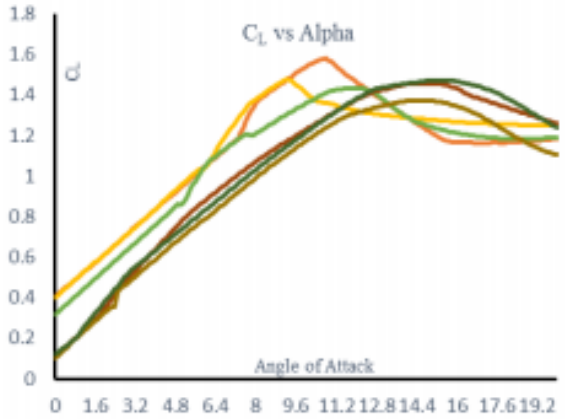

Figure 7 C_L vs Alpha for Central Body Airfoils

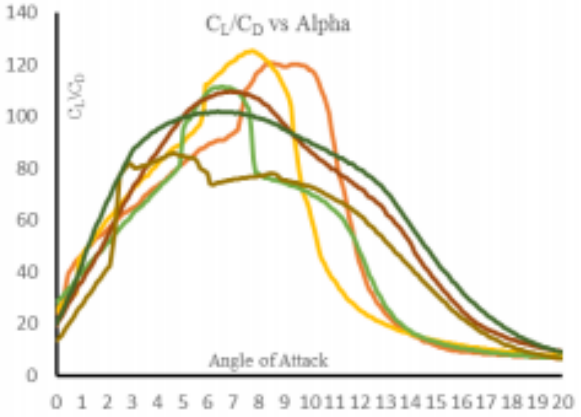

Figure 6 C_L/C_D vs Alpha for Central Body Airfoils

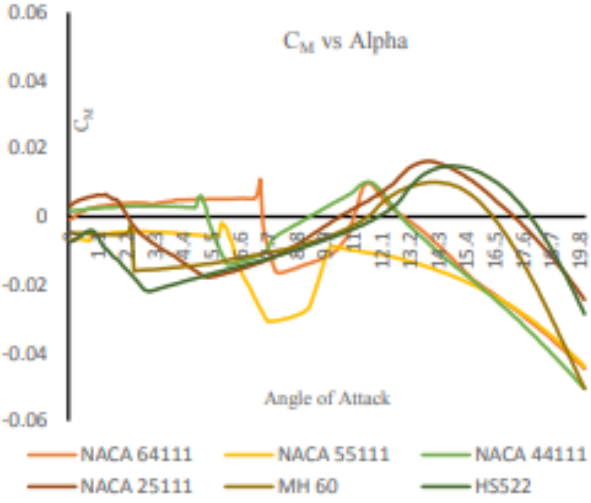

Figure 8 C_M vs Alpha for Central Body Airfoils

Table 2 Results for Central Body

Name of Aerofoil	C_L (at $\alpha = 5^\circ$)	C_L max	Average C_M ($0^\circ \leq \alpha \leq 10^\circ$)	C_L/C_D Max (Max Efficiency)
NACA 25111	0.77	1.45	-0.0074	109
NACA 44111	0.85	1.43	-0.0014	111
NACA 55111	0.94	1.47	-0.0121	125
NACA 64111	0.94	1.57	-0.0003	120
MH 60	0.69	1.37	-0.0103	86
HS 522	0.73	1.47	-0.0135	102

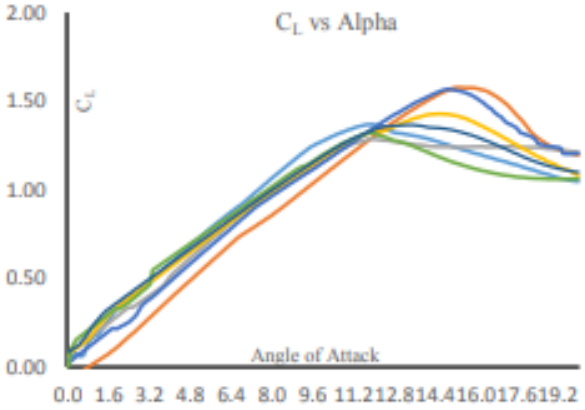

Figure 10 C_L vs Alpha for Outer Section

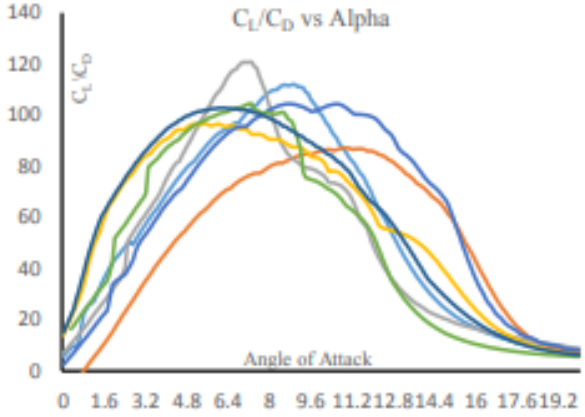

Figure 11 C_L/C_D vs Alpha for Outer Section

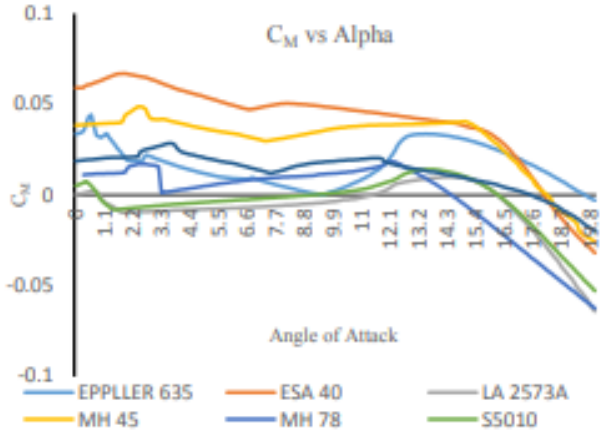

Figure 9 C_M vs Alpha for Outer Wing

Results for Outer wing are summarized in Table 3. Here, airfoil for outer wing should counter balance the moment created by root airfoil and effects of absence of empennage yet having good efficiency and co-efficient of lift. ESA 40 has the highest CM but lowest efficiency whereas MH 78 has high CM and efficiency.

Table 3 Results for Outer Body

Name of Aerofoil	C_L (at $\alpha = 5^\circ$)	C_L max	Average C_M ($0^\circ \leq \alpha \leq 10^\circ$)	C_L/C_D Max (Max Efficiency)
EPPLER 635	0.71	1.36	0.0145	112
ESA 40	0.51	1.57	0.0556	87
LA 2573A	0.64	1.28	0.0194	121
MH 45	0.67	1.42	-0.0061	97
MH 78	0.61	1.56	0.0370	105
MH 80	0.71	1.32	0.0094	104
S5010	0.68	1.36	-0.0026	103

7 CFD ANALYSIS OF NACA 64111 AND MH 78

NACA 64111 shown in Fig. 12 was selected for center body and MH 78 shown in Fig. 13 for outer wing body.

A two-dimensional Laminar Flow CFD analysis of both the airfoils was carried out in ANSYS Fluent to determine the lift and drag more accurately. Quadrilateral C-type mesh was generated because of non-symmetric geometry of the airfoils; airfoils

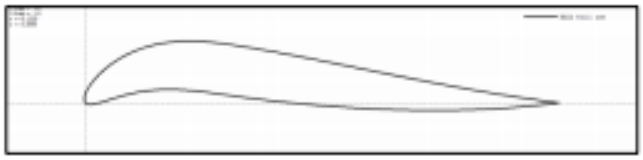

Figure 12 Geometry of NACA 64111

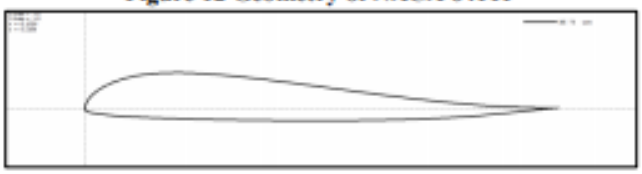

Figure 13 Geometry of MH 78

were analyzed in the laminar flow at a velocity of 30 m/s and lift and drag forces along with the static pressure contours were calculated at zero angle of attack (α).

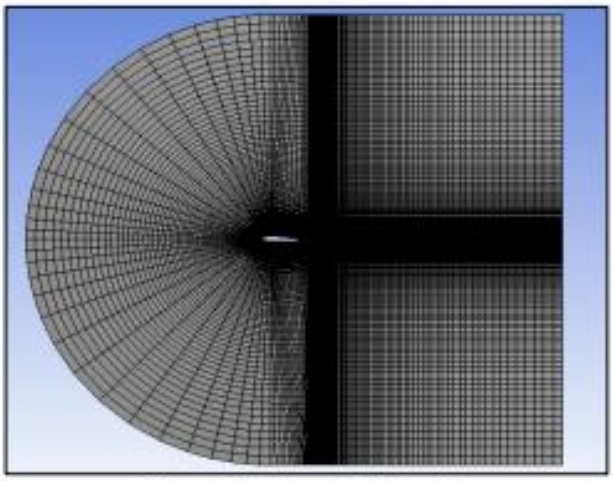

Figure 14 C-Type Mesh Quality

Fig. 14 show the quality of fine C-type quadrilateral mesh which was used, Fig. 15 and Fig. 16 show the static pressure contour for NACA 64111 and MH 78 respectively, which shows that stagnation pressure in both the airfoils is maximum at the leading edge and the pressure over the center body is negative hence contributing to the lift generated, it should also be noted that pressure is more negative for NACA 64111 as it's producing more lift.

Table 4 shows the amount of lift and drag generated for both the aerofoils in Newton.

Table 4

Aerofoil Name	Lift (N)	Drag (N)
NACA 64111	270.81	32.67
MH 78	43.65	8.20

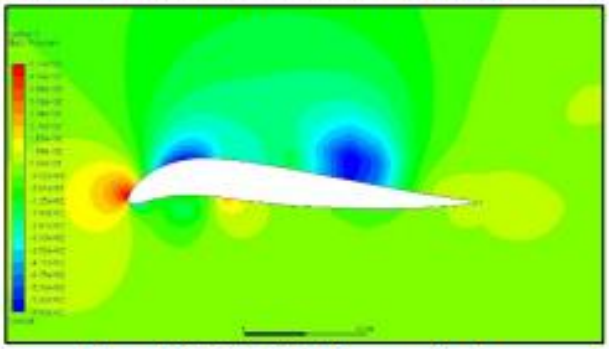

Figure 16 NACA 64111 Pressure Contours

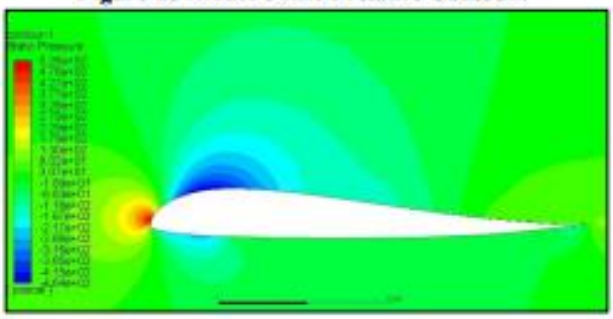

Figure 17 MH 78 Pressure Contours

8 CONCLUSION

Shortlisting aerofoils for a blended wing body aircraft is a challenging task because of the stability restrictions. A hybrid technique was used, as it is relatively simpler yet sturdy approach in choosing the airfoils, as said by Goodman [10]. Using this criterion, airfoil selection was easily clarified, i.e. high lift with minimum moment for center body and high moment with maximum possible lift for outer wing. NACA 64111 and MH 78 were finalized for root and wing airfoils, respectively, after performing analysis in XFLR5. Both the airfoils were then further analyzed using CFD in ANSYS Fluent, thus making the research in this paper highly accurate and efficient. A 3D model based on the selected airfoils is shown in Fig. 17. Design calculation and 3D modelling of is beyond the scope of this paper and an image of 3D model is included for visual purposes only.

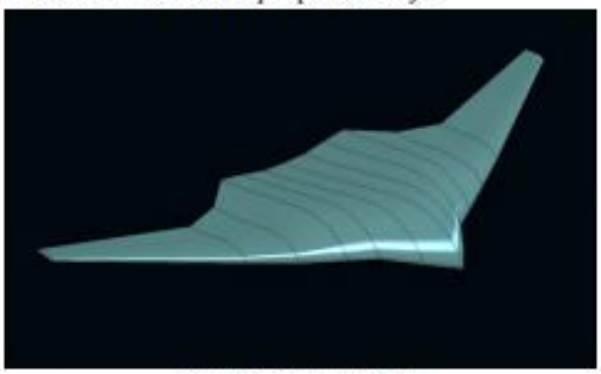

Figure 15 Future Work

REFERENCES

[1] "Boeing Commercial Airplanes." Current Market Outlook 2013-2032. USA. 2013.

[2] "Airbus. Global Market Forecast 2007-2026." Blagnac, France., 2008.

[3] R. H. Libeck, "Design of the Blended Wing Body Subsonic Transport," JAC, 2004.
[4] R. M. Martinez, "Design and analysis of the control and stability of a Blended Wing Body aircraft," Polytechnic University of Madrid (UPM), 2015.
[5] M. Marino, "BENEFITS OF THE BLENDED WING BODY AIRCRAFT COMPARED TO CURRENT AIRLINERS.," ISSA, 2015.
[6] M. H. Sadraey, AIRCRAFT DESIGN A Systems Engineering Approach.
[7] J. D. Anderson, AIRCRAFT PERFORMANCE AND DESIGN, TATA McGraw-Hill. 2010.
[8] "Thompson - 2011 - The Design and Construction of a Blended Wing Body.pdf.".
[9] S. H. Cho, "BWB MILITARY CARGO TRANSPORT FUSELAGE DESIGN AND ANALYSIS," presented at the INTERNATIONAL CONGRESS OF THE AERONAUTICAL SCIENCES, 2008.
[10] G. Alexander S, "Conceptual Aerodynamic Design of Delta-type Tailless Unmanned Aircraft," IJUSEng, 2014.
[11] A. Baig, "A New Methodology for Aerodynamic Design and Analysis of a small scale Blended Wing Body," AAE, 2018.

ANALYSIS OF EXPERIMENTAL AND NUMERICAL SIMULATION OF VARIOUS NACA SERIES AIRFOILS

Bilal Ahmed[1,*] Ateeque Ahmed[1], Nasiruddin Shaikh[1], Muhammad Waseem[2], Abdul Fatah[3], Dur Muhammad[3]

[1]Department of Mechanical Engineering, NED University of Engineering & Technology, Karachi, Pakistan

[2]School of Engineering, Computer & Mathematical Sciences, AUT University, Auckland, New Zealand

[3]Mechanical Engineering Department, Mehran University of Engineering & Technology, Jamshoro, Pakistan

[*]Corresponding author. Tel.: +92-332-3964756

E-mail address: 12me76@student.muet.edu.pk

ABSTRACT

In this work NACA series airfoils have been modelled and simulated and then are compared with the experimental results of the subsonic wind tunnel. The airfoils selected in this work are NACA 4412, NACA 2412 and NACA 0012. Experimental work has been performed on subsonic wind tunnel at Aerodynamics laboratory Mechanical Engineering Department MUET Jamshoro. ANSYS Fluent 15.0 has been used for modelling and simulation purpose and turbulence model used is Spalart Allmaras. The lift and drag coefficient are studied at 2° angle of attack and for validation purpose, numerical simulations results are compared with experimental results.

Keywords: NACA Series, Angle of attack, ANSYS, Subsonic wind tunnel

1 INTRODUCTION

Airfoil profile is the important parameter for wing design because wing efficiency increases depending on the airfoil profile, so there are a lot of studies over the airfoil profile as numerical and experimental in the literature. The coefficient of lift and drag helps in designing the airfoils and in understanding flow characteristics. Generally, a lot of investigators studied lift and drag performances of NACA airfoil. Bhat et al., studied oscillating of NACA 0012 airfoils at around stall angle at low Reynolds number [1]. Benard et al., have investigated the enhancement of airfoil performance by using a plasma actuator in steady and unsteady models [2]. Yao et al., have computed aerodynamic performance analysis of NACA0018 wind turbine airfoil by using numerical simulation method. The authors investigated lift, drag performances and surface pressure by changing attack angle using different turbulence model [3]. Lianbing et al. have investigated the performance of wind turbine NACA0012 airfoil using FLUENT programs. Spalart Allmaras turbulence model to numerical solutions was used by Lianbing et al. of the airfoil at 3×10^6 Reynolds number for lift and drag performance and stall angle [4]. Villalpando et al. studied over NACA 63-415 airfoil profile. They used different turbulence model in FLUENT and they saw that SA (Spalart Allmaras) model was better than others models. Also, they investigated aerodynamics of airfoil at low and high angles of attack [5]. Izzet et al. studied the lift and drag performances of NACA 0015 and they investigated that drag and lift coefficient increased with increasing angle of attack. [6]. In this work, the lift and drag coefficient are studied at 2° angle of attack of NACA 4412, NACA 2412 and NACA 0012. The experimental work has been performed on subsonic wind tunnel at Aerodynamics laboratory Mechanical Engineering Department MUET Jamshoro. ANSYS Fluent 15.0 has been used for modelling and simulation purpose and turbulence model used is SA (Spalart Allmaras).

2 EXPERIMENTAL SETUP

Three airfoils namely NACA 4412, NACA 2412 and NACA 0012 are being tested in subsonic wind tunnel placed at Aerodynamics laboratory Mechanical Engineering Department MUET Jamshoro. The airfoil is mounted in the test section as can be seen in fig. 1. For air flow to be straight

over airfoil the reference point is set first of all then angle of attack is set to 2°. The air flow speed is fixed to 20 m/s to monitor the different parameters of airfoils such as CL and CD. The wind tunnel is integrated with the computer to monitor all these parameters. The results are shown below in Table 1.

Fig. 1: Shows airfoil mounted in the test section

Table 1. Shows Lift and Drag co-efficient Results

S.No.	Airfoils	C_L	C_D
1	NACA 4412	0.21	0.07
2	NACA 2412	0.39	0.025
3	NACA 0012	0.31	0.0138

3 NUMERICAL SIMULATION

ANSYS Fluent 15.0 has been used for modelling and simulation purpose. The simulation steps are designing of geometry, meshing and solution of the model. The geometry has been designed on ANSYS fluent design modeller. The turbulence model used in this study is SA (Spalart Allmaras). SA is one equation model that solves an empirical transport equation for the eddy viscosity $\tilde{\upsilon}$. The transport equation for $\tilde{\upsilon}$ is

$$\frac{\partial}{\partial t}(\rho\tilde{\nu}) + \frac{\partial}{\partial x_i}(\rho\tilde{\nu}\tilde{u}_i) = G_\nu + \frac{1}{\sigma_{\tilde{\nu}}}\left[\frac{\partial}{\partial x_j}\left\{(\mu+\rho\tilde{\nu})\frac{\partial\tilde{\nu}}{\partial x_j}\right\} + C_{b2}\rho\left(\frac{\partial\tilde{\nu}}{\partial x_j}\right)^2\right] - Y_\nu + S_\nu \quad (1)$$

The production and destruction terms, G_ν and Y_ν, respectively, are defined as follows:

$$G_\nu = C_{b1}\rho\left(S + \frac{\tilde{\nu}}{k^2 y^2} f_{\nu_2}\right)\tilde{\nu}, \quad (2)$$

$$Y_\nu = C_{w1}\rho f_w \left(\frac{\tilde{\nu}}{y}\right)^2, \quad (3)$$

Where S is the mean strain rate, y is the wall distance and f_{ν_2} and f_w are damping functions. The constant values are $C_{b1} = 0.1355$, $C_{b2} = 0.622$, and $\tilde{\nu} = 2/3$.

The SA model is able to resolve the viscous sublayer when the mesh is fine enough near the walls. The mesh around airfoil for NACA 4412 is shown in fig. 2, for NACA 2412 is shown in fig. 3 and for NACA 0012 is shown in fig. 4.

Fig. 2: Mesh around NACA 4412 airfoil

Fig. 3: Mesh around NACA 2412 airfoil

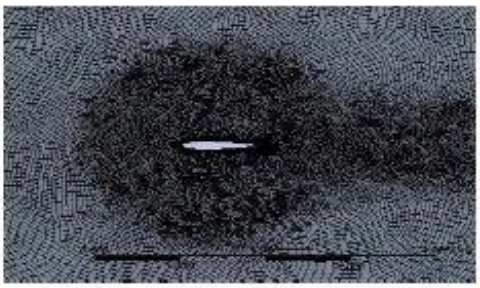

Fig. 4: Mesh around NACA 0012 airfoil

Mesh independent study was performed to verify that solution will not change with subsequent additional refinements and table 2 shows the grids number that was suitable for our models.

Table 2: Grids Number

S.No.	Airfoils	Grids Number
1	NACA 4412	226607
2	NACA 2412	208768
3	NACA 0012	107119

4 RESULTS AND DISCUSSION

In this study experimental and numerical analysis was performed for various NACA Series airfoils. The lift and drag co-efficient were calculated for various NACA series airfoil at 20 m/s wind velocity and 2° degree angle of attack experimentally by subsonic wind tunnel placed at Aerodynamics laboratory Mechanical engineering department MUET Jamshoro. Also lift and drag co-efficient were obtained numerically with ANSYS Fluent 15.0 for same conditions.

SA (Spalart Allmaras) turbulence model was used in this work. The 1000 iterations were given to all airfoils and for NACA 4412 the solution was converged at 668 iterations, for NACA 2412 the solution was converged at 545 iterations and for NACA 0012 the solution was converged at 780 iterations. The lift and drag coefficient that were obtained experimentally are shown in table 1 and numerical results are shown in table 3.

Table 3. Numerical results for lift and drag coefficient

S.No.	Airfoils	C_L	C_D
1	NACA 4412	0.16	0.065
2	NACA 2412	0.375	0.021
3	NACA 0012	0.37	0.0125

The velocity and pressure contours for NACA 4412, NACA 2412 and NACA 0012 are shown in fig. 5, 6, and 7.

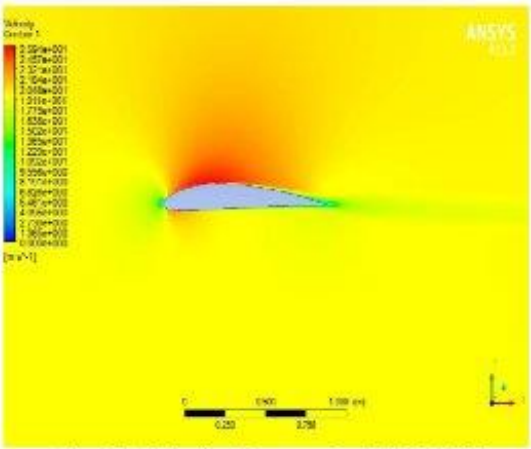

Fig. 5a. Velocity Contours for NACA 4412

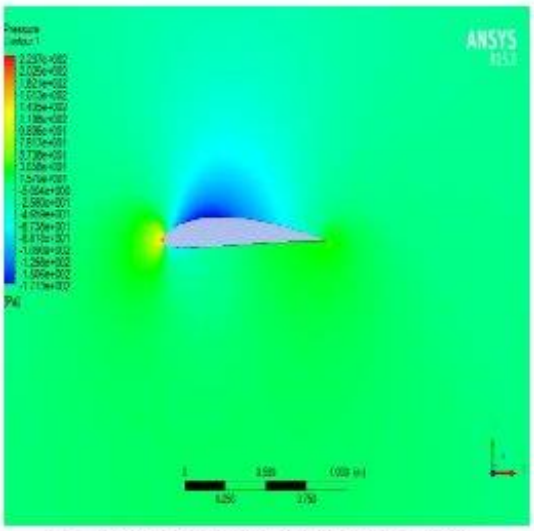

Fig. 5b. Pressure Contours for NACA 4412

Fig. 5a shows the velocity contours, the red colour shows that velocity is high on the upper camber surface. Fig. 5b shows the pressure contours, the blue colour represents low pressure on the upper camber surface. Fig. 6a shows velocity contours, the red colour shows that velocity is high at the upper and lower camber surface. Fig. 6b shows the pressure contours, the blue colour represents low pressure at upper and lower camber surface while pressure is high at the leading edge of airfoil represented by red colour.

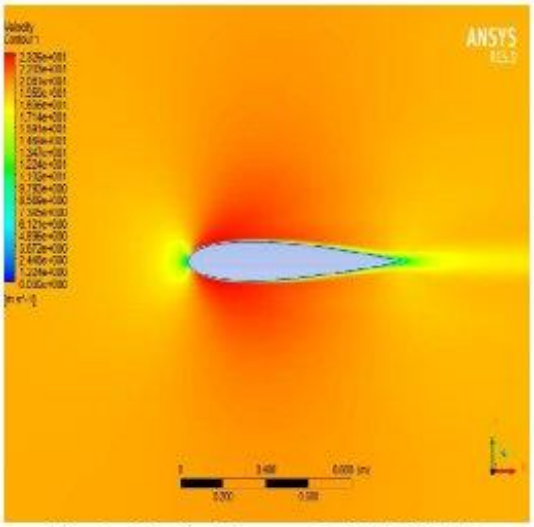

Fig. 6a. Velocity Contours for NACA 2412

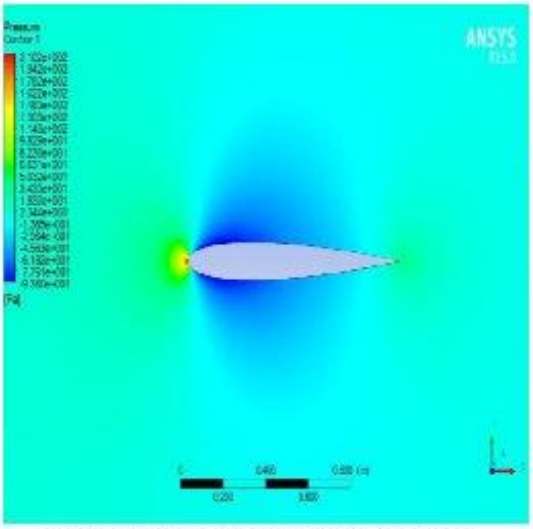

Fig. 6b. Pressure Contours for NACA 2412

Fig. 7a shows the velocity contours, the velocity is high at upper and lower camber surface as represented by red colour. Fig. 7b shows the pressure contours, the pressure is low at upper and lower camber surface as represented by blue colour while pressure is high at the leading edge of the airfoil.

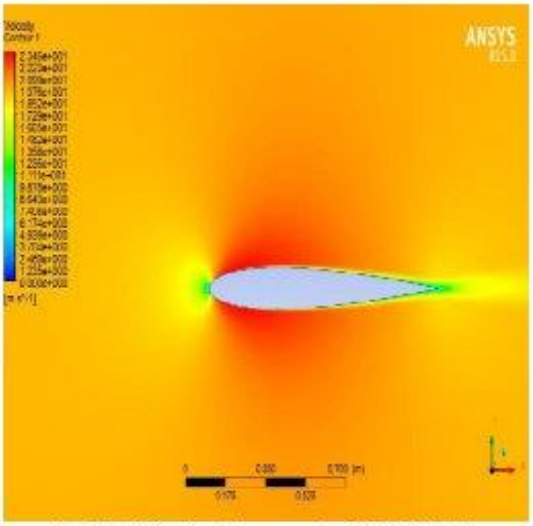

Fig. 7a. Velocity Contours for NACA 0012

The percentage of error between experimental and numerical results is shown in table 4 for coefficient of lift and drag.

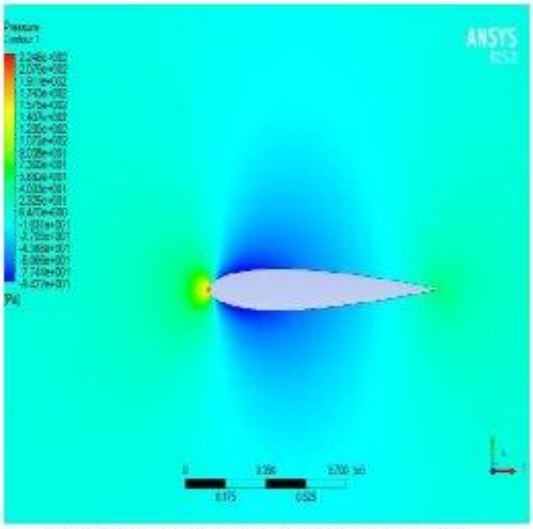

Fig. 7b. Pressure Contours for NACA 0012

Table 4. Percentage Error for various airfoils

Airfoils	% Error for C_L	% Error for C_D
NACA 4412	31.25 %	7.69 %
NACA 2412	4%	19%
NACA 0012	16.2%	10.4%

The percentage of error is maximum for lift coefficient of NACA 4412 whereas the percentage of error is maximum for drag coefficient of NACA 2412.

5 CONCLUSION

In this study, the lift and drag coefficient for various NACA series airfoils were calculated experimentally using subsonic wind tunnel placed at Aerodynamics laboratory Mechanical engineering department MUET Jamshoro and numerical results were obtained through ANSYS Fluent 15.0. SA (Spalart Allmaras) model was chosen for computational analysis. The experimental and numerical results were compared. The percentage of error was maximum for Lift coefficient of NACA 4412 and for coefficient of Drag the maximum percentage of error was obtained in NACA2412.

ACKNOWLEDGEMENTS

We would like to thank Faculty of Mechanical Engineering department, MUET Jamshoro for allowing us to use the subsonic wind tunnel for experimental work and we would also like to thank Faculty of Department of Mechanical Engineering

NED UET Karachi for their computational facilities.

REFERENCES

[1] S. S. Bhat and R. N. Govardhan, "Stall flutter of NACA 0012 airfoil at low Reynolds numbers," Journal of Fluids and Structures, vol. 41, pp. 166-174, May 2013.

[2] N. Benard, J. Jolibois, and E. Moreau, "Lift and drag performances of an axisymmetric airfoil controlled by plasma actuator," Journal of Electrostatic, vol. 67, pp. 113-139, January 2009.

[3] J. Yao, W. Yuan, J. Wang, J. Xie, H. Zhou, M. Peng, and Y. Sun, "Numerical simulation of aerodynamics performance for two-dimensional wind turbine airfoils," Procedia Engineering, vol. 31, pp. 80-86, 2011.

[4] L. B. Li, Y. W. Ma, and L. Liu, "Numerical simulation on aerodynamics performance of wind turbine airfoil," in Proc. World Automation Congress (WAC), 2012, pp. 1-4.

[5] F. Villalpanda, M. Reggio, and A. Ilinca, "Assessment of turbulence model for flow simulation around a wind turbine airfoil," Modelling and Simulation in Engineering, February 2011.

[6] Şahin, İzzet, and Adem Acir. "Numerical and experimental investigations of lift and drag performances of NACA 0015 wind turbine airfoil." International Journal of Materials, Mechanics and Manufacturing 3, no. 1 (2015): 22-25.

Stress Analysis of Gas Turbine High Pressure Compressor Stage 4 Blade At Different Loading Conditions

Junaid Ahmed Khalid
Department of Mechanical Engineering
NED University of Engineering and Technology
Karachi, Pakistan
Junaidahmedkhalid@gmail.com
Contact No: 03363396002

Dr. Murtaza
Department of Mechanical Engineering
NED University of Engineering and Technology
Karachi, Pakistan
drmurtuza@neduet.edu.pk

Dr. Maaz Akhtar
Department of Mechanical Engineering
NED University of Engineering and Technology
Karachi, Pakistan
maazakhtar@hotmail.com

Abstract: In the current work the fourth stage of High pressure compressor blade of a nine stage high pressure compressor has been analyzed for static structural analysis using Solid Works Simulation. In this paper the effect of induced axial and vertical stresses on the compressor blade is being investigated. A structural analysis has been carried out to investigate the stresses and displacements of the turbine blade which is been develop due to the coupling effect of centrifugal loads. Different materials has been tested to suggest the best material for a compressor blade by comparing the results obtained for two different materials such as Titanium Ti 6Al 4Vand N-155 that has been considered for the analysis. The turbine blade along with dovetail joint is considered for the static structural analysis. The blade is modeled and analyzed on Solidworks .The geometric model of the blade profile is generated with curve points using an online tool called airfoil tool.

Key words: Static structural, Gas turbine blade, High Pressure Compressor, Twist Angle, Airfoil, Axial Load

I. INTRODUCTION

For many decades, researchers have steadily worked on improving the performance of gas turbine engines. Major Advances were made in the areas of materials, structures, controls, reliability, thermal cycles, thrust to weight ratio, and overall pressure ratios. Improving performance, reducing operating cost, lowering emission and noise, and enhancing structural reliability of gas turbine engines are economical to meet the challenges of the new century. Production of lighter engines than conventional engines with higher efficiency and improved reliability compared to present technology is essential.

Gas turbine engine blades are subjected to severe stresses which are caused by complex in-service environment [1-3]. The non-uniform aerodynamic excitation formed by rotor/stator interaction, inlet distortion and rotational stall is the primary factor which produces the high level vibration stress of rotor blades [4-6]. The high cycle fatigue failure caused by the forced vibration response is the main failure mode of the blade, affecting the life and reliability of gas turbine engine [7]. When rotating speed approaching the resonant speed of the campbell diagram, the resonance stress of the blade increases abruptly, the resonance stress quickly falls when the rotating speed passed through the resonant speed.

One of the most important and critical component of the gas turbine engine is turbine blades of different stages. The complete performance of the engine depends on the ability of turbine blade to extract energy from the hot gases. One of the major causes of failure in gas turbine engine is the breakdown of compressor blade. The failure of the compressor blade may lead to catastrophic consequences both physically and economically. An appropriate design of turbine blade with economical material selection is needed to avoid theses consequences.

II. PROBLEM STATEMENT

Due to high centrifugal forces and high temperature working conditions the gas turbine blades are experiencing high stresses. Due to the high stresses in turbine blade there may be chance of failure or change in the shape of turbine blade. To prevent the failure or change in the shape of

the turbine blade we should know the amount of stresses and deformation acting on the blade.

The temperature ranges at different stages of turbine blades are .i.e. Temperature in compressor blades is 450°C, temperature range in HPT blades is 1390°C and temperature range in LPT Blades is 600°C. However this study does not consider temperature condition. Moreover the effect of temperature can be included by using lower values of strength. Mostly temperature conditions had importance in HPT blades because of their high temperature environment. In this research work HPC blades are considered, HPC Blades mostly depends on axial loads and vertical loads of compressed air.

The main intention of this work is to know the amount of stresses acting on the fourth stage gas turbine compressor blade and to come up with an idea to minimize the stresses and increase the life of gas turbine blade. In the present work gas turbine blade has been analyzed for static structural analysis at different loading conditions by fixing Dovetail end of the blade.

III. METHOD AND PROCEDURES

A. Objective

The main objective of this paper is to understand the loads acting on the turbine compressor blade and obtain the geometric details from the literature review [1].The geometry of HPC gas turbine blade is obtained from online tool of airfoil. This geometry of gas turbine compressor blade is meshed and carryout Stress Analysis analysis by applying boundary conditions We assume the material to be linearly elastic and isotropic therefore the loads were selected in a way so as to keep the operating stress below yield strength of the material, whereas yield strength was considered to be in the limit of elastic region. This compressor blade is analyzed by using N-155 and Titanium alloy (Ti 6Al 4V) material. After successful analysis of blade at different loading conditions, this work will help designers to choose best material for blade design.

B. METHODOLOGY

The geometry was created using commercially available Solid works Software and geometry was meshed using Solid Works Simulation.

Boundary conditions were applied to the compressor blade by fixing Dovetail End of blade and apply Distributed load in vertical direction and axial direction.

The results obtained were validated with literature review results.

Design of the turbine blade was optimized and analyzed for two different materials with same boundary conditions. Compressor blade is analyzed for Structural Stress analysis at twist angle and without twist angle of blade. Results of these blades are compared with the yield of strength of the blade.

IV. GEOMETRY RESULTS

The gas turbine blade is modelled in Solidworks. The model of gas turbine blade with Dovetail joint is considered for the analysis. The complete gas turbine blade geometry details are discussed below.

The gas turbine blade is modelled using X and Y coordinate points. The file consisting of X and Y coordinate points in .sldcrv.

Key Point Number	Coordinate Y (mm)	Coordinate Y (mm)
1	10	0.01
2	9.5	0.15
3	9	0.27
4	8	0.49
5	7	0.67
6	6	0.81
7	5	0.92
8	4	0.98
9	3	0.98
10	2.5	0.94
11	2	0.88
12	1.5	0.79
13	1	0.66
14	0.75	0.58
15	0.5	0.47
16	0.25	0.34
17	0.13	0.24
18	0	0

19	0.13	-0.14
20	0.25	-0.19
21	0.5	-0.25
22	0.75	-0.27
23	1	-0.29
24	1.5	-0.29
25	2	-0.27
26	2.5	-0.25
27	3	-0.23
28	4	-0.18
29	5	-0.14
30	6	-0.1
31	7	-0.06
32	8	-0.04
33	9	-0.02
34	9.5	-0.02
35	10	-0.01

Table 1. Blade Coordinates

Gas turbine Engine stage 4 compressor blade with Dovetail joint with one end fixed is shown below.

Fig 1: HPC Stage 4 Blade with Dovetail Joint

The Fine Meshed view of compressor blade is also shown below.

Fig 2: HPC Stage 4 Blade Meshed form with Dovetail Joint

Mesh Statistics	
Nodes	112029
Elements	67728
Mesh Element Type	Tetrahedron
Mesh Type	Solid Mesh

Table 2. Meshing Details of Compressor Blade

Also in this paper the compressor blade is also tested with twist angle of -20 degrees to check the strength of blade as shown in figure below.

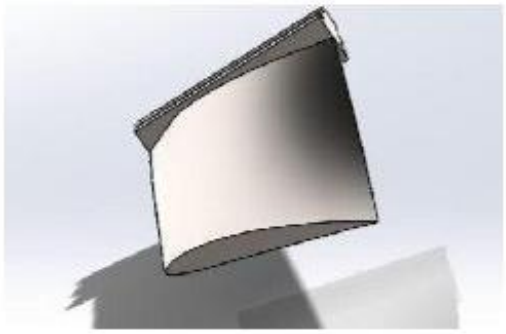

Fig 3: HPC Stage 4 Blade with Twisted Angle of -20 Degrees

Material Properties

Following are the material properties used in this paper.

Material Properties	Units	TI 6AL 4V	NI 155
Elastic Modulus	N/m^2	1.0480031e+0.11	2.1e+011
Poisson's Ratio	—	0.31	0.21
Shear Modulus	N/m^2	—	7.9e+0.11
Mass Density	Kg/m^3	4428.78	8500
Tensile Strength	N/m^2	1050000000	317000000
Yield Strength	N/m^2	827370880	59000000

Table 3. Material Properties

V. BOUNDARY CONDITIONS

To simulate the real time working conditions of forces acting on the gas turbine blade, boundary conditions are given. We assume the material to be linearly elastic and isotropic therefore the loads were selected in a way so as to keep the operating stress below yield strength of the material, whereas yield strength was considered to be in the limit of elastic region.

Following Conditions have been applied in this experiment in which for both materials in which yield strength was in elastic region.

Axial and vertical distributed Forces of 200N are applied for normal blade without twist and the same Force of 200 N is applied for twist Blade to check the maximum yield strength of both compressor blades.

VI. RESULTS AND DISCUSSION

This Section of work deals with the results of static stress analysis of HPC Stage 4 Blade at different loading conditions by using TI Al 4V and Nickel N155 material properties.

Results of experiments were obtained using solid works simulation technique. Results of both blades twist and without twist by applying distributed with fixing on end shown below.

A. Stress Analysis Results

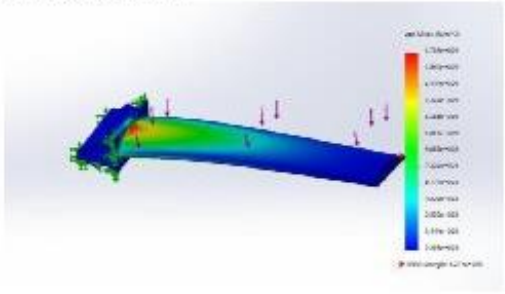

Figure 4. Von Mises stress of Titanium Ti 6Al 4V alloy

In Figure 4 200N vertical distributed load is applied on without twist blade and results shown that the von Mises stress of material is less than tensile yield strength of material that is 1.733e+009 <8.27e+008 , it means compressor blade will not rupture.

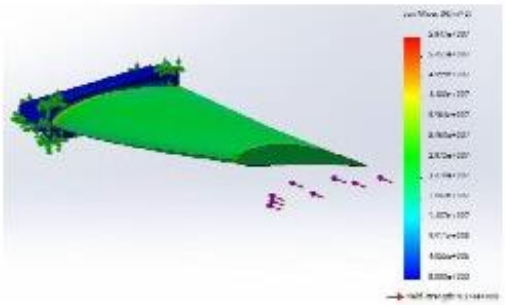

Figure 5: Von Mises stress of Titanium Ti 6Al 4V alloy

In Figure 5 200N Axially distributed load is applied and results shown that the von Mises stress of material is less than tensile yield strength of material that is 5.947e+009 <8.27e+008 , it means compressor blade will not rupture.

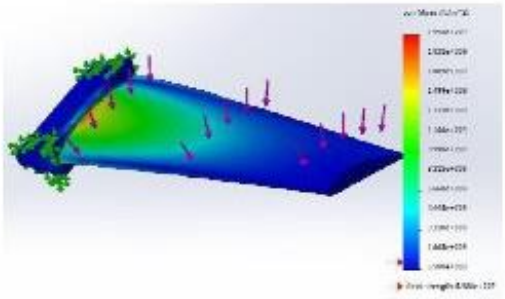

Figure 6. Von Mises stress of Nickel N155 alloy

In Figure 6 200N vertical distributed load is applied on twisted blade and results shown that the von Mises stress of material is less than tensile yield strength of material that is 1.998e+009<5.900e+008,it means compressor blade will not rupture.

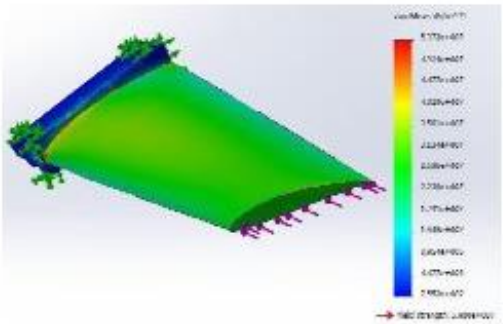

Figure 7. Von Mises stress of Nickel N155 alloy

In Figure 7 200N Axial distributed load is applied on a twisted compressor blade and results shown that the von Mises stress of material is less than tensile yield strength of material that is 5.37e+007 <5.90e+007, it means compressor blade will not rupture

VII. SUMMARY

In the current work two materials i.e Titanium 6AL-4V alloy and N 155 have been taken for analysis.

Various conclusions derived from the work are as follows:

The Von Mises stress of Titanium 6AL-4V which way less than the tensile yield strength. By observing all the results of these experiments, it is concluded that the best material for gas turbine compressor blade is Titanium Alloy because it has more strength and less weight. While when cost is the primary issue then NI 155 is preferred.

Whereas Strength of without twist blade is more than with twist, however with twisting the blade we get more thrust of engine, for this purpose the twisted blade is coated with ceramic coating.

Detailed study of different materials and alloys that can be used in gas turbine blade should be done.

Different coatings may be used to increase the strength of blade.

REFERENCES

[1] L.Umamaheswararao, Dr. K. Mallikarjunarao. "Design and analysis of a gas turbine blade by using FEM", ISSN: 2278-621X, Vol. 4 Issue 4 November 2014 published by International Journal of Latest Trends in Engineering and Technology (IJLTET).

[2] Structural dynamic analysis of turbine blade by 2017 First International Conference on Recent Advances in Aerospace Engineering (ICRAAE) by Daniel Anthony.

[3] P.V.Krishnakanth, G.Narasa Raju, R D V. Prasad, R. Saisrinu. "Structural & Thermal Analysis of Gas Turbine Blade by Using F.E.M", ISSN 2278 – 0882, Volume 2 Issue2 pp 060-065 May 2013 published by International Journal of Scientific Research Engineering & Technology (IJSRET)..

[4] "Blade Health Monitoring of Gas Turbine using Online Crack Detection" by Bai Liu, Longli Tang, Tong Liu, Zijian Liu China Institute of Marine Technology & Economy

[5] S. Moffatt and L. He, "Blade Forced Response Prediction for Industrial Gas Turbines. Part 1: Methodologies," Proceedings of ASME Turbo Expo, 2003..

[6] Barhm Abdullah Mohamad and Abdelsalam Abdelbussien. "Failure analysis of gas turbine Blade using finite element Analysis", Article ID: IJMET_07_03_027, Volume 7, Issue 3, May–June 2016, pp.299–305. International Journal of Mechanical Engineering and Technology (IJMET).

[7] Https:// www.airfoiltool.com

EFFECT OF SPECIFIC CHARGE IN THE PRIMARY ATOMIZATION ZONE OF ELECTROSTATICALLY CHARGE BIODIESEL SPRAYS

Shehzaib Yousuf Khan
School of Aerospace, Mechanical and Mechatronic Engineering, The University of Sydney, NSW, Australia

*Corresponding author. Tel.: +92 322 2784372
E-mail address: skha7071@uni.sydney.edu.au (Shehzaib Y. Khan)

ABSTRACT

Electrostatically charge injection atomization of Fatty Acid Methyl Ether (FAME) called Biodiesel is shown to work varying electrode gap to diameter ratio and injection velocities. An experimental setup has been built for observing the break-up mechanism of Biodiesel sprays against Diesel as studied by other researchers earlier. The spray characteristics of the macroscopic structure of primary atomization zone are investigated at different conditions using image processing. The structure includes the location of onset of spray dispersion which is measured and compared with the break-up length. The electric charge induces an electrostatic repulsion between the surface and tip of the liquid jet which is proportional to the break-up parameters. The electric potential is provided with negative polarity to the electrode which affects the position of the onset of dispersion. In this paper, the graph of experimental data is compared with the semi-empirical formula for break-up length developed by Shrimpton and Yule [1] and the effect of electric charge is analysed for different Biodiesel blends with Diesel.

Keywords: Primary atomization; Electrostatic atomization; EHD; jet breakup; sprays

1 INTRODUCTION

The Electrostatic atomization of liquid fuels has always been a significant topic for combustion for past four decades where Kim & Turnbull used a chemically etched tip needle in a glass capillary with very low flow rates and current [2]. The Electrohydrodynamic (EHD) atomization is not commercially available due to limited knowledge. However, this technology was predominantly matured time to time with the research of J. Shrimpton, A. Yule, A. Rigit, G. Malkawi and A. Kourmatzis [3]. EHD atomizer works similar to fuel injection atomizer in internal combustion engines however the EHD atomizer consumes much lower electrical power as low as 2 milli-Watt. These atomizers are promised to provide quality sprays to small engines 20 – 250 cc, microscale turbines, painting and many other spraying applications.

The main objective of this paper is to understand the characteristics of the EHD Atomization in the primary region where the jet breakup is observed. The spray characteristics is defined by the quality of atomization which include finer droplet, larger cone angle of sprays and shorter jet breakup length. The quality of spray is always desired with parameters such as jet breakup length, breakup angle and droplet size. The breakup length is the distance from the nozzle orifice to the breakup of the liquid jet.

The atomization can be induced by the electric repulsive force which is proportional to the electric charge, also the electro-convective turbulence is promoted potentially which is as efficient as compared to pressure atomization. The dielectric nature of Diesel and Biodiesel carries the electric charge causing dispersion and breakup of injected fluid into fine spray and droplets due to disruptive electric field. Shrimpton and Yule suggested that the jet breakup length is a function of specific charge ($\mathbb{Q}_m$) which can be calculated using the semi-empirical equation [1]:

$$l_j = u_{inj}\tau_j \qquad \tau_j = \frac{\varepsilon_o \varepsilon_r}{\kappa \mathbb{Q}_m} \qquad (1)$$

u_{inj} is the average jet velocity, t_j is the characteristic time, κ is the liquid ionic mobility, ε_o is the permittivity of vacuum which is a constant equal to

8.8542 × 10-12 F/m, and ε_r is the relative permittivity also called dielectric constant which depend on the liquid type. For Diesel and Biodiesel, the relative permittivity is approximated to 2.2. The ionic mobility is also dependent on the liquid type and inversely proportional to liquid dynamic viscosity which can be related via Walden's rule [8]

$$\kappa = C\mu^{-1} \quad (2)$$

The EHD atomizer schematically shown in Fig. 1, is a 'third generation' atomizer subsequent to the previous research and development of charge injection system by many groups. The two electrodes in the atomizer are separated by a distance called 'inter-electrode gap' where the electric potential up to -15kV is provided by a high voltage power supply. The charged and grounded electrodes are fully immersed in the dielectric fluid and the fluid is injected through an orifice created by drilling into the grounded base.

2 EXPERIMENTAL SETUP

The test rig as shown in Fig. 2 contains an electrostatic charge injector, current measurement system and an imaging system in which the electrostatic injector is facilitated with a high voltage power supply and a fuel pump. The electrostatic injector also includes a micrometre to control the electrode gap. In current measurement, the spray current is measured using a digital pico-ammeter and the leakage current is measured using an analogue micro-ammeter. The macroscopic structure of the jet breakup into spray is captured using a CMOS camera using five different fuels including Diesel and Biodiesels.

2.1 Fuel Selection

Four different blends of Biodiesels named as B1, B2, B3 and B4 are used as working fluid in the EHD atomizer along with Commercial Diesel at The University of Sydney [5]. These Biodiesel blends B1, B2, B3 and B4 are Fatty Acid Methyl Esters (FAMEs) manufactured from methanolysis trans-esterification of Palmere, Coconut, Pale and Canola based Oils respectively. The carbon chain lengths and saturation level are different where B1 has the shortest chain and B4 has the longest among these blends. B1 and B2 are saturated, B3 is partially saturated while B4 is almost fully unsaturated. The fluid properties are affected by the varying change lengths and resulting lower ionic mobility as the viscosity of the blend increases. The properties of these biodiesels and diesel such as density, viscosity and surface tension are shown in Table 1.

2.2 Atomizer Design

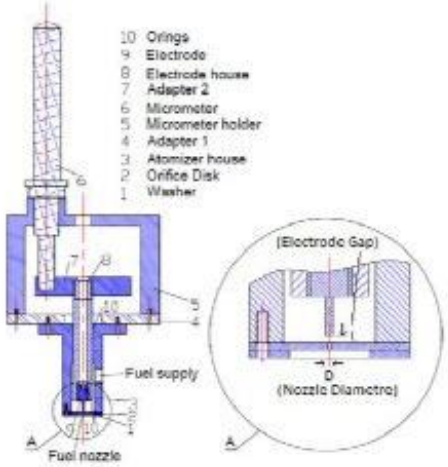

Figure 1. Schematics of EHD atomizer plane-plane electrode layout

The schematics of Electrohydrodynamic (EHD) or electrostatic charge injection atomizer is used as shown in Fig. 1 which has been developed at The University of Sydney similar to a typical plane-plane charge injector [4]. The atomizer design includes atomizer housing, electrode housing, electrode, orifice disk and micrometre. The housing is made from Perspex in which the inside of the

Table 1. Fuel properties and operating conditions used in the experiments

Fuel	u_{inj} (m/s)	Q_v (C/m^3)	ρ (kg/m^3)	μ (Pa.s)	σ (N/m)
B1 $(C_{9.5}H_{19.7}O_2)$	2.5-10	0.16 – 0.53	877	0.00171	0.0261
B2 $(C_{14.8}H_{28.5}O_2)$	2.5-10	0.48 – 0.83	871	0.00381	0.0284
B3 $(C_{18.3}H_{35.5}O_2)$	2.5-10	0.35 – 1.16	873	0.00432	0.0299
B4 $(C_{18.7}H_{35.5}O_2)$	2.5-10	0.35 – 1.30	879	0.00465	0.02996
Diesel (C_xH_y)	2.5-10	0.38 – 0.79	848	0.0032	0.0230

atomizer can be observed. The nozzle orifice base disk is grounded and contains nozzle opening of diameter (D) 250 µm. The inter-electrode gap (L) is controlled using Starrett Micrometre Head which has non-rotating spindle ranging from 0 to 1 inch with 0.001-inch graduation. The Micrometre is set for inter-electrode gap to diameter ratio (L/D) equal to 1.5 and 2.

2.3 Measurement Method

The electric potential is controlled using a high voltage power supply, Spellman SL Series, ranging from 1 kV to 130 kV and 10 W power where the electrode is provided negative polarity from 0 to -14.5 kV. A Genie Touch Syringe Pump System is used to control flow rate (Q_L) of the fuels from which jet injection velocities are calculated equal to 2.5, 5, 7.8 and 10 m/s. The syringe pumps include two cylinders at a time of 60 mL capacity each.

The spray current (I_s) is measured using a Keithley Model 6485 Pico Ammeter ranging from 10 fA to 20 mA and an average is estimated to record the values for each voltage. The spray current flows the charged spray which is collected from a metal container isolated from the test setup. The leakage current (I_L) is the current leaking from the ground electrode connected with orifice disk. The leakage current is measured from Simpson Taut-band 0-10 DC Micro Ammeter ranging 0 to 10 µA with 0.2 µA least count.

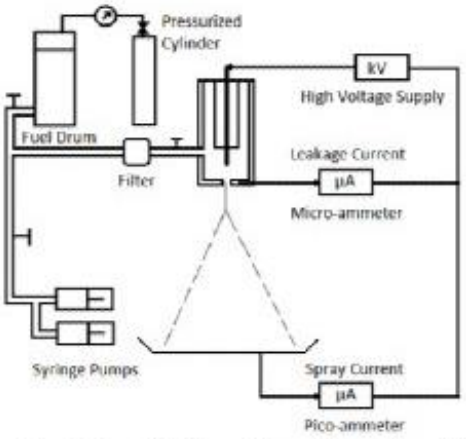

Fig. 2. Circuit Schematics of Experimental Setup.

2.4 Image Processing

A CMOS camera Canon 600D and Canon EF-S 50mm lens are used to capture the macroscopic structure in the primary atomization zone are shown in Fig. 3. A Matlab code has been developed to binarize the images taken by the camera and quantify the locations where the spray starts to disperse known as 'location of onset of dispersion (χ)'. This technique has been employed to measure the breakup length (l_j) in most of the literature on EHD sprays [1]. The location of onset of dispersion is taken as experimental breakup length in this paper and compared for five working fluids with different injection velocities and electrode gap to diameter ratios.

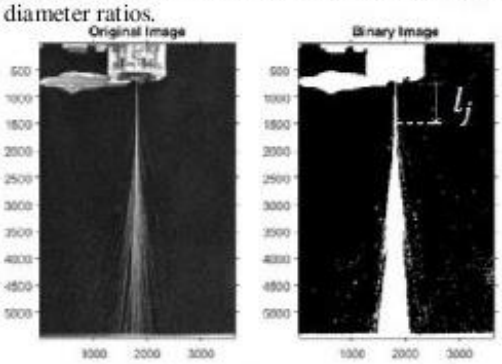

Fig. 3. Example of a binary image of jet breakup and dispersion taken with CMOS Camera setup and processed in MATLAB.

3 RESULTS AND DISCUSSION

3.1 Location of Onset of spray dispersion

The location of onset of dispersion is measured using image processing in MATLAB by varying electric potential from 0 to -14.5 kV at Nozzle Diameter D = 250 µm and inter-electrode gap to diameter ratio L/D = 1.5 and 2, controlled by the micro meter attached to the atomizer. Also, four different injection velocities u_{inj} = 2.5, 5, 7.8 and 10 m/s are used in this experiment for biodiesel B1, B2, B3, B4 and commercial diesel. Different graphs are plotted for different fuels against the applied voltage to observe the profile of the onset of dispersion. The onset of dispersion is scaled by taking ratio χ/D which shows a declining steep curve at higher voltage. The onset of dispersion can be compared with the jet breakup length which is the function of specific charge.

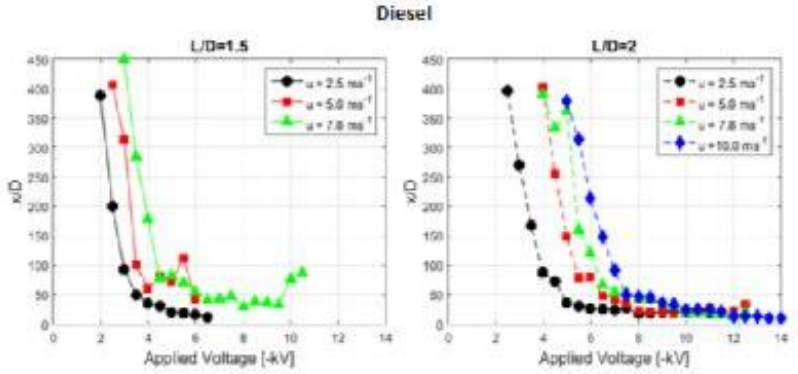

Fig. 4. x/D versus voltage for Diesel at D=250µm, L/D=1.5 and 2 with different injection velocities u_{inj}=2.5, 5, 7.8 and 10 m/s

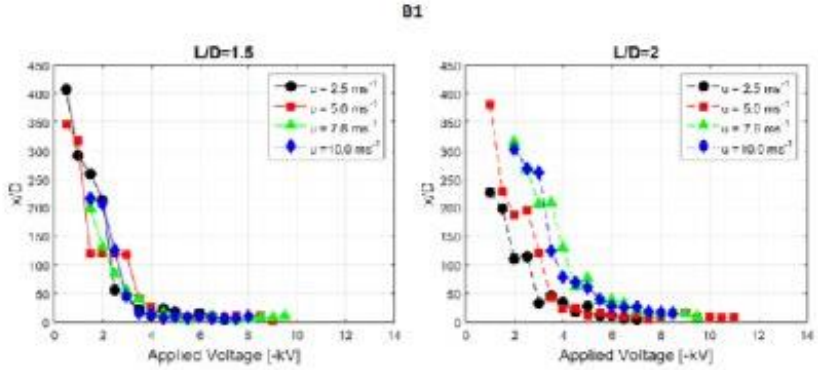

Fig. 5. x/D versus voltage for B1 at D=250µm, L/D=1.5 and 2 with different injection velocities u_{inj}=2.5, 5, 7.8 and 10 m/s

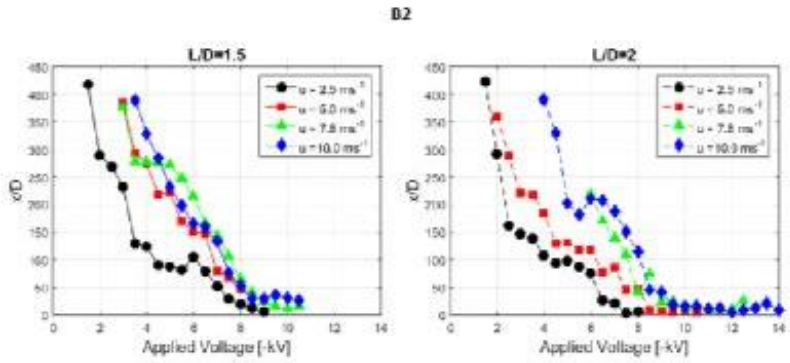

Fig. 6. x/D versus voltage for B2 at D=250µm, L/D=1.5 and 2 with different injection velocities u_{inj}=2.5, 5, 7.8 and 10 m/s

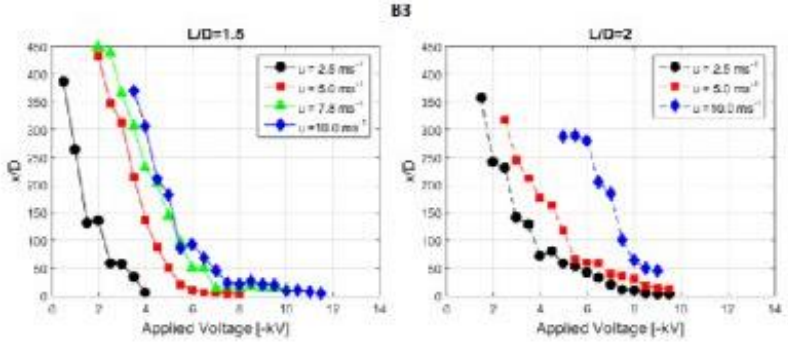

Fig. 7. x/D versus voltage for B3 at D=250µm, L/D=1.5 and 2 with different injection velocities u_{inj}=2.5, 5, 7.8 and 10 m/s

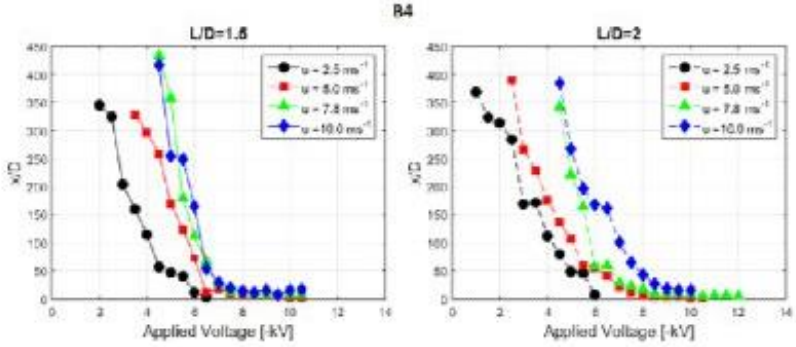

Fig. 8. x/D versus voltage for B4 at D=250µm, L/D=1.5 and 2 with different injection velocities u_{inj}=2.5, 5, 7.8 and 10 m/s

Specific charge (C/m^3) is measured from spray current divided by volumetric flow rate which has a parabolic profile for supercritical regime. The specific charge drops after a maximum value and at this point the critical voltage (V_c) is found out as mentioned in previous studies [1]. The breakup length is limited to macroscopic structure and microscopic imaging technique is required to measure smaller lengths at voltages greater than critical voltage.

The x/D plots versus applied voltage increases as the injection velocities increases which is an agreement to Shrimpton and Yule [1]. The profile is almost similar to different L/D value where specific charge is depending on viscosity. The specific charge is greater for higher viscosities such as in B3 and B4. The maximum specific charge is plotted against Reynolds number ($Re = \rho u_{inj} D/\mu$) of different fuels at different velocities as shown in Fig. 9.

3.2 Theoretical Breakup length Correlation

The numerical values of breakup length are calculated by substituting the properties of different fuels in equation 1. The constant C in ionic mobility is determined from the experimental breakup length data which is approximated which is near to Castellanos approximation 3×10^{-11} [6,7]. The central values of constant C are found to be 3×10^{-11} for Diesel, 2.05×10^{-10} for B1, 1.19×10^{-10} for B2, 4.74×10^{-11} for B3 and 3.59×10^{-11} for B4. The ionic mobility is greater in lower viscous fuels which promote electro-convective turbulence prior to the higher viscous fuels.

A range of Maximum specific charge is determined for each fuel at L/D=1.5, 2 and different velocities as shown in Table 1. The plot shown in Fig. 9 is evident that the maximum specific charge is varied with the hydrodynamics of the fluid. The Reynolds number is estimated for comparing the peak

specific charge that supports the semi-empirical equation further. This result in longer break-up length when the electric charge is stretched out for higher hydrodynamic forces. The maximum specific charge is substituted along with the ionic mobilities of different fluids to calculate the theoretical value of the break-up length.

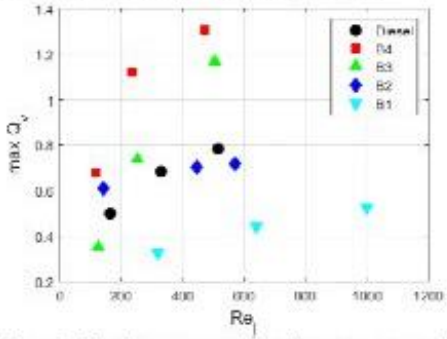

Fig. 9. Maximum specific charge versus jet Reynolds number at L/D=1.5

The experimental breakup length l_{exp} is taken as the location of the onset of spray dispersion x and compared with the theoretical values l_{calc} formulated from the equation (1). The profile is shows linear profile for Diesel, B1 and B3, however for higher viscous fluids the values do not match. This is due to the limitation of the macroscopic structure where experimental values should be determined carefully. Also, below the threshold voltage V_{th} where the dispersion and breakup begin the measured values do not coincide with the theoretical values. The threshold voltage is where the charge initiates spray dispersion which will be further analysed in the future using leakage current.

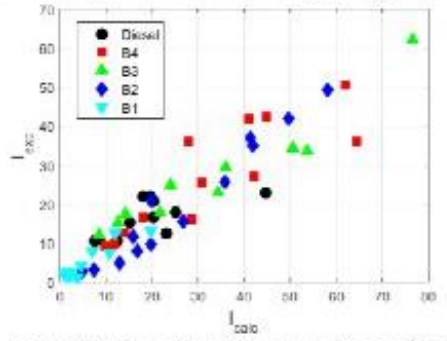

Fig. 10. Experimental versus theoretical breakup length for Diesel and Biodiesel blends B1, B2, B3 and B4 at D=250µm and L/D = 1.5 and different operating conditions.

4 CONCLUSIONS

The Diesel and Biodiesel sprays in Electrostatically charged injection system have been investigated and the results from this study prove that the electric charge is significant in measuring the break-up length. The injection velocity is also significant and for higher values the break-up length increases. The location of onset of dispersion spray is relative to the break-up length which varies with applied voltage for all biodiesel blends similar to commercial diesel. Future work will include analysis of extended electrical performance and non-dimensional numbers such as Weber number and Ohnesorge number. Also, the microscopic structure can be observed to provide better correlation for break-up length for different biodiesel blends.

ACKNOWLEDGEMENTS

I would like to thank The University of Sydney and my supervisors for giving me the opportunity to research in the field of Electrohydrodynamics.

REFERENCES

[1] Shrimpton, J.S, Charge Injection System, Springer 2009

[2] Kim, K., Turnbull, J.: Generation of charged drops of insulating liquids by electrostatic spraying. Journal of Applied Physics 47(5), 1964 (1976)

[3] A. Kourmatzis and J.S. Shrimpton,, Atomization and Sprays, 22(4) (2012) 351-370

[4] Pham, Kourmatzis, Khan, Masri. (2017). Dual-Angle Micro-Particle Tracking Velocimetry in the Primary Atomization Zone of Electrostatically Charged Diesel Sprays

[5] P.X. Pham (2015) Influences of Molecular Profiles of Biodiesels on Atomization, Combustion and Emission Characteristics. PhD Thesis, The University of Sydney, Sydney, Australia

[6] Castellanos A, Basic concepts and equations in electrohydrodynamics. In: Castellanos A (ed) Electrohydrodynamics, 1st edn. Springer, New York, pp 1– 62, 1998

[7] A. Castellanos. Introduction to Electrodynamics (3rd edition). Prentice Hall, 1999.

[8] Chang, J. S., Crowley, J. M., and Kelly, A. J., "Handbook of Electrostatic Processes. Dekkar," 1995.

EXPERIMENTAL ANALYSIS OF DIESEL AND DUAL-FUEL ENGINE

Tanweer Hussain[1], Ateeque Ahmed[2], Bilal Ahmed*[2], Dur Muhammad[3], Abdul Fatah[3], Muhammad Waseem[4]

[1]Mechanical Engineering Department, Quaid-e-Awam University of Engineering and Technology Nawabshah, Pakistan

[2]Department of Mechanical Engineering, NED University of Engineering and Technology Karachi, Pakistan

[3]Mechanical Engineering Department, Mehran University of Engineering and Technology Jamshoro, Pakistan

[4]School of Engineering, Computer & Mathematical Sciences, AUT University, Auckland, New Zealand

*Corresponding author. Tel.: +92-332-3964756

E-mail address: 12me76@student.muet.edu.pk

ABSTRACT

The current issue of global warming and concerns about environmental pollution researchers are focusing more on alternative fuels that is cost efficient and produce less emissions than fossil fuel. Diesel engines produce more emissions due to their heavy duty operations and diesel fuel is costly too, so different studies related to emissions and development of alternative fuel have been done by many researchers. Diesel fuel when mixed with natural gas in diesel engine is called dual-fuel engine, it produces less emissions and it costs less than diesel fuel. This research is based on an experimental setup in which the comparative analysis has been done for the engine in terms of emission and performance. The objective of this project is to study the performance and exhaust gases of dual-fuel single cylinder compression ignition engine. Natural gas is used with diesel for dual- fuel. Moreover, from the diesel engine, a high compression ratio can be obtained. The losses in power are also less, therefore, it reduces the cost of conversion kits and fuel. The output of the engine is being achieved based on brake power and torque in order to investigate the thermal efficiency under various running conditions. After experimental results, it is concluded that the dual-fuel engine has increased the thermal efficiency and reduced the emissions i.e. CO and NO_x, etc. which are toxic for the environment.

Keywords: Natural Gas, Diesel Engine, Dual-Fuel, Thermal Efficiency, Emission

1 INTRODUCTION

The rising issue of global warming and its impacts on our environment is now a great concern for scientists and researchers. When fossil fuels burns its releases different gases that are harmful to environment such as CO_2. The emissions that are released by vehicles also contribute to environmental pollution. The most common type of engines are petrol and diesel engines, the diesel engines release more toxic gases than petrol due to its heavy duty operations.

Whereas natural gas releases less greenhouse gases due to fact that it contains less contents of carbon but it has less power as compared to diesel engine this issue can be solved by using a dual fuel engine that has less emissions and have higher power than CNG engines. The usage of diesel fuel has grown due to increase in number of diesel engine operated vehicles and diesel fuel engine emissions plays an important role in environmental pollution and global warming [1]. The development of dual fuel commercially goes back to late 1930's when a dual fuel engine that was filled with town gas was produced and operated in England [2]. During Second World War the interest the shortage of conventional liquid fuel supplies the application of dual fuel engines rose in several countries. Many conversions of diesel fuel engines were suggested for military and civil applications and that includes diesel fuel used with natural gas, mal gas and blast furnace gas. The chief components of these gases were hydrogen, carbon monoxide, methane, ethane, propane and other hydrocarbons often in presence of diluent gases such as nitrogen, carbon dioxide and water vapor [3]. Natural gas is widely used as an alternative for transportation purpose and for dual fuel engines due to its low cost and environmental advantages over other gasoline and

diesel fuel [4, 5, 6, 7]. It is forecasted that with the depletion of good quality petroleum crudes, diesel fuel quality (CN and distillation properties) will deteriorate continuously in the future, which will greatly affect the performance of diesel engines and will conflict with environmental goals to lower pollution emissions [8, 9, 10]. Effective measures have been taken to improve the dual fuel operation of ignition engines [11, 12, 13]. This project aims at replacing the diesel fuel with dual fuel because emissions are less. The dual fuel means that engine utilizes the pilot diesel fuel to ignite CNG. Engine performance and emissions are calculated at different speeds. In this study engine performance parameters are calculated first at fixed speed of 1800 RPM for both diesel and dual-fuel engine and then results are calculated at different speeds. The exhaust data is also compared at maximum and moderate operating load conditions for both types of engine.

2 LITERATURE REVIEW

The effects of changes in the initial charge temperature, oxygen and diluent concentrations, pilot liquid fuel quantity and injection characteristics on the length of the ignition delay period of the pilot, when a range of different gaseous fuels were admitted with the intake air, were investigated by Karim and his co-workers [14, 15, 16]. The findings of Lewis [17], Felt et al.[18] and Karim [19] confirmed that with very lean gaseous fuel-air ratios, the flames initiated from the multitude of the ignition centres of the liquid diesel pilot spray will fail to propagate throughout the whole combustion chamber, leaving various amounts of the gaseous fuel-air charge unconverted. Studies by Clark and Bunch [20], Karim and Rogers [21] and Karim and Klat [22] established that the ignition and combustion processes depended not only on the injection and ignition characteristics of the diesel pilot, but also depended strongly on the type and concentration of the gaseous fuel employed. Tesarek [23] who fumigated natural gas in a single cylinder, direct injection diesel engine and replaced up to 80% (on an energy basis) of the liquid fuel by gas, mainly to reduce particulate emissions, observed very large associated increases in un burnt hydrocarbons (HC) and CO emissions. In a survey of the dual fuel engine performance at light load, Karim [19] concluded that any of the measures which increase the size of the combustion zone in the vicinity of the pilot or enhance the effective flammability limits of the charge at around the pilot fuel, could reduce significantly the unburnt gaseous fuel in the exhaust gas.

Liu [24] developed a multi-zone analytical model to predict the features of combustion processes in a dual fuel engine. His results were consistent with the findings of the previous experimental work and showed that for lean mixtures most of the CO is produced from the partial oxidation of the gaseous fuel [25]. This was due to the low charge temperature and relatively slow reaction rates of the gaseous fuel in the reacting zone. For higher gaseous fuel concentrations in the mixture, no partial oxidation was evident in dual fuel engine operation and most of the CO was produced primarily from the pre-ignition reactions of the gaseous fuel within the unburnt zone. Most of the above mentioned investigations were performed on single cylinder, direct injection, normally aspirated research engines that provide better flexibility of control and economy of testing. Some examples of studies performed on larger industrial engines types are also available such as those of Ding and Hill [26] and Barbour et al. [27].

Ding and Hill [26] used a four cylinder, turbocharged, prechamber, 7 litre diesel engine fuelled with natural gas to explore the combustion phenomena over a wide range of engine speed and load. It was found that the gas-air equivalence ratio is the key variable affecting both emissions and fuel economy. They reported very high unburnt hydrocarbons and CO concentrations at very light loads when using relatively small pilot diesel fuel input. They suggested that, especially at light loads, emission improvements may be realized by means of throttling (except NO_x, emissions) and by advancing the injection timing. Barbour et al. [27] examined the performance and emission characteristics of a six cylinder, prechamber, 4.3 litre diesel engine fuelled with natural gas and propane. At full load, no important change in either engine performance or exhaust emissions was found with the introduction of gaseous fumigants. As load was decreased gaseous fuel emissions (except NO_x) increased considerably. The percent of the unburnt gas was found to be independent of the amount of the particular gaseous fuel used. It was suggested that the main factor of influence concerning the unburnt fuel is the overall combustion temperature. However, it can be suggested that this can be viewed as the dominance of the pilot fuel combustion on the overall engine behaviour and emissions.

3 ENGINE PERFORMANCE PARAMETERS

3.1 ENGINE TORQUE

An engine's torque is a measure of its rotational force exerted to transmit power from the engine to the wheels of the vehicle through the drive train. The torque and power produced by an engine can be measured using a dynamometer which is mounted to the engine as a separate component. The product of torque and angular speed gives the power developed by the engine:

$$\tau = \frac{60P}{2\pi N} \quad (1)$$

Where,
T= Torque (N-m)
P= Power (W)
N= Engine Speed (RPM)

3.2 INPUT POWER

The input power of the engine refers to the maximum rate at which energy is supplied to the engine. The heat of combustion of fuel is supplied to the engine and assuming the cycle efficiency as unity where all the chemical energy of the fuel is converted into useful work the input power is given by:

$$IP = m_f Q_{hv} 10^3 \quad (2)$$

3.3 BRAKE POWER

The brake power is the power output delivered by the engine shaft. It is less than the indicated power since heat is lost to overcome the total friction generated in the engine which is summed as friction power.

$$BP = \frac{2\pi N\tau}{60 \times 10^3} \quad (3)$$

3.4 SPECIFIC FUEL CONSUMPTION

Specific fuel consumption is the measure of fuel flow rate per unit power output and relates to the fuel efficiency of an engine. Specific fuel consumption is defined as

$$sfc = \frac{\dot{m}_f}{P} \times 3.6 \times 10^6 \quad (4)$$

Where,
sfc= specific fuel consumption (g/kW.hr)
$\dot{m}_f$= mass flow rate of fuel (kg/s)
P= power output (kW)
In the performance measurement and comparison between engines running on diesel and dual-fuel for the experimentation the power output measured is the brake power Therefore, brake specific fuel consumption is

$$bsfc = \frac{\dot{m}_f}{BP} \times 3.6 \times 10^6 \quad (5)$$

3.5 BRAKE MEAN EFFECTIVE PRESSURE

The brake mean effective pressure is a useful measure of the relative performance of an engine. It refers to the mean pressure to be maintained in the pistons of the cylinder to produce a power output during each power stroke. The brake mean effective pressure can be calculated from the torque and is defined as

$$bmep = \frac{BP \times nR \times 60}{A \times L \times N \times n} \quad (6)$$

Where,
bmep= Brake mean effective pressure (kPa)
BP= Brake power (kW)
nR= number of crank revolutions for each power stroke per cylinder.
A= area of engine bore (m^2)
L= Length of engine stroke (m)
N= Engine speed (rpm)
n= number of cylinders

3.6 ENGINE THERMAL EFFICIENCY

Generally, an IC engine loses almost 42% of its energy to the exhaust system and a further 28% to the cooling system. The engine thermal efficiency refers to the ratio of work produced per cycle to the amount of fuel input to the engine per cycle

$$\eta_f = \frac{P}{\dot{m}_f Q_{hv}} \quad (7)$$

Where,
η_f = engine thermal efficiency
P= power output produced per cycle (kW)
$\dot{m}_f$= mass flow rate of fuel per cycle (kg/s)

4 EXPERIMENTAL SETUP

The experimental setup involves fixing of diesel engine, gas kit fitting, fuel consumption measurement system, fabrication of manifold and load measuring mechanism. The pressure of gas is regulated by gas pressure regulator. The pressure of gas is 20 MPa that will be reduced by gas pressure regulator. Emissions levels are measured by gas emission analyser. A portable 5 gas emission Analyser with pc software unit is used for this experiment to measure levels of HC, CO, O_2, CO_2 and NO_x.

4.1 FIXING OF DIESEL ENGINE

The single cylinder engine has a weight of 56 kg so it must be fixed well enough to with stand all load applied and the test bed must bear the running load and vibration created due to running of the engine. The engine must be placed on some strong material products to with stand all the loads, and should be placed at a suitable height so that it should be easy for the operator to start the engine with lever hand. The engine is fixed with nuts and bolts on the u shape guarders. The guarders are welded like "a" shape the firstly two guarders A & B are strongly welded to the square pipes of the frame and the guarders of C & D are welded on top of guarders A & B. To absorb the vibrations of the engine, the vibration absorbing foundation are made of rubber and are designed to minimize the vibration of up to 8 HP engines, these are made of elastic material having the nuts equally and exactly on the opposite sides of the base.

4.2 GAS KIT FITTING

The gas kit is a device which is used for the correct amount of flow of gas and gets correct fuel and mixture. The gas kit senses how much amount of gas is required for the correct mixture and it allows the outlet valve to open at some desired level and let the correct amount of gas to pass through it. The gas coming from the outside enters through inlet valve, the amount of inlet and outlet varies according to the need of engine, the amount of gas flow from the gas kit varies with the increase and decrease in load & speed.

4.3 FUEL FLOW MEASUREMENT

Fuel flow measurement of the fuel that engine uses certain amount of time on certain load. The fuel tank of engine is separated carefully and is assembled on vertical board. A pipe is attached vertically on the vertical board. This divisions are made to indicate 100ml, 200ml respectively on increasing upwards

4.5 FABRICATION OF MANIFOLD

The manifold has been fabricated in the fabrication shop of QUEST, Nawabshah. The installation of manifold is used to allow the mixture of air and gas, then it should be mounted vertically in such a way that gas uniformly available and mix instantaneously with the air stream.

Fig. 2: Manifold

4.4 LOAD MEASURING MECHANISM

Load measuring is one of the most important factors from our subjective point of view, because every mechanical activity involves load. The system involves converting of diesel engine into CNG system keeping in view the increasing cost of petroleum products and safety environment. For this purpose we have bought 6 hp 353 cm3 single cylinder engine having the dial of the fly wheel 33.66 cm and thickness of the fly wheel is 4.5cm and we have fabricated the bed in which the load measuring meter, fuel tank and gas flow meter are attached to it.

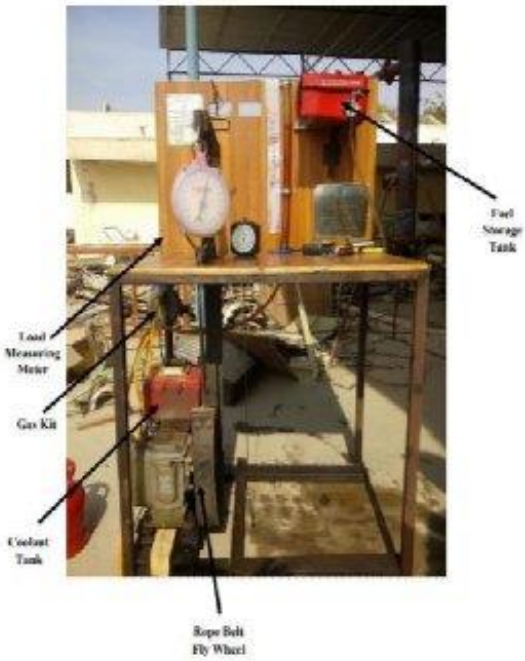

Fig. 1: Load measuring mechanism

5 LOAD AND EMISSIONS MEASURING PROCEDURE

The engine is started at diesel fuel first and for first five minutes no load is applied to engine in order to reach steady state operating condition. the engine is adjusted at speed of 1800 rpm and volume flow rate is calculated when engine use 50 ml of fuel then gas analyser probe is inserted in exhaust duct of engine and emissions are calculated and then probe is removed from exhaust duct. Now load is applied to engine by rope belt and emissions are calculated by gas analyser. Engine emissions are calculated at different speeds i.e. 1800, 2200 and 2600 rpm. Now engine is filled with dual fuel but before that engine is allowed to cool to room temperature and then engine is first started at diesel pilot fuel to warm the engine for five minutes and then natural gas is allowed to travel to gas regulator through high pressure fuel line.

6 RESULTS AND DISCUSSION

The engine performance parameters are calculated at various operating loads first at diesel engine and then at dual fuel. The speed is fixed to 1800 RPM and angular velocity taken is 188 rad/sec. The engine performance parameters involves Torque (τ), Angular velocity (ω), Brake power (BP), Input power (P_i), Thermal efficiency (η_d), Mass flow rate (m_f) and Inlet temperature (T_i), Exhaust temperature (T_e), Cooling temperature (T_c) are also measured for both types of fuel. The diameter of wheel is 0.34 m, Brake power is calculated by eq. 3, Power input is calculated by eq.2, and Thermal efficiency is calculated by eq. 7. Table 1 shows the engine performance parameters for diesel engine. The diesel fuel consumed is 50mL. When no load is applied engine timing was 10 min whereas input power for diesel was 850 kW, input power for gas was 34785kW, inlet temperature was 36°C, exhaust temperature was 155°C, mass flow rate was 0.000083 lt/sec and engine cooling temperature was 58°C and with increasing load the timing reduced while other parameters increased.

Table 1: Engine performance parameters for diesel engine

Test#	Load	t/min	τ	N/m	BP/W	Pi diesel/kW	Cost	ηf	Ti/°C	Te/°C	mf/lt/sec	Tc/°C
1	0	10	0	0		850	Rs.4	0	21	120	0.00000833	58
2	5	5	0.9	160		1700	Rs.4	2.26%	26	155	0.00000167	68
3	10	3	1.7	320		3400	Rs.4	2.26%	36	220	0.00000333	80

Table 2 shows the engine performance parameters for dual fuel. The diesel fuel consumed is 12mL. Time of first test is 0 minutes and brake power is 0, time of second test is 5 minutes and brake power is 160 and time of third test is 3 minutes and brake power is 320. When no load is applied engine timing was 10 min whereas input power was 850 kW, inlet temperature was 21°C, exhaust temperature was 120°C, mass flow rate for diesel 0.00004 lt/sec, mass flow rate for gas was 0.00073 lt/sec and engine cooling temperature was 82°C and with increasing load the timing reduced while other parameters increased.

Table 2: Engine performance parameters for dual-fuel engine

Test#	Load	τ/Nm	Pi diesel/kW	Pi gas/kW	Total cost	ηf	Ti/°C	Te/°C	mf/liter	mf gas/milliter	Tc/°C
1	0	0	850	34785	3	0	26	155	0.00082	0.00073	82
2	5	0.9	1700	69570	3	0.20%	30	230	0.00064	0.00054	90
3	10	1.7	3400	139140	3	0.20%	40	260	0.00088	0.00038	107

Graph 1 clearly shows that with constant increase of load the exhaust temperature also increased for both type of fuel.

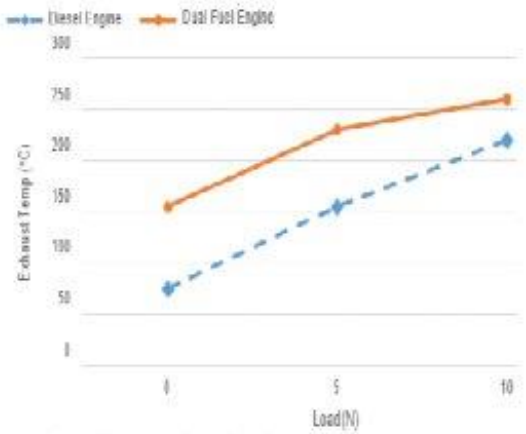

Graph 1: Load and Exhaust Temperature at Constant Speed of 1800 RPM

Graph 2 shows that with constant increase of load the water cooling temperature increases whereas for dual fuel water cooling temperature is more than diesel fuel. Graph 3 shows that with increasing load the consumption of diesel fuel in diesel engine was more than diesel in diesel fuel. Graph 4 shows that cost of fuel consumption in diesel engine is greater than the dual fuel engine. Graph 5 shows that with increasing load the thermal efficiency increases for diesel fuel than dual fuel.

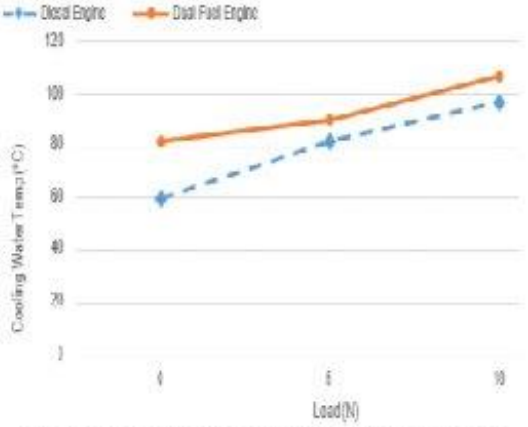

Graph 2: Load and Cooling water Temperature at Constant Speed of 1800 RPM

Graph 6 shows that mass flow rate of diesel in diesel engine is greater than the mass flow rate of diesel in dual fuel engine. Graph 7 shows that diesel engine requires more input power than the dual fuel engine and with the constant increase in the load the input power also increases.

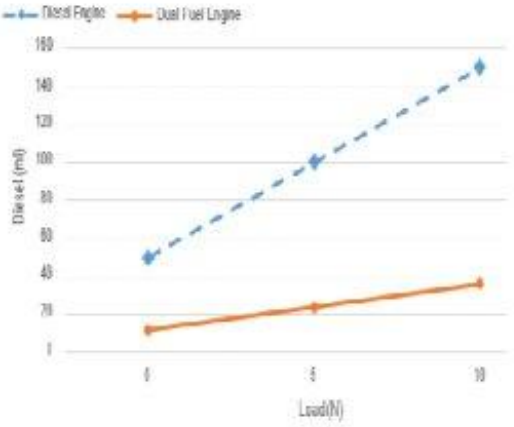

Graph 3: Diesel Fuel Consumption v/s Load at Constant Speed of 1800 RPM

In second case torque and brake power are calculated at changing speed for both types of fuel and at fixed load. Table 3 shows the engine parameters for diesel fuel.

Table 3: Engine parameters for diesel fuel

Test #	RPM	t sec	BP kW	τ N.m
1	1600	78	1.173	7
2	1800	69	1.6967	9
3	2000	64	1.8852	9

Table 4: Engine performance parameters for dual-fuel.

Test #	RPM	t sec	BP kW	τ N.m
1	1600	290	1.3406	8
2	1800	249	1.8852	10
3	2000	230	2.0947	10

Table 4 shows the engine performance parameters for dual fuel. Time decreased with increasing speed and due to that brake power and torque also increased for both types of fuel. Graph 8 shows that the time consumption of fuel in dual fuel engine is greater than the time of diesel engine because in dual fuel engine the mass flow rate also decreases. Graph 9 shows that when we increases the speed rpm of the engine its brake power also increases when the load remains constant. In this graph it can be seen that brake power developed in the dual fuel engine is greater than the diesel engine.

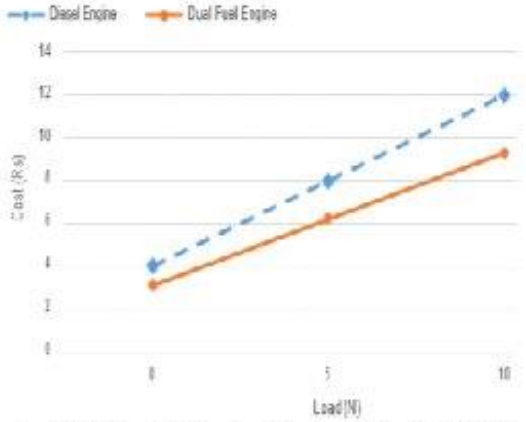

Graph 4: Cost v/s Load at Constant Speed of 1800 RPM

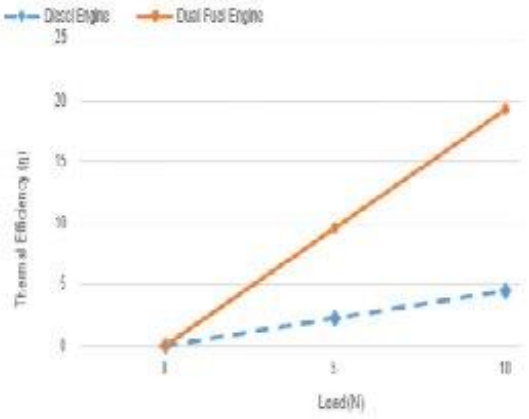

Graph 5: Thermal efficiency v/s Load at Constant Speed of 1800 RPM

Graph 10 shows that when the number of rpm increase, brake power increases and torque also increases, in this graph it can be seen that torque produced by dual fuel engine is greater than the torque produced in the diesel engine.

6.1 ENGINE EXHUAST EMISSIONS FOR MAXIMUM LOAD OPERATING CONDITIONS

The exhaust emissions has been measured with variable speed for diesel and dual-fuel engine. The calibrated gas analyser is used for measuring the emissions from exhaust gases of the engine i.e. CO, HC, NO_x, CO_2, and O_2.

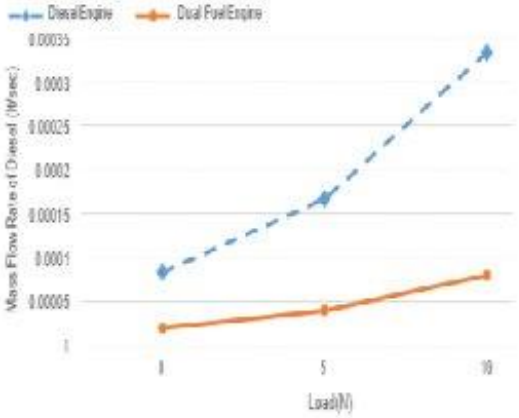

Graph 6: Mass flow rate of diesel v/s Load at Constant Speed of 1800 RPM

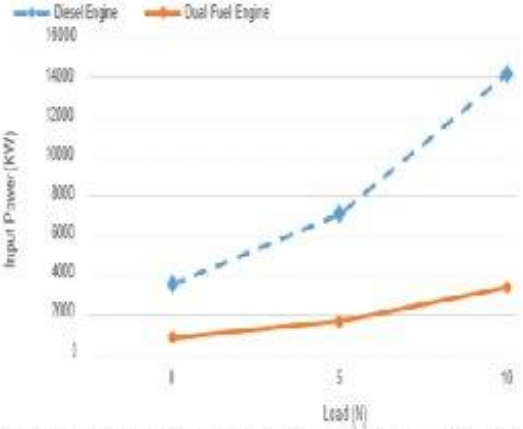

Graph 7: Input power of diesel v/s Load at Constant Speed of 1800 RPM

Table 5 shows exhaust data comparison of diesel and dual fuel engine under maximum load operating conditions.

Table 5: Exhaust data comparison of diesel and dual fuel engine under maximum load operating conditions

RPM	Diesel						Dual-Fuel			
	CO (ppm)	HC (ppm)	NOx (ppm)	CO2 (%)	O2 (%)	CO (ppm)	HC (ppm)	NOx (ppm)	CO2 (%)	O2 (%)
1600	122	758	70	2.4	17.7	36	4005	15	1.3	15.7
1800	117	566	96	2.9	17.3	42	3467	26	1.7	15.1
2000	83	922	155	3.2	14.3	55	3084	50	2.20	12.7

CO emissions reduces for diesel engines that operate between 1600 rpm to 2300 rpm because temperature of body and exhaust increases and complete combustion occurs. CO emissions increases when diesel engine operates above 2600 rpm because of knocking factor. The results show that CO emissions decrease for dual fuel because natural gas combustion efficiency is higher than liquid fuel but under high loading conditions the CO emissions rise but still less than diesel fuel as shown in graph 11. Graph 12 shows that level of unburnt HC is higher in dual fuel than diesel fuel whereas at high speed dual fuel produce less unburnt HC but still higher than diesel engine.

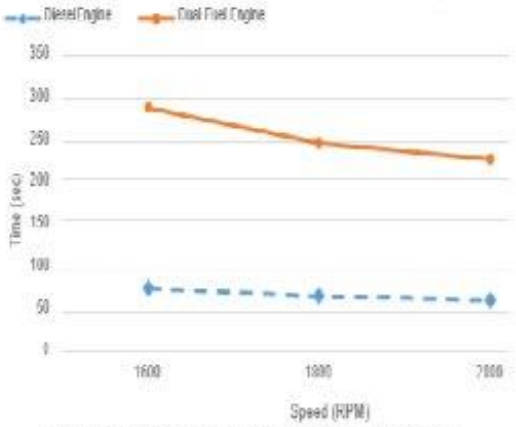

Graph 8: Speed RPM v/s Time of Diesel Consumption

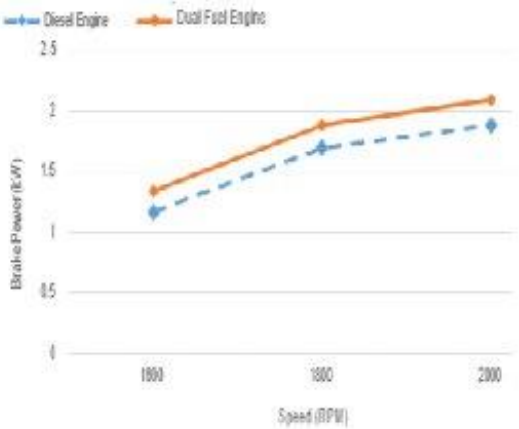

Graph 9: Speed RPM v/s Brake Power

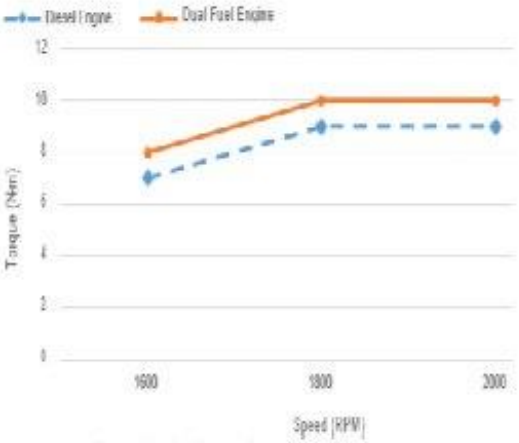

Graph 10: Speed RPM v/s Torque

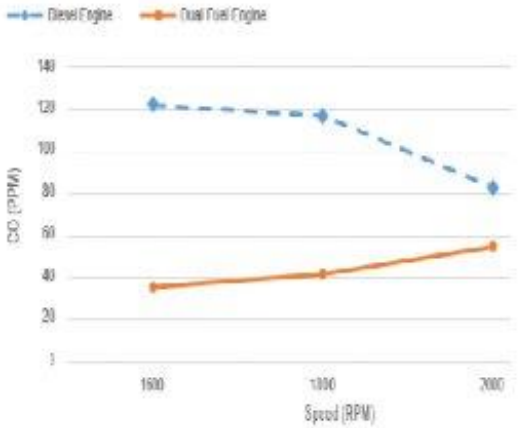

Graph 11: CO Emission of Diesel and Dual-Fuel Engine

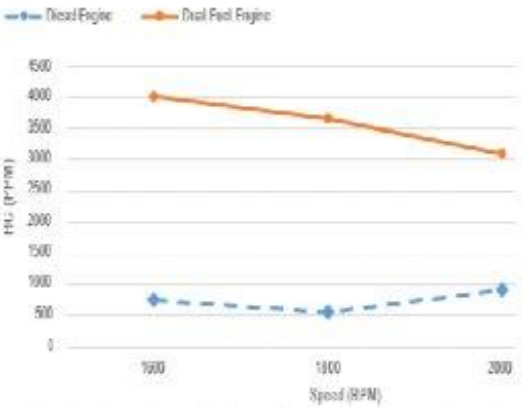

Graph 12: HC Emission of Diesel and Dual-Fuel Engine

Graph 13 shows that level of NO_x reduces for dual fuel when compared with diesel fuel. The NO_x emissions reduces by 58%. Whereas NO_x emissions rise for both fuels when engine is operated at maximum loading conditions. Graph 14 shows that the CO_2 emissions are reduced for dual fuel by an average of 1.16 % when operated under high loading condition. The reduction in CO_2 emissions is observed when engine is at speed of 2200 rpm almost by 2.2%. The reduction in CO_2 emissions for dual fuel is due to fact that natural gas contains less carbon atoms than diesel fuel.

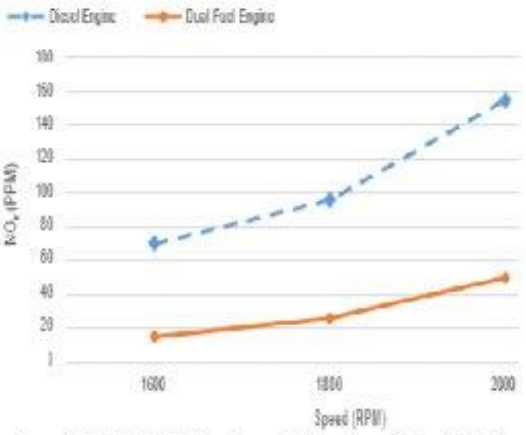

Graph 13: NO_x Emission of Diesel and Dual-Fuel Engine

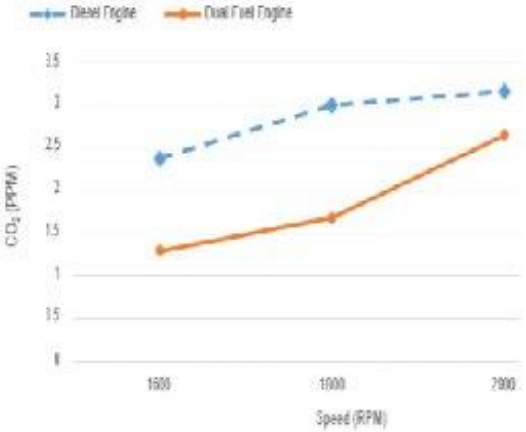

Graph 14: CO_2 Emission of Diesel and Dual-Fuel Engine

Graph 15 shows that level of excess O_2 decreases for dual fuel by 1.9% when engine operating at speed between 1600 rpm to 2600 rpm as compared with diesel. The results further indicate that combustion of dual fuel is better and leads to lower level of excess O_2.

6.2 ENGINE EXHUAST EMISSIONS FOR MODERATE LOAD OPERATING CONDITIONS

Now exhaust emissions are observed and compared between dual fuel and diesel fuel for moderate load operating conditions.

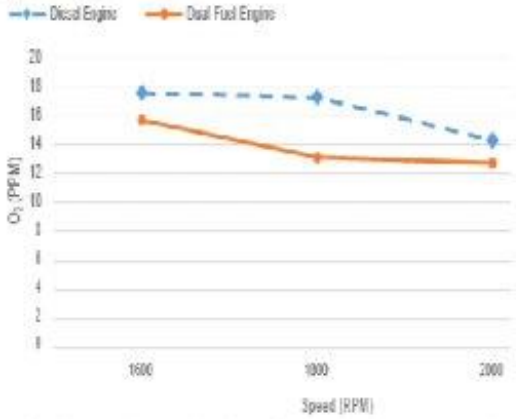

Graph 15: O_2 Emission of Diesel and Dual-Fuel Engine

The gas analyser has been used for measuring different pollutants. Table 6 shows exhaust data comparison of diesel and dual fuel engine under moderate load operating conditions.

Table 6: Exhaust data comparison of diesel and dual fuel engine under moderate load operating conditions

RPM	Diesel					Dual-Fuel				
	CO (ppm)	HC (ppm)	NOx (ppm)	CO2 (%)	O2 (%)	CO (ppm)	HC (ppm)	NOx (ppm)	CO2 (%	O2 (%
1600	68	1984	65	2.19	19.04	14	4857	18	1.25	18.9
1800	72	1776	87	2.47	18.41	29	4215	25	1.58	17.4
2000	79	1682	106	2.38	17.24	38	3259	29	1.97	17.7

Under moderate loading conditions CO emissions are reduced by 58 % at 1600 rpm speed for dual-fuel. The reduction level increases by 79.4% when compared with diesel fuel. CO emissions produced are less when engine operates at moderate loading conditions as compared with maximum loading conditions as shown in graph 16.

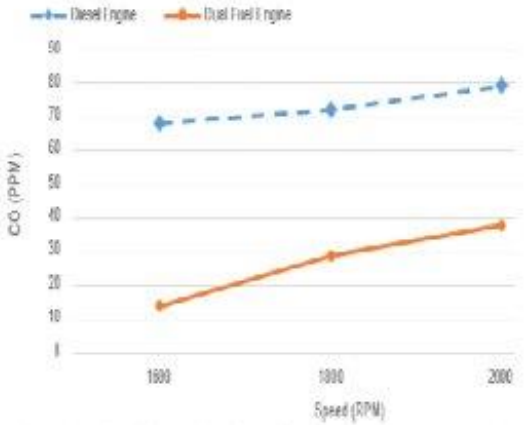

Graph 16: CO Emission of Diesel and Dual-Fuel Engine

Under moderate loading condition the dual fuel at speed of 1600 rpm produces unburnt HC that are 145% higher than diesel. As compared to maximum loading conditions the level of unburnt HC is 96 % higher for diesel and 10.5% higher for dual fuel as shown in graph 17.

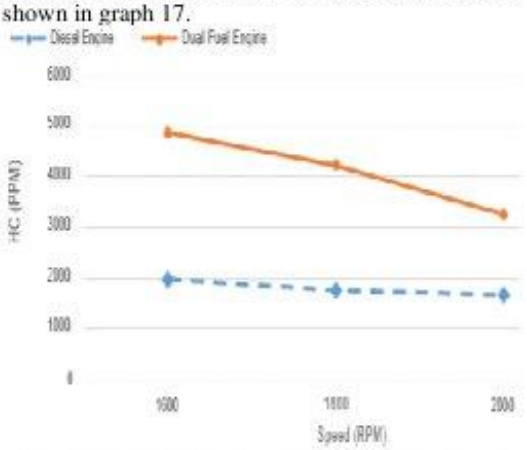

Graph 17: HC Emission of Diesel and Dual-Fuel Engine

Under moderate conditions the level of NO_x reduces by 68.2% which is result of lower combustion temperatures. As compared with maximum loading conditions NO_x emissions are reduced for diesel by 10.7% and for dual-fuel by 22.5% as shown in graph 18.

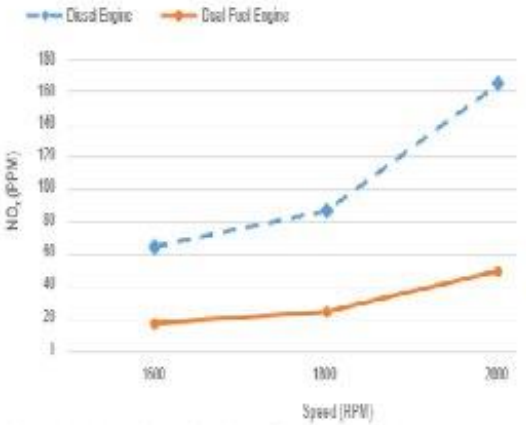

Graph 18: NO_x Emission of Diesel and Dual-Fuel Engine

As compared with maximum loading conditions CO_2 emissions are reduced by an average of 0.65% for moderate loading conditions as shown in graph 19. The high level of oxygen is present as compared with maximum loading conditions. The difference between diesel and dual fuel is only 0.13% as shown in graph 20.

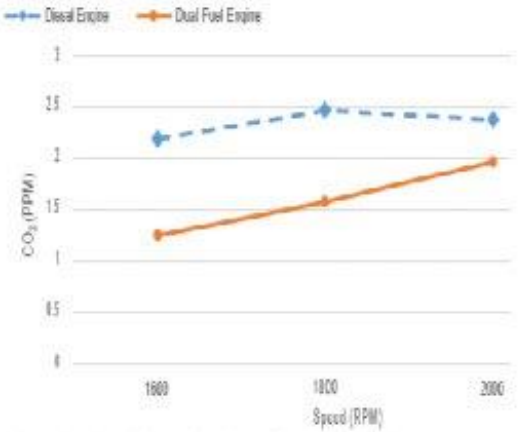

Graph 19: CO_2 Emission of Diesel and Dual-Fuel Engine

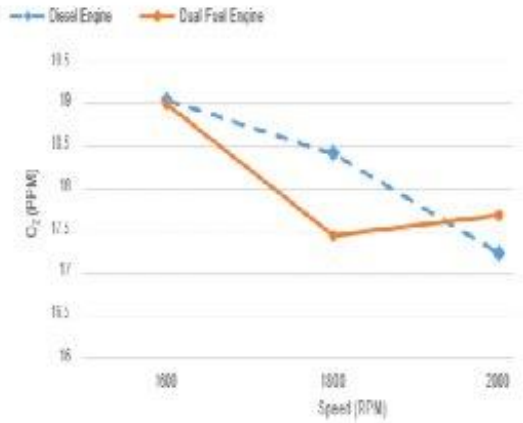

Graph 20: O_2 Emission of Diesel and Dual-Fuel Engine

7 CONCLUSION

In order to achieve the project objectives the modification in diesel engine has been obtained by installing a conversion kit in order to operate on CNG. Now the engine can operated on dual-fuel. This dual-fuel based engine can utilize the diesel as a pilot fuel. After running the engine and taking experimental output from engine in terms engine performance and emissions. As the experimental result has been achieved on different operating loads. It has been observed from results of torque, brake power and efficiency of engine that the performance of engine is increased by using dual-fuel operation based engine. Therefore, the specific fuel consumption is also reduced. It is also observed from experiments results of emission that there is subsequent reduction in CO, CO_2, NO_2 and exhaust excess oxygen level. As we know that the cost of natural gas is much less than the cost of diesel. Therefore, it is analyzed that we are saving the cost in terms fuel and the payback period of energy conversion kit can be reduced with this ambitious savings. Moreover, it is highly recommended for future work that the compression ratio of diesel engine we have used in our laboratory must be increased to carry out more fruitful research and increase the thermal efficiency.

ACKNOWLEDGEMENTS

The author would like to thank to Mechanical Engineering department, QUEST Nawabshah to provide the lab facilities.

REFERENCES

[1] Walsh, Michael P. *Global Trends in Motor Vehicle Pollution Control-A 1988 Perspective*. No. 890581. SAE Technical Paper, 1989.

[2] Riffkin, J. "Town Gas as a Fuel in the Compression-Ignition Engine." Gas & Oil power (1937).

[3] BOYER, RALPH L. Status of dual fuel engine development. No. 490018. SAE Technical Paper, 1949.

[4] EPA, 'Analysis of the Economic and Environmental Effects of Compressed Natural Gas as a Vehicle Fuel, Volume I (Passenger Cars and Light Trucks) and Volume 2 (Heavy Duty Vehicles) April, 1990, Special Report of Environmental Protection Agency - Office of Mobile Sources.

[5] EPA, "Standards for Emissions from Natural Gas-Fuelled and LPG-Fuelled Motor Vehicles and Motor Vehicle Engines and Certification Procedures for Aftermarket Conversion Hardware, Notice of proposed rulemaking, 40 CFR Parts 85,86 and 600, December 1992.

[6] Goetz, W. A., D. Petherick, and T. Topaloglu. Performance and emissions of propane, natural gas, and methanol fuelled bus engines. No. 880494. SAE Technical Paper, 1988.

[7] Wang, Quanlu, Daniel Sperling, and Janis Olmstead. "Emission control cost-effectiveness of alternative-fuel vehicles." (1993).

[8] Gunea, Catalin Dragos. Examination of the effects of pilot fuel quality on the performance of gas fuelled diesel engines. Calgary, 1997.

[9] Kato, Makoto, Kunihiko Masunaga, and Hirohiko Hoshi. The influence of fuel qualities on white smoke emissions from light-duty diesel engine. No. 870341. SAE Technical Paper, 1987.

[10] Lepperhoff, Gerhard, Michael Houben, and Hellmut Garthe. Influences of Future Diesel Fuels on Combustion and Emissions of a Dl-Diesel Engine. No. 872244. SAE Technical Paper, 1987.

[11] Karim, G.A., "An Examination of Some Measures for Improving the Performance of Gas Fuelled Diesel Engine at Light Load", SAE 912366, 1991.

[12] Nielsen, O.B., Qvale, B. and Sorenson, S., "Ignition Delay in the Dual Fuel Engine", SAE Trans. 870589, Vol. 96, Sect. 5, 1987.

[13] Turner, S.H. and Weaver. C.S., "Dual-Fuel Natural Gas/Diesel Engines: Technology, Performance and Emissions" Gas Research Institute, Topical Report No. 9410094, Nov. 1994.

[14] Burn, K.S. and Karim, GA., "The Combustion of Gaseous Fuels in Dual Fuel Engines of the

Compression Ignition Type with Particular Reference to Cold Intake Temperature Conditions", SAE 800263, 1980.

[15] Karim, G.A. and Amoozegar, N., "Examination of the Performance of a Dual Fuel Diesel Engine with Particular Reference to the Presence of Some Inert Diluents in the Engine Intake Charge", SAE 821222, 1982.

[16] Karim, GA, Jones, W. And Raine, R.R., "An Examination of the Ignition Delay Period in Dual Fuel Engines", SAE 892140, 1989.

[17] Lewis, J.D., "A Study of Combustion Process in the Dual-Fuel Engine by Exhaust Gas Analysis Methods", Ph.D. Thesis, London University, 1954.

[18] Felt, AE. and Steele Jr.,W.A, "Combustion Control in Dual Fuel Engines", SAE Trans. Vol.70, 1962.

[19] Karim, G.A., "Combustion in Dual Fuel Engines"- Proceedings, 8th International Congress on Combustion, CIMAC, Bruxelles, May 1968.

[20] Clark, J.S. and Bunch, H.M., "Dual Fuel Combustion of Propane in a Railroad Diesel Engine", SAE Trans., Vol. 71, 91-1 01, 1963.

[21] Karim, G.A. and Rogers, A., "Comparative Studies of Propane and Butane as Dual Fuel Engine Fuels", Journal of the Inst. Of Fuel, Nov. 1967.

[22] Karim, GA. and Klat, S.R., 'Hydrogen as a Fuel in Compression Ignition Engines", Mechanical Engineering, April 1976.

[23] Turner, S.H. and Weaver. C.S., "Dual-Fuel Natural Gas Diesel Engines: Technology, Performance and Emissions" Gas Research Institute, Topical Report No. 9410094, Nov. 1994.

[24] Liu, Z., "An Examination of the Combustion Characteristics of Compression Ignition Engines Fuelled with Gaseous Fuels", Ph.D. Thesis, Dept. of Mech. Eng., Univ. of Calgary, 1995.

[25] Liu, Z. and Karim, G.A., "Simulation of Combustion Processes in Gas-Fueled Diesel Engines", Proceedings of Institution of Mechanical Engineers, Journal of Power and Energy, Vol. 21 1, No. A2, 159-1 69, 1997.

[26] Ding, X. and Hill, P., "Emissions and Fuel Economy of a Pre-chamber Diesel Engine with Natural Gas Dual Fuelling", SAE Trans. 86069, Vol.95, Sect. 6, 1986. 13. Eliott, M.A and Davis, R.F., "Dual Fuel Combustion in Diesel Engine" Ind. and Eng. Chem. Vol. 43, No.12. 1951.

[27] Barbour, T.R., Crouse, M.E. and Lestz, S.S., "Gaseous Fuel Utilization in a Light- Duty Diesel Engine", SAE Trans. 860070, Vol. 95, Sect. 6, 1986.

SOL-GEL BASED SYNTHESIS OF NEW PEROVSKITE MATERIAL

Syed Raheel Adeel[1,*] Murtuza Mehdi[2,*] Maaz Akhtar[3*]
[1]Mechanical Engineering Department, NED University of Engineering & Technology, Karachi, Pakistan

[*]Corresponding author. Tel.: +92-21-99261261-8 (Ext: 2330)
E-mail address: drmurtaza@neduet.edu.pk

ABSTRACT

This paper is about the current research of synthesis of perovskite material. Many others synthesis procedures, have been adopted for synthesis of perovskite but by sol-gel method is more effective and inexpensive method. Sol-gel technique is widely being used in synthesis of nanoparticles and has a versatility in material science. Sol-gel transformation is based on complex ions formation. It is recognised that this method involves a multiple modification from solution to high temperature curing.

Perovskite materials are known to manifest clearly many properties including ferroelectric, ferromagnetic, piezoelectric, electro-optic, dielectric etc. These materials have remarkable application in solar cells, sensors, actuators, transducers, capacitors etc. Triple cations perovskite, are being synthesized to develop high stable and efficiency solar cells.

Perovskite material based on magnesium, copper and manganese oxide powder, having the general formula ABO_3, where A is generally an alkali or alkaline earth metal and B is a transition metal. But according to general formulation, A is the cation having ionic radius greater than that of B cation.

1 INTRODUCTION

Perovskite oxide nanocrystals exhibit a wide spectrum of attractive properties such as ferroelectricity, piezoelectricity, dielectricity, ferromagnetism, magneto-resistance, and multiferroics. These properties are indispensable for applications in ferroelectric random access memories, multilayer ceramic capacitors, transducers, sensors and actuators, magnetic random access memories, and the potential new types of multiple-state memories and spintronic devices control- led by electric and magnetic fields.[1]

Inorganic perovskite-type oxides are fascinating nanomaterials for wide applications in catalysis, fuel cells, and electrochemical sensing. Perovskites prepared in the nanoscale have recently received extensive attention due to their catalytic nature when used as electrode modifiers. The catalytic activity of these oxides is higher than that of many transition metals compounds and even some precious metal oxides. They exhibit attractive physical and chemical characteristics such as electronic conductivity, electrically active structure, the oxide ions mobility through the crystal lattice, variations on the content of the oxygen, thermal and chemical stability, and super-magnetic, photocatalytic, thermoelectric, and dielectric properties.[2]

The method, based on a sol–gel process is characterized by its simplicity, reduced sintering time, mass production, high level of repeatability and a low industrialization implementation cost.[3]

By sol-gel process, perovskite material are prepared in powder form, then in thin film form to check its properties. Among all the advantages of sol-gel method are easier fabrication of large area thin films, low cost, and a short fabrication cycle.

This paper is concerned with the synthesis of new perovskite material by sol-gel method.

2 EXPERIMENT

To develop new perovskite material consisting of triple metal cations Mg, Cu & Mn. We have precursor materials like acetate salts of copper, magnesium & manganese, ethanol as a solvent and citric acid as a chelating agent.

By taking all these precursor materials in particular stoichiometry amount. And dissolve each salt separately in ethanol under constant magnetic stirring. Then followed by mixing of solutions and again placed on magnetic hot plate for constant stirring. See figure 1.

Figure 1: Ethanolic solution of precursor materials

Chelating agent plays an important role in gel formation, because it forms bonding between metals ions or by complex ions formation. However, it depends on which chelating agent to be use. As in this experiment, we used two chelating agents i.e. oxalic acid and citric acid one at a time for gel formation.

In order to form transform solution to gel, oxalic acid was used as a chelating agent, but it reluctant to formation of gel, because it formed copper oxalate as a precipitate, which settled down in the solution and then separated it by filter paper. See figure 2.

Figure 2: Copper oxalate precipitate

To prevent precipitation, we used citric acid as a chelating agent, adding its solution on mixed solution of precursors under constant stirring and heating to form gel by evaporating ethanol. See figure 3. After gel formation, it dried by placing on magnetic hot plate and curried further to perovskite powder.

Figure 3: (a) Mixed solution of all precursors' solution, (b) Mixed solution under constant stirring, (c) Before adding citric acid solution in mixed solution, (d) After adding citric acid solution.

2.1 Equation

The stability and distortion of perovskite crystal structure can be predicted by using Goldschmidt Tolerance Factor.

$$t = \frac{r_A + r_o}{\sqrt{2}(r_B + r_o)}$$

According to this factor: "The value of "t" should be within 0.75 to 1. Otherwise, stable perovskite structure will not be formed".

As this equation, ionic radius of A cation r_A is greater than that of B cation r_B and r_O is the ionic radius of anion of oxygen i.e. O^{-2}.

For this perovskite consisting of magnesium, copper and manganese ions, the value of "t" lies in required range of 0.75 to 1.

3 RESULTS

By using citric acid, mixed solution of all precursors transformed to gel. See figure 4. It ensured that all three cations are present in this gel in a complex form rather than precipitation. Because precipitate formation is the failure of

J. Cerda`*, J. Arbiol, R. Diaz, G. Dezanneau, J.R. Morante "Synthesis of perovskite-type BaSnO3 particles obtained by a new simple wet chemical route based on a sol–gel process" Published: January 2002. Materials Letters-Journal-Elsevier.

GROWTH OPTIMIZATION BY ANALYZING SUSTAINABILITY COMPONENTS: A CASE STUDY OF CERAMICS INDUSTRY

Muhammad Waseem[1,*] Qazi Muhammad Usman Jan[2] Irfanullah[3]
[1]Aerospace Engineering Department, College of Aeronautical Engineering, National University of Science and Technology, PAF Academy Asghar Khan, Pakistan
[2]Industrial Engineering Department, College of Aeronautical Engineering, National University of Science and Technology, PAF Academy Asghar Khan, Pakistan
[2]Industrial Engineering Department, University of Engineering and Technology, Peshawar, Pakistan

[*]Corresponding author. Tel.: +92321-9081489

E-mail address: mw9722299@gmail.com (Muhammad Waseem)

ABSTRACT

In today's industrialization era manufacturing companies are realizing and treating sustainability as an important objective to increase growth and competitiveness. Sustainability in manufacturing is the creation of products not only through economically sound processes but minimizing the environmental impacts and considering the social aspects as well. This study develops a framework and applied it to a local industry related to ceramics. The framework is mainly based on the three aspects of environmental, social and economic parameters of sustainability in order to investigate and measure the current state of the company in the areas of energy utilization, machines availability, hazardous emissions etc. By measuring the current state from the sustainability framework shows that the case company is 33% sustainable having the product sustainability index (PSI (TLC)) value of 33% which lies in poor category. The suggesting improvements in relation to the aspects of sustainability will support to increase their operational efficiency, reduce costs and waste, and give competitive advantage for environmental friendly manufacturing processes.

Keywords: Economic Sustainability, Environmental sustainability, product sustainability index (PSI) and optimization.

1. INTRODUCTION

Sustainable manufacturing efforts are aiming to reduce the resource consumption through improved efficiency in manufacturing processes, decrease the amount of waste and emissions and reduce the energy consumption through manufacturing activities. In recent years large number of companies realizing the benefits of sustainable manufacturing. As it is related to the making of fabricated items through financially stable procedures and reduces the negative ecological effects. For

the next generation manufacturing systems, it is necessary to adopt, integrate and implement the latest approaches to achieve economic benefits for all stakeholders [1].

Among the basic materials, ceramic is an important class of material used mainly in the building construction. In the last few decades its production output is constantly increasing due to increase in its demand. There is a negative impact on environment due to increase in production [2]. During the production of ceramic tiles large amounts of energy intake are required and high amount of pollutants are discharged, which adversely impact the environment [3]. Due to the growing demands of environmental friendly products, many researchers have worked on to reduce the energy intake and pollutants to the environment. These studies include improving the material used in ceramics tiles, controlling and monitoring the manufacturing processes, used various approaches to minimize the emissions and carried out life cycle assessment of the production processes [4].

It has been observed that the local ceramics industry is based on traditional manufacturing processes and faces problems related to energy utilization, machines availability, hazardous emissions etc. Therefore there is a need for sustainability analysis of ceramic industry. In this paper sustainability analysis of FORTE tiles is performed by measuring the factors that impact sustainable production processes and suggestions for optimization to enhance growth and competitiveness with respect to its market and in their process.

2. Literature Review

Manufacturing companies must follow sustainability measures as a strategic goal. This could be achieved to perform a sustainability assessment of the products and manufacturing processes [5, 6]. This assessment must involve measurements of resource utilization, pollution emission, waste generation in all manufacturing activities. Measurements must use performance metrics and approaches for computing them. Impact analysis must be compared against the industry standards.

[7] discussed that sustainability assessment is associated with the family of impact assessment tools. [8] added a technological view and proposed that an integrated assessment is "to assess the social, environmental, technological, and economic dimensions of projects, policies, and programs." The researchers provided the approaches to describe sustainability assessment. These approaches aim to support decision making to satisfy social, environmental, and economic goals. Various authors [2, 9] researched on the social, economical and environmental aspects to identify the key problems regarding sustainability; developed techniques and methods to address these concerns, and developed sustainability indicators to assess and improve overall performance etc.

Literature shows that researchers have worked on various aspects of sustainability, this research advance the discussion on the topic to develop a framework to assess the current practices in a company that impact the product life cycle and its manufacturing in addition give suggestions for optimization regarding sustainable processes.

3. METHODOLOGY

Initially, the study focuses on the application of sustainability in the ceramic industry. We observed that local ceramic industries are based on traditional manufacturing processes without considering the sustainability effects on manufacturing processes. For this purpose data is collected in four phases of the product development process namely pre manufacturing,

manufacturing, usage and post usage phases. Then the assessment of the sustainability components is performed using the product sustainability index. The sustainability index identifies weak areas and the factors that impact the production processes. Based on this framework; suggestions are proposed that will improve the current state of the manufacturing process.

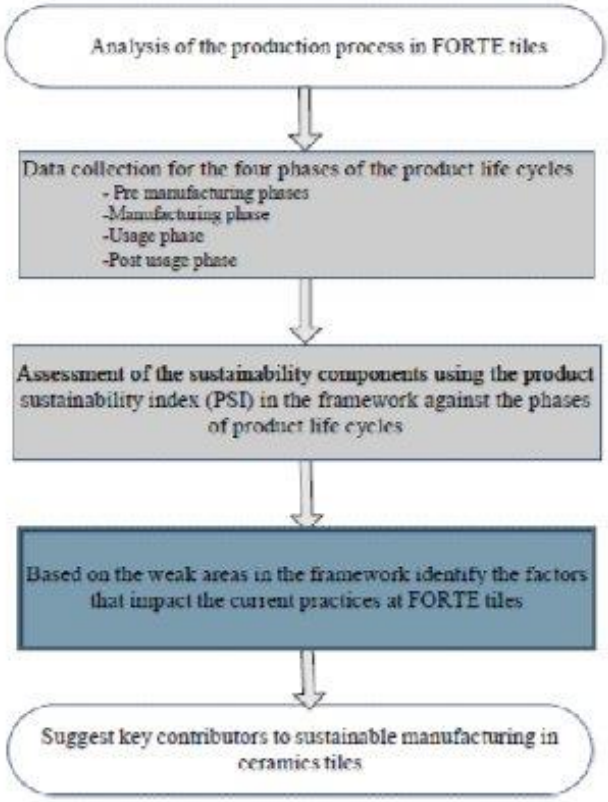

Figure 1. Research Methodology

4. INTRODUCTION TO CASE COMPANY

Frontier Ceramics is a private company popularly known as FORTE. The FORTE brand in market is recognized for Ceramic Tiles manufacturing. FORTE tiles has dealership network with more than 60 authorized dealers across Pakistan. In 2006 the group has taken Frontier Ceramics Limited. The company is expert in the manufacturing of ceramic tiles having a brand name "FORTE" which has created greater trust and loyalty within the marketplace.

The company has a huge work force of almost 500 workers. It operates 24 hours a day in 4 shifts and has a daily production capacity of almost 6000 sq meter tiles. The

company has a big setup which is divided into following major departments:

- Administration
- Research and Development Center
- Raw Material Inventory
- Body Preparation Section
- Production Section
- Maintenance Department
- Finished Goods Inventory

4.1. Process Flow Chart

The main steps in the process of manufacturing ceramics tiles by FORTE Company are shown in the following flow chart which is in fig.2.

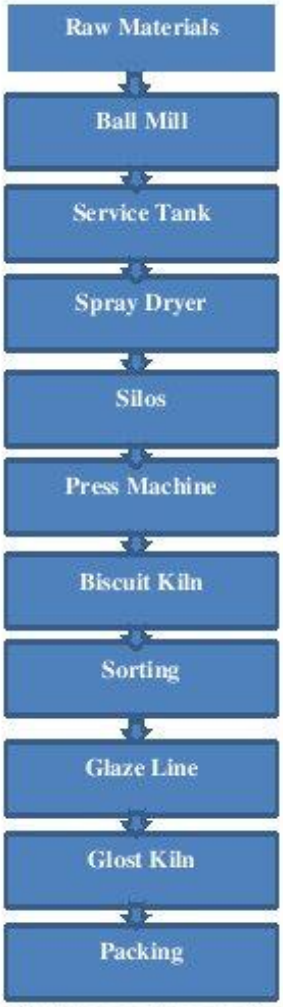

Figure 2. Process Flow chart at FORTE

The process starts from scaling raw materials which is sent to body section where ball mills are used for mixing and grinding the raw material shows in fig.

Figure 3. Raw Material for Tile Production

The ball mill make slip from the raw material (see fig 3) which is transferred to storage tanks. In the followed step, the slip is injected into the spray dryer which evaporates water from the slip and converts it into powder form. The powder having desired amount of moisture is transferred through a conveyor belt to silos for storage. The mixture from the silo is continuously transferred to a tank above the press machines. At this point the discrete manufacturing system of the factory starts.

Figure 4. Press Machine Presses the Powder into the Desired Size

The press machines (see fig 4) presses the powder into desired size. After pressing the powder the tile called green biscuit is produced. The tile transfers through conveyer belts towards brushing section which removes dust from the tiles and forward to the kiln (see fig 5) for heating and removing moisture. Through conveyer these tiles are transferred towards the inspection section. In this section the strength of each tile is checked, the weak tiles fell from the conveyer and the hard tiles passes under the brushes again to remove dust and make the surface clean. These tiles are transferred towards engobe and glazing section, and then it is transfer towards the printing section where the tiles are printed by a desired colors and designs. Then the tiles are transfer towards the rollers where batches of nine and eleven are made and then the roller transfer the batches towards the second kiln where it again get heated.

Figure 5. Process Kiln to Heat the Tiles

Finally, the tiles are transferred towards sorting section where the workers sort the tiles into five types namely:

- Classic
- Standard
- Commercial
- Sub-standard
- Waste

After sorting; the workers pack different types of tiles in different boxes and then it is transferred to store shows in fig.

Figure 6. Tile Packing for storage

5. SUSTAINABILITY FRAMWORK

The product sustainability index (PSI) which is the weighted sum of different sub-indicators of three main sustainability indicators, is a method proposed by Jaafar. [10] We used this index in the framework to measure the sustainability components. For example, at manufacturing phase, the PSI value of societal indicator is calculated using equation (1).[10]

$$PSI_{(so\_mn)} = \left\{\frac{\left[\sum_{i=1}^{n} IF_{(so\_mn)}\right]}{n\times 5}\right\} \times 100\% \qquad (1)$$

Where,

$IF_{(so\_mn)}$ = influencing factor ranges from 0-5 for the societal indicator at manufacturing phase.

n= number of influencing factors considered.

Similarly, the PSI values for environment PSI (en_mn) and economy PSI (ec_mn) components for various stages of production process can be calculated. In addition to that, sustainability components across all four life-cycle stages can be calculated by averaging the PSIs in the horizontal row for that particular sustainability component. The PSI value for a single indicator can also be calculated by taking the average of the sustainability components at different phases of production. Equation (2) is used to find out the total product sustainability index (PSI TLC).[10]

$$PSI_{TLC} = \frac{[PSI_{en} + PSI_{so} + PSI_{ec}]}{3} \qquad (2)$$

During different phases of product life cycle, the impact of indicators on sustainability is shown in the following framework.

Table 1. Weighting Criteria for the Different Parameters

Digits	Intangible Value	Digits	Intangible Value
0	Nil	3	Average
1	Poor/least	4	Above Average
2	Below Average	5	Excellent/Mostly

The above table 1 shows the weighting criteria for different parameters. The values ranging from 0 to 5 which show an impact from nil to excellent respectively. If a parameter has zero value it means that this parameter has no impact but if a parameter has a value of 1 it means the parameter has poor impact and so on. The highest impact of a parameter is represented by value of 5.

Table 2. Sustainability Analysis Framework in Ceramics Manufacturing Company.

		A Framework for Total Life Cycle Evaluation Using Sustainability Components								
		Pre Manufacturing Phase	Score Out of 5	Manufacturing Phase	Score Out of 5	Usage Phase	Score Out of 5	Post Usage Phase	Score Out of 5	
Sustainability Components	Environment	Raw Material Processing	2	Production	2	Material Disposals	3	Recyclability	0	
		Design for Environment	1	Hazardous Waste Produced	1	Intended Functionality	3	Remanufacturability	0	
		Quality of Raw Material	2	Smoke Emission	2	Hazardous waste generated	2	Redesign	0	PSI_{en} = 31
								Material Disposals	1	
		$PSI_{(en\_pre)}$ =	10.2222	$PSI_{(en\_man)}$ =	13.3333333	$PSI_{(en\_use)}$ =	12.222	$PSI_{(en\_pst)}$ =	5	
	Society	Worker Health	3	Work Ethics	2	Customer Feed Back	2	Reuse	0	
		Worker Safety	2.5	Ergonomics	1.5	Accomodate Consumer Requirements	2	Recovery	0	
		Ergonomics	2	Work Safety	1.5	Functional Improvement	1			PSI_{so} = 23
				Worker Health	2					
		$PSI_{(so\_pre)}$ =	10	$PSI_{(so\_man)}$ =	15	$PSI_{(so\_use)}$ =	15	$PSI_{(so\_pst)}$ =	0	
	Economy	Raw Material Cost	3	Production Cost	1.5	Product Cost	1	Recycling Cost	0	
		Transportation Cost	3	Packing Cost	2	Quality Cost	1	Remanufacturing Cost	0	
		Labor Cost	2	Cost due to accidents	1	After Sales Services cost	1	Disassembly Cost	0	
				Inventory Cost	1.5			Disposal Cost	0	
				Cost due to defects	1					PSI_{ec} = 39
				Energy Cost	2					
				Employees Training	1					
				Material Handling Cost	2					
		$PSI_{(ec\_pre)}$ =	10	$PSI_{(ec\_man)}$ =	10	$PSI_{(ec\_use)}$ =	6	$PSI_{(ec\_pst)}$ =	0	
		PSI_{ss} =	54.4444	PSI_{ss} =	62.7777777	PSI_{ss} =	31.111	PSI_{ss} =	5.555556	PSI_{ss} = 33
			Symbol							
			Score	Excellent (>=74%)	Good (<74% & >=60%)	Average (<60% & >=40%)	Poor (<40%)			

The framework measures the sustainability components with respect to the total life cycle in a manufacturing company. For FORTE tiles the overall product sustainability index (PSI (TLC)) value of 33% lies in poor category. The results also show how much the industry is sustainable under the three main components that is related to Environment, social and Economic aspects.

In this framework the PSI value for environment is 31%, PSI value for social component is 28 % and the PSI value for economic component is 39%. Similarly from the assessment of the four life cycle stages, usage phase and post usage phase have very poor values such as 31% and 1.67 % respectively. However pre manufacturing phase and manufacturing phase lies in the energy utilization, and no attention to quality will cause low quality production, loose customer confidence.

With the measurement of the key sustainability components with respect to total life cycle evaluation, it is possible to identify the factors that impact the current practices at FORTE tiles. Based on current practices suggestions for improvements are shown in the table 2.

average range with 54% and 42 % PSI value.

Based on this analysis, this company lies in poor category with respect to sustainability issues which needs an improvement in their production processes.

In the framework low score for environmental design, hazardous waste, no recycling, high emission will cause the environmental pollution, effect human health and increase the product cost. Similarly, no employee training, low score for accidents prevention, causes safety issues and impact overall productivity. Furthermore, low scores for functional improvements, high

Table 3. Current Practices at FORTE Ceramic Company and Suggestions for Improvement

Sustainability Indicators	**Current practices at FORTE company identified in the framework**	**How the current practices impact the production processes**	**Suggestions for improvement**
Environmental (PSI of 31% lies in a poor range)	Low score for environmental design Very low score for hazardous waste control in manufacturing process No recycling and remanufacturing of the tiles Low score for energy utilization and emission	Causes Environmental pollution May effect human health Increase in waste Increase energy utilization cost	Implement standard operating procedures Implement ISO 9000 and ISO 14000 quality standards Measures to reduce waste Reduce energy utilization and emissions

Societal (PSI of 28% lies in a poor range)	Low scores for any functional improvements	Reduce productivity and customer satisfaction	Employee training and involvement Mechanism for customer feedback
Economical (PSI of 39% lies in a poor range)	Low score for cost due to accidents Low quality cost Lack of employees training	Causes safety issues Low quality product Low production and quality	Health and safety strategies Improve scrap reduction *Improve productivity by measuring overall equipment effectiveness (OEE)

Overall equipment electiveness (OEE) is a useful measure of the efficiency and effectiveness of the manufacturing processes by measuring the Availability, performance and quality of the production machines.
The analysis from the framework and visual observations at the FORTE Company shows a lot of weak areas (Table 2) in the production of the ceramic tiles. In order to improve growth and competitiveness, key contributors to sustainable manufacturing in ceramics tiles are suggested in the following figure.

Figure 7. Key Contributors to Sustainable Manufacturing in Ceramics

From the optimization analysis in the framework it is clear that all the sustainability components against the four life cycle stages is having a very low scores such as 31%, 28% and 39% respectively. So this framework is a good indicator for the initial assessment of the sustainability components. In the FORTE tiles it is observed that there is no mechanism to assess and control the key indicators for sustainable processes. Therefore based on the analysis key contributors are suggested for sustainable practices in a ceramics industry.

6. CONCLUSION

On the basis of sustainability analysis, key parameters have been analyzed and a framework has been developed. Results from the sustainability framework shows that the case company is 33% sustainable having the product sustainability index (PSI (TLC)) value of 33% which lies in poor category. Similarly, according to three sustainability indicators the case company lies in poor category having low PSI values. The current practices in the FORTE tiles impact the sustainability with respect to economical, social and environmental domains. Low scores for environmental design, hazardous waste control and no recycling impact human health, increase in waste and energy utilization. Similarly very low scores for any functional improvements in product and processes and no feedback from the customers impact quality, production flexibility and customer faith in the product. Therefore, by measuring the current state and suggesting improvements in relation to the aspects of sustainability and implementing these results will increase competitive advantage for environmental friendly manufacturing processes in FORTE tiles.

7. REFERENCES

[1] Koren Y, Gu X, Badurdeen F, Jawahir I. Sustainable Living Factories for Next Generation Manufacturing. *Procedia Manufacturing*. 2018;21:26-36.

[2] Barros M, Bello P, Roca E, Casares J. Integrated pollution prevention and control for heavy ceramic industry in Galicia (NW Spain). *Journal of hazardous materials*. 2007;141:680-92.

[3] Bovea MD, Díaz-Albo E, Gallardo A, Colomer FJ, Serrano J. Environmental performance of ceramic tiles: improvement proposals. *Materials & Design*. 2010;31:35-41.

[4] Montero MA, Jordán M, Hernández-Crespo M, Sanfeliu T. The use of sewage sludge and marble residues in the manufacture of ceramic tile bodies. *Applied Clay Science*. 2009;46:404-8.

[5] Garetti M, Taisch M. Sustainable manufacturing: trends and research challenges. *Production planning & control*. 2012;23:83-104.

[6] Rosen MA, Kishawy HA. Sustainable manufacturing and design: Concepts, practices and needs. *Sustainability*. 2012;4:154-74.

[7] Ness B, Urbel-Piirsalu E, Anderberg S, Olsson L. Categorising tools for sustainability assessment. *Ecological economics*. 2007;60:498-508.

[8] Hasna AM. A review of sustainability assessment methods in engineering. *The International Journal of Environmental, Cultural, Economic & Social Sustainability*. 2008;5.

[9] García-Ten J, Monfort E, Gómez-Tena M, Sanz V. Use of coatings to minimise acid emissions during ceramic tile firing. *Journal of Cleaner Production*. 2011;19:1110-6.

[10] Jawahir I, Dillon O, Rouch K, Joshi KJ, Venkatachalam A, Jaafar IH. Total life-cycle considerations in product design for sustainability: A framework for comprehensive evaluation. *Proceedings of the 10th International Research/Expert Conference, Barcelona, Spain: Citeseer;* 2006. p. 1-10.

DESIGN AND ANALYSIS OF ALUMINUM MOULD FOR INJECTION MOLDING PROCESS OF POLYMERS

Qazi Muhammad Usman Jan[1,*] Sahar Noor[2], Tufail Habib[3] and Muhammad Waseem[4]

[1]Industrial Engineering Department, College of Aeronautical Engineering, National University of Science and Technology, PAF Academy Asghar Khan, Pakistan

[2]Industrial Engineering Department, University of Engineering & Technology, Peshawar, Pakistan

[3]Industrial Engineering Department, University of Engineering & Technology, Peshawar, Pakistan

[4]Aerospace Engineering Department, College of Aeronautical Engineering, National University of Science and Technology, PAF Academy Asghar Khan, Pakistan

*Corresponding author. Tel.: +92333-9303877

E-mail address: usmankazi999@gmail.com (Qazi Muhammad Usman Jan)

ABSTRACT

Plastic injection moulding process is an important manufacturing operation in plastic industry. However, lack of expertise and skill in mould designing and fabrication and control of injection moulding machine parameters will lead to low quality plastic products. Designing of a mould is very important task involving significant decisions with implications to productivity and yield quality. In this research paper, the failure analysis of a mould of vertical plastic injection moulding machines utilized locally in Pakistan for production of plastic cups was investigated. After structural and thermal analysis of aluminum alloy Al6061 mould in analysis system (ANSYS), it was found that a designed mould for polypropylene cup will not face any failure.

Keywords: Injection Moulding Process, Mould, Modelling, Analysis, CREO Parametric, ANSYS.

1. INTRODUCTION

Moulds have been costly to fabricate and they are used where hundreds of products are being produced[1]. Typical moulds are made from aluminum, beryllium-copper alloy, hardened steel and pre-hardened steel[2]. Generally aluminum moulds are expensive to construct, but when the lifespan of aluminum mould is compare to its cost it becomes beneficial to use[3]. Tool design is driven by the complexity of part design[4]. Optimizing both tool design and part design can increase the quality of part and lifespan of the tool[5]. Till now different materials has been used for different moulds by researchers. They modeled and analyzed moulds using different techniques. Mohd Jamshed et.al.., has worked on the manufacturing of cam bush with submarine gate. He designed and fabricated the mould of cam bush for injection moulding process. To analyze the mould flow for cooling system of cam

bush, filling rate and submarine gate location he used auto desk mould flow[6].
a mould for plastic injection moulding and also performed the thermal analysis. Unigraphics version 13.0 software was used to design a mould and for thermal residual stress analysis software known as LUCAS Analyst version 13.0 was used[7].
K.K.Alaneme has worked on the punching machine mould which was used for the manufacturing of cable trays. He used different techniques for failure investigation which includes chemical composition determination, hardness tests, micro structural analysis and visual examination[8]. S.H. Tang et.al.., has worked on mould for plastic injection to reduce the warpage in the design. He used Taguchi method. After his research he came to a conclusion that warpage is mostly affected by melting temperature and slightly affected by filling time[9].
Silvia Barella et.al.., has worked on the copper mould to identify the failure and damages. Chromium was used to layer the sides of the mould. After his research they reached to a point that the working condition plays a major role to start a failure and high zinc content is responsible for copper wear[10].
D.M.Yakovleva et.al.., during his research they applied pressure to identify failure analysis of mould. They observed chemical and physical activity of casting alloy as major factors. Material properties and cyclic temperature power loading
S.H.Tang et.al.., has worked on warpage testing specimen in his research, he present intensity were also identified as major sources of failure. Contact surfaces were exposed to maximum level of stresses during filling[11].
Xi-Ping et.al.., has worked on the mould for LCD TV panel. During his research he tried to work on thermal analysis and stress analysis of the mould and the same time electric heating was also provided. He also identified the reason for large thermal stress using finite element analysis[12].
Different researches were carried out on different material moulds and considering different parameters [13, 14]. In this research project a mould was designed for vertical injection moulding machine and failure analysis related to structural and thermal analysis was performed as this mold will be used in injection molding machine for the manufacturing of polymers.

1. METHODOLOGY

Overall methodology of a research project is given below. However this research paper is only concentrated on modeling and analysis of a mould for vertical injection moulding machine. Keeping in mind the specification of vertical plastic injection moulding machine, first model of a mould is developed in CREO parametric and then same mould is analyzed in ANSYS.

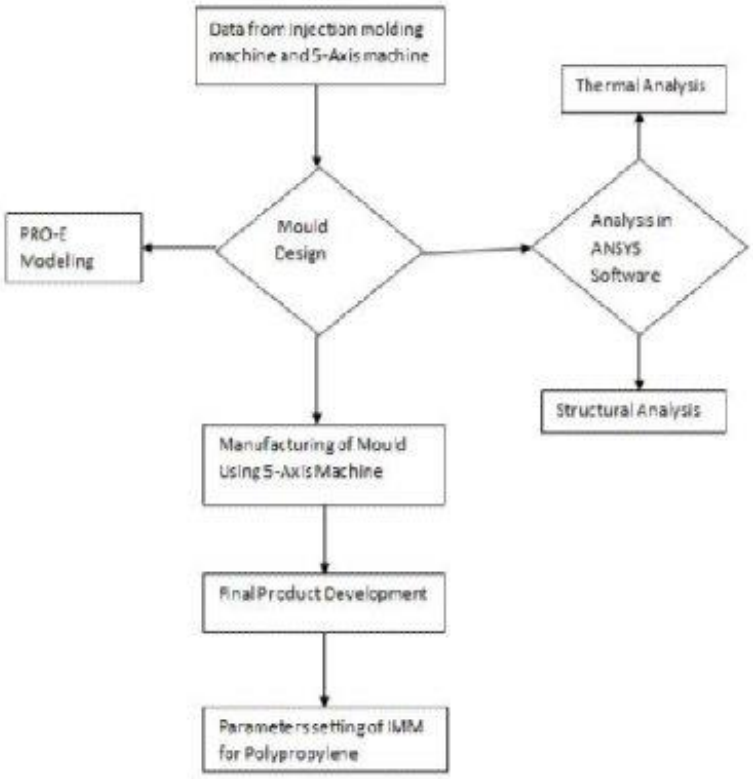

Figure 1. Flow Chart of Complete Research Project

1.1 Mould Modeling in PTC Creo

For the analysis or designing of a mould in ANSYS software, first we did modeling in PTC CREO. In order to make an assembly of a mould we need to first make the mould and drag part separately. When the model was completed drawing for cope and drag was generated. To see visually the whole model and develop understanding exploded drawing of an assembly was also made. Figure 2 show the cope and drag part separately while figure 3 shows the final model of a mould.

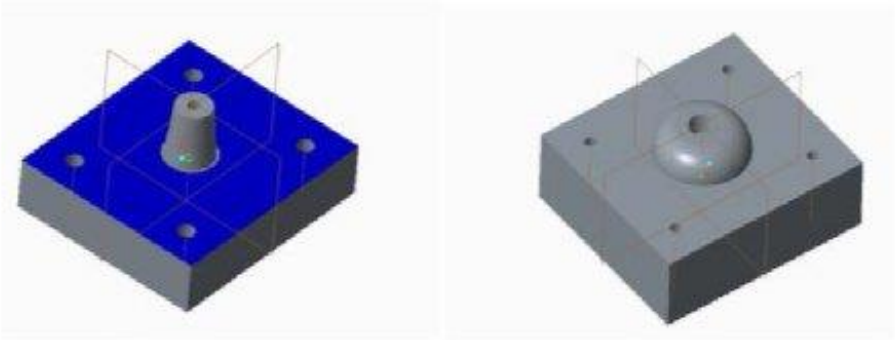

A. Cope B. Drag

Figure 2. Cope and Drag

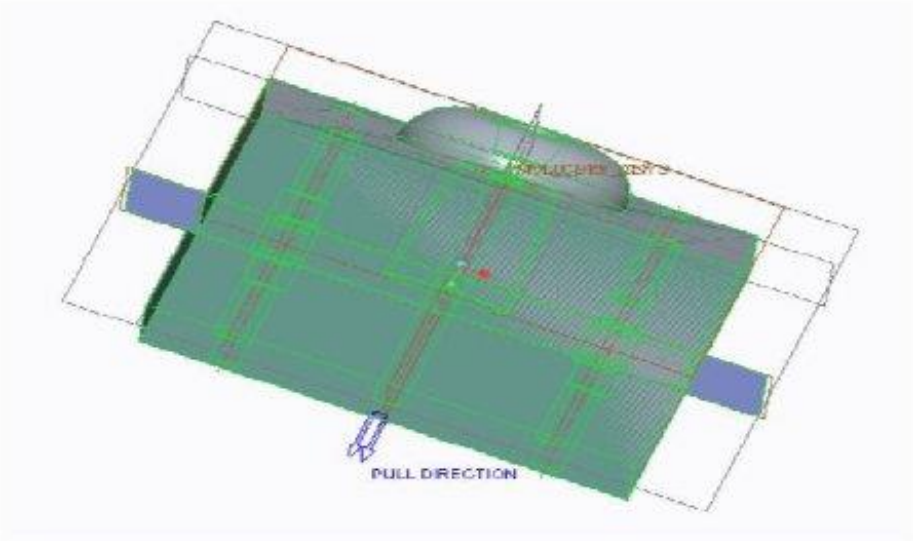

Figure 3. Final Model of a Mould

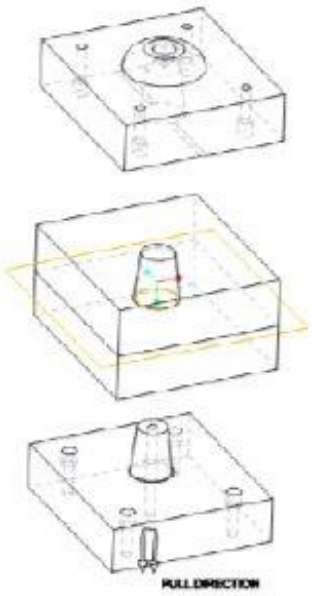

Figure 4. Mould Exploded Drawing

Mould will be rectangular in form. Length of a die is 239.52 mm (9.4 in) and its breadth is 212 mm (8.34 in). Generated drawing of a cope and drag is given below.

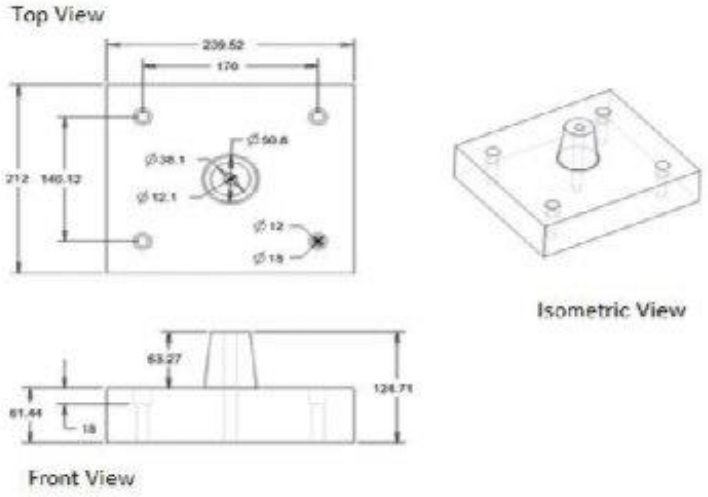

Figure 5. Drawing of a Cope

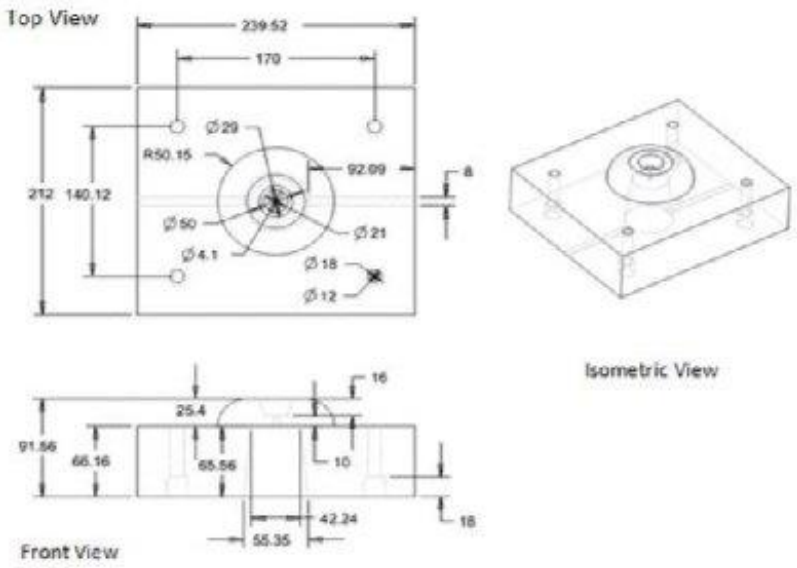

Figure 6. Drawing of a Drag

1.2 Structural and Thermal Analysis in ANSYS

In analysis we are more interested in structural and thermal analysis in order to know the chances of failure of a mould when both the temperature and pressure is applied on the mould at a same time[15].

Structural Analysis

ANSYS was used for structural analysis of a mould. The reason for finding the structural analysis was to identify the effects of load or the effects of pressure on the structure of mould. It helps in taking better and quick decision regarding the design of a mould.

As this mould is made for polypropylene cup and maximum pressure that we apply for polypropylene in vertical plastic injection moulding machine is 55bar. When the mould is kept under pressure of 55bar the below mentioned stresses were observed.

1. Normal Stress
2. Maximum Shear Stress

After performing structural analysis we got the value $7.9666e^{8}$Pa for maximum normal stress and $-1.501e^{8}$Pa for the minimum normal stress.

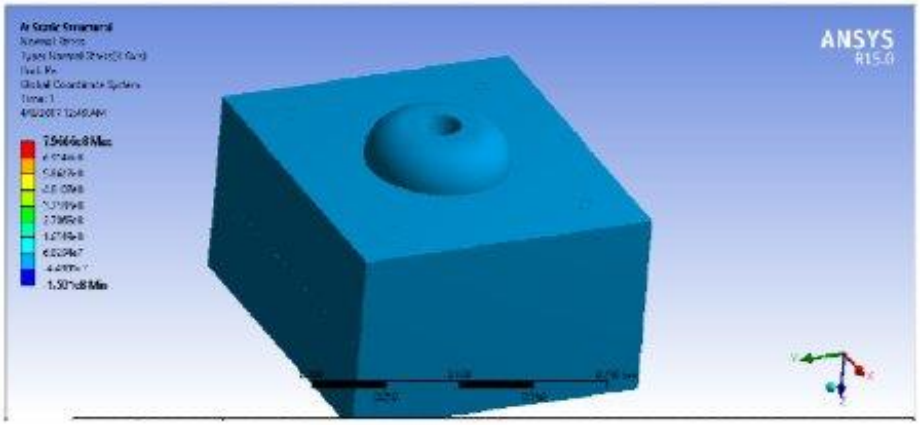

Figure 7. Normal Stress at 55bar Pressure

For shear stress we got the value $5.819e^{8}$Pa for maximum shear stress and 111.07Pa for minimum stress.

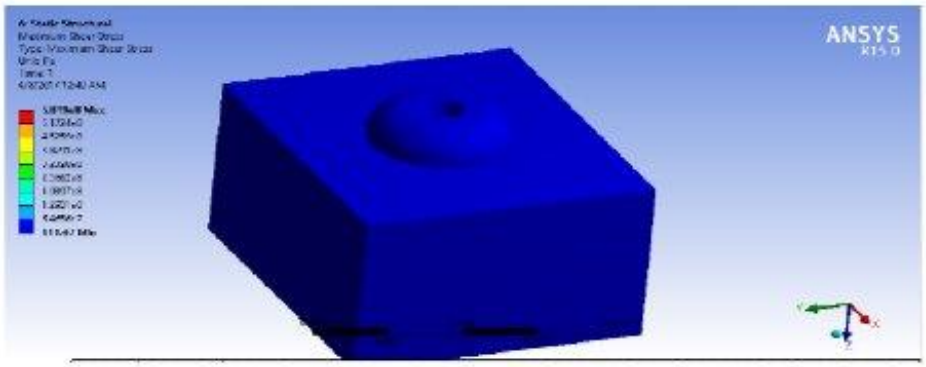

Figure 8. Shear Stress at 55bar Pressure

Thermal Analysis

ANSYS was also used to find the thermal analysis of a mould. Thermal analysis is actually performed to identify the changes in properties and structure of the material with change in temperature. To make an efficient design it has to be analyzed thermally in order to study the design more deep. Although different modes of heat transfer like conduction, convection, radiation also plays an important role to study thermal analysis but to study the effects of friction and power losses on thermal energy one need to use some special tools like ANSYS to identify the small changes as a reaction to heat change. Maximum temperature that we apply for polypropylene in vertical plastic injection moulding machine is 210°C. After the application of 210°C, we got the value 0.002256 for maximum thermal strain and $-6.0086e^{-16}$ for minimum thermal strain.

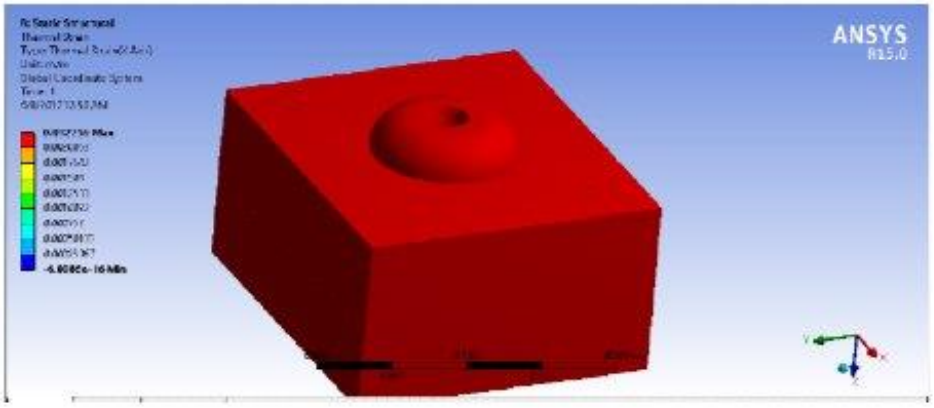

Figure 9. Thermal Strain at 210°C Temperature

This experiment is only performed to analyze the structural and thermal behavior of mould for 55bar maximum pressure and 210°C maximum temperature.

3. RESULTS

We got two results from our analysis one for structural analysis and the other for thermal analysis. The pressure applied on aluminum mould was maximum 55bar and minimum 45bar which is equal to 5.5MPa and 4.5MPa respectively. The applied pressure is very less than 240MPa (2400bar) which is the yield strength of aluminum alloy Al6061. It means that this pressure has no impact on the structure of mould and is good to use as mould of vertical injection moulding machine.

The melting temperature range for aluminum alloy Al6061 is 582°C to 652°C (1080 - 1205°F). The temperature applied for thermal analysis of mould was 210°C which is very less than melting temperature of aluminum alloy and thermal resistivity of aluminum alloy is high as compare to the one we got after applying 210°C temperature. It means that the aluminum alloy mould can be used for injection moulding without any problem of melting or deforming with temperature.

4. CONCLUSIONS AND FUTURE RECOMMENDATIONS

This research work was carried out to model and analyze aluminum alloy Al6061 mould for vertical plastic injection moulding machine. After modeling it in CREO parametric and then analyzing it structurally and thermally in ANSYS we concluded that this mould will not face failure and production could be done on it smoothly.

The same modeled and analyzed mould can be fabricated and used for production purposes in industry especially in injection moulding processes for the manufacturing of polypropylene cups and parameters of vertical plastic injection moulding machine can be optimized for plastic material like polypropylene using same mould as well.

5. REFERENCES

1. *Bledzki, A.K., A. Jaszkiewicz, and D. Scherzer, Mechanical properties of PLA composites with man-made cellulose and abaca fibres. Composites Part A: Applied Science and Manufacturing, 2009.* ***40****(4): p. 404-412.*
2. *Matarrese, P., et al., Estimating energy consumption of injection moulding for environmental-driven mould design. Journal of Cleaner*

Production, 2017. ***168****: p. 1505-1512.*

3. *Lucchetta, G., D. Masato, and M. Sorgato, Optimization of mold thermal control for minimum energy consumption in injection molding of polypropylene parts. Journal of Cleaner Production, 2018.* ***182****: p. 217-226.*
4. *Holthusen, A.-K., et al., Mold machining and injection molding of diffractive microstructures. Journal of Manufacturing Processes, 2017.* ***26****: p. 290-294.*
5. *Barrière, T., J.C. Gelin, and B. Liu, Improving mould design and injection parameters in metal injection moulding by accurate 3D finite element simulation. Journal of Materials Processing Technology, 2002.* ***125-126****: p. 518-524.*
6. *Jamsheed, M., et al., Design and Analysis of Plastic Injection Mould for CAM BUSH with Submarine Gate. Materials Today: Proceedings, 2015.* ***2****(4): p. 2083-2093.*
7. *Tang, S.H., et al., Design and thermal analysis of plastic injection mould. Journal of Materials Processing Technology, 2006.* ***171****(2): p. 259-267.*
8. *Alaneme, K.K., B.O. Adewuyi, and F.A. Ofoegbu, Failure analysis of mould dies of an industrial punching machine. Engineering Failure Analysis, 2009.* ***16****(7): p. 2043-2046.*
9. *Tang, S.H., et al., The use of Taguchi method in the design of plastic injection mould for reducing warpage. Journal of Materials Processing Technology, 2007.* ***182****(1): p. 418-426.*
10. *Barella, S., et al., Investigation of failure and damages on a continuous casting copper mould. Engineering Failure Analysis, 2014.* ***36****: p. 432-438.*
11. *Yakovleva, D.M., G.F. Mukhametzyanova, and L.R. Kharisov, The Research of Stresses in the Molds of Injection Molding Machines. Procedia Engineering, 2016.* ***150****: p. 453-457.*
12. *Li, X.-P., et al., Thermal and stress analysis of rapid electric heating injection mold for a large LCD TV panel. Applied Thermal Engineering, 2011.* ***31****(17): p. 3989-3995.*
13. *Moayyedian, M., K. Abhary, and R. Marian, New Design Feature of Mold in Injection Molding For Scrap Reduction. Procedia Manufacturing, 2015.* ***2****: p. 241-245.*
14. *Grandguillaume, L., et al., Mold Manufacturing Optimization: A Global Approach of Milling and Polishing Processes. Procedia CIRP, 2015.* ***31****: p. 13-18.*
15. *Ozcelik, B. and I. Sonat, Warpage and structural analysis of thin shell plastic in the plastic injection molding. Materials & Design, 2009.* ***30****(2): p. 367-375.*

TIDAL ENERGY POTENTIAL IN COASTAL REGIONS OF PAKISTAN

Absar Ahmed Khan[1*], Sohail Hasnain[2], and Muhammad Ali Syed[3]
[1]Office of Research, Innovation and Commercialization (ORIC), SZABIST, Karachi, Pakistan
[2]Mechanical Engineering Department, NED University of Engineering & Technology, Karachi, Pakistan
[3]Mechanical Engineering Department, Nazeer Hussain University, Karachi, Pakistan

[*]Corresponding author. Tel.: +92-331-256-7884
E-mail address: Absar.Ahmed.Khan@hotmail.com (Absar Ahmed Khan)

ABSTRACT

Energy shortage is a fundamental problem in Pakistan. This dearth has led to various problems in the country and overcoming this problem has become imminent. While the government has explored a number of sources for harnessing renewable energy, harnessing energy from tides still requires significant attention of not only the government but also of environmentalist and investors.

This paper provides an insight into the prospects of tidal energy in Pakistan across five different coastal regions, viz. Karachi, Hajmoro, Mianmi Hor, Pasni and Gwadar. The paper explores the power generation through high tides of the aforementioned coastal areas. The major idea is to utilize the tides of Pakistani coastal areas and harness the energy from them.

Through the performance analysis of a turbine model and employing necessary design calculations, the results have shown that Pakistan has a huge potential of harnessing the tidal energy from the Arabian sea covering its coastal areas.

Keywords: Tidal Energy; Karachi; Hajmoro; Mianmi Hor, Pasni, Gwadar, Renewable Energy

1 INTRODUCTION

Tidal power, or tidal energy, is a kind of hydropower. The potential energy present in the tides is harnessed and converted to potential energy through the turbine [1]. The world witnessed its first tidal power station in 1966 when France opened the Rance Tidal Power Station that now has the capacity to produce the electricity of 240 MW through its 24 installed turbines [2].

When compared to the wind or solar energy, tides are more predictable. However, harnessing energy from tides is still believed to be costly [3]. Besides, there is also a limited availability of sites having adequate high tides or flow velocities required for harnessing the potential energy, thus constricting its total availability. However, with the advancement of technology in terms of turbine technology such as the introduction of cross flow and axial turbines, and the adoption of new design techniques such as tidal lagoons and dynamic tidal power, it is now believed that the total availability of the tidal power could be greater than it was previously anticipated [4]. This has also led to the idea that the environmental and economic cost could be slashed, making them highly competitive in its deployment.

2 GENERATION OF TIDAL ENERGY

As the other sources of harnessing renewable energy primarily depend on the sun, wind and fossil fuel, tidal power is the only kind of renewable energy that is harnessed due to the relative motion of Earth-Moon system, and to some extent from the Earth-Sun system. When combined with the rotation of the earth, the moon and sun effect on the tidal forces, thus causing the generation of tides.

Tidal energy is harnessed when the large bodies of water are in motion. The water levels of the sea periodically change while the tidal currents that are associated with the sea depend on the gravitational attraction of the moon and sun. The magnitude of the tide in a given location is the product of the constant changing of the positions of the moon and sun in relation to the rotation of the earth. The tidal

magnitude also depends on the coastal lines and sea floor [4].

Since the tides are the product of gravitational interaction with the moon, sun and the earth's orbital, therefore the tidal energy is termed as practically inexhaustible and thus classified as a renewable energy resource.

A tidal generator is employed to harness the potential energy in the tides and convert that energy into kinetic energy for power generation. The high variation in tides and the tidal current velocities ultimately increase the potential of electricity generation.

The phenomenon of tidal movement leads to a continual loss of mechanical energy in the earth-moon system as the water is pumped through the natural restrictions around the coastal lines, causing viscous dissipation at the seabed and in turbulence. The loss of energy has led to the slowing of earth's rotation since its formation around 4.543 billion years ago. However, in the last 620 million years, the earth's rotation period has surged from 21.9 hours to 24 hours today. This phenomenon has caused the earth to lose 17% of its rotational energy in the last 620 million years [5]. The tidal power, thus, can be concluded to be taking energy from the system, causing the rate of slowdown to increase; however, this effect is noticeable only after millions of years and, therefore, is said to be negligible.

2.1 Tidal Stream Generator

Tidal stream generator strategy is use to harness kinetic energy from running tides of water. It works on same line as wind energy. Tidal stream generators are usually cheap, environment friendly and most prevalent in the harnessing of tidal energy.

Several types of tidal stream generators are employed today. The most common type is Axial or Horizontal Turbine. These types of turbines have a rotor that is parallel to the flow of the water. The rotors employed are similar to those used in wind turbines, however the properties of the hydrofoil (just like airfoil for turbines and aeroplanes) are different since they operated in the fluid that is water [6].

Axial turbines are friendly to marine life and produce less noise. Since the density of the water is greater than the air, therefore the power output of axial turbine installed in a given area is higher than wind turbine. This means that an axial turbine with higher rotor swept area than wind turbine will harness more energy. The power output may be enhanced further through the use of Venturi effect that allows water to move with additional velocity through the blades of the turbine.

The axial turbines use the lift created by the water to harness the energy. The hydrofoils are designed to create a certain pressure difference that is different from airfoil. The orientation of the rotor, commonly referred to as rotor pitch, has to be carefully adjusted to allow the potential energy present in the tide to be harnessed as the tide is changed. The primary drawback of tidal turbines is that they tend to get affected by corrosion due to the sea water and, thus, require high maintenance cost.

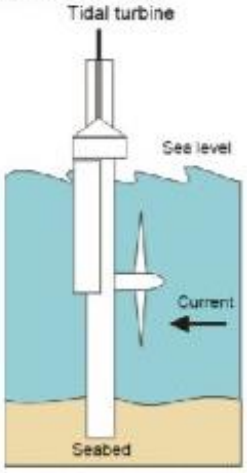

Figure 1. Tidal Stream Generator

3 POWER GENERATION

Different turbine tend to operate under different efficiencies which affects the power output. In the event that the efficiency of the turbine "η" is known the condition underneath can be utilized to decide the power output of a turbine. The energy harnessed from these turbines can be mathematically represented as [4]:

$$P = \frac{\eta \rho A V^3}{2} \quad (1)$$

where,

η = Efficiency of turbine

ρ = Density of water (sea water) 1030 kg/m^3

A = the sweep area of turbine in m^3 = πR^2

V = the velocity of water flow

The potential energy present in the seawater is given by:

$$E = g\rho A \int z dz = \frac{1}{2} g \rho A h^2 \quad (2)$$

where,

E = Potential energy

g = Acceleration due to the gravity (9.81 m/s^2)
ρ = Density of seawater (1030 kg/m^3)
A = Sea area under consideration
z = Vertical coordinate of ocean surface
h = Tide amplitude

The estimation of the potential energy available in the tidal stream device is contingent upon an the tidal-current velocity. This velocity in the tidal-current follows significant variation in different regions and this is because of the astronomical influence.

When the tidal flow enters the duct attached with the turbine, it converges after striking the blade and then exists the turbine, diverging while exiting completely. In this scenario, the inlet and outlet areas are considered at A_{in} and A_{out}. It can be said that the power that is extracted in this process is the product of energy extracted due to the tidal flow and the volumetric flowrate (Ṿ) (m^3/s). When the power is extracted from the flow, this is due to the loss in total pressure as stated in the Bernoulli equation (3) below,

$$Power = (P_2 - P_1)\dot{V} \quad (3)$$

When the Bernoulli is applied to the above equation (3), it yields equation (4),

$$P_1 = P_2 = P_{SP} + \frac{1}{2}\rho(v_\alpha)^2 \quad (4)$$

where,

P_{SP} = freestream static pressure
v_α = freestream flow velocity

The power of the turbine is contingent upon the volumetric flowrate and may commonly be referred to as discharge through the device 'Q', upon the freestream velocity (v_α)(m/s) and the exit area (A_{out}) (m^2).

The maximum power output is given by the equation (5),

$$Q_{maximum\ power} = \frac{1}{\sqrt{3}} v_\alpha A \quad (5)$$

4 CALCULATION

There are two high tides and two low tides every day. The average for every month is being calculated and presented in the following Table 1 [7].

Table 1: Tidal Amplitude of Karachi, Hajmoro, Mianmi Hor, Pasni and Gwadar

	Karachi	Hajmoro	Mianmi Hor	Pasni	Gwadar
	Tidal Amplitude (h) in meters (m)				
May-17	1.673	1.878	1.624	1.873	1.57
Jun-17	1.642	1.868	1.618	1.867	1.56
Jul-17	7.036	1.858	1.609	1.858	1.56
Aug-17	1.659	1.857	1.598	1.863	1.572
Sep-17	1.624	1.824	1.567	1.823	1.57
Oct-17	1.623	1.809	1.56	1.809	1.5
Nov-17	1.606	1.807	1.557	1.815	1.51
Dec-17	1.618	1.816	2.19	1.815	1.7
Jan-18	1.638	0.952	1.582	1.84	1.5903
Feb-18	1.642	1.848	1.598	1.848	1.5125
Mar-18	1.657	1.841	1.615	1.86	1.56
Apr-18	1.664	1.835	1.624	1.864	1.57
May-18	1.672	1.882	1.622	1.88	1.57

Table 2 presents the results using the equation (2).

Table 2: Potential Energy Present in the Tides

	Karachi	Hajmoro	Mianmi Hor	Pasni	Gwadar
	MW				
May-17	0.21	0.27	0.20	0.26	0.19
Jun-17	0.20	0.26	0.20	0.26	0.18
Jul-17	3.74	0.26	0.20	0.26	0.18
Aug-17	0.21	0.26	0.19	0.26	0.19
Sep-17	0.20	0.25	0.19	0.25	0.19
Oct-17	0.20	0.25	0.18	0.25	0.17
Nov-17	0.19	0.25	0.18	0.25	0.17
Dec-17	0.20	0.25	0.36	0.25	0.22
Jan-18	0.20	0.07	0.19	0.26	0.19
Feb-18	0.20	0.26	0.19	0.26	0.17
Mar-18	0.21	0.26	0.20	0.26	0.18
Apr-18	0.21	0.25	0.20	0.26	0.19
May-18	0.21	0.27	0.20	0.27	0.19

Applying equation (1) and using the turbine efficiency as defined by Betz Limit that is 59.3%, the following power output results are being obtained, presented in the Table 3.

Table 3: Turbine Efficiency and Power Calculation

Density (kg/m^3)	Efficiency (%)	π	R^2 (m^2)	V^3 (m/s)	Total (Watts)
1330	0.59	3.14	100	27	2501.1

The following Figure 2 gives a graphical illustration of the results obtained in the Table 1.

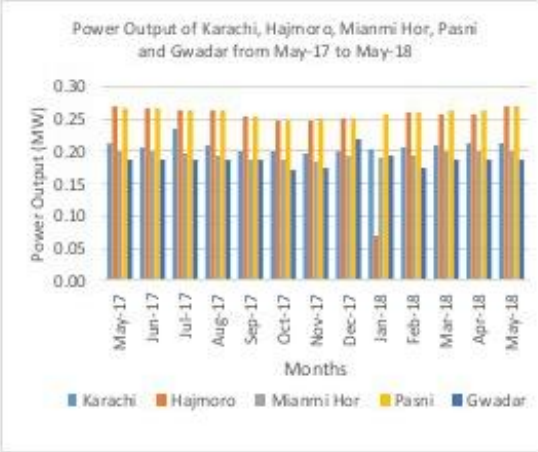

Figure 2. Tidal Power Output of Karachi, Hajmoro, Mianmi Hor, Pasni and Gwadar

5 DISCUSSION

The tidal amplitude of the five coastal regions in Pakistan suggest that there is not much variation in the five identified regions. Pasni and Hajmoro regions from the Table 1 show relatively good tidal amplitude. This corresponds with the results shown in the Table 2 where Pasni and Hajmoro have a better power output.

When the turbine efficiency is being calculated, the results have shown that a single turbine with blade radius of 10 meters would yield an output of 2.5 kW as presented in Table 3. If the radius of the turbine blades is increased, this would result in the increased sweep area and the turbine would be able to harness more energy.

The results also suggest that much of the power output depends on the type of turbine used and the efficiency that it may carry.

6 CONCLUSION

Pakistan is blessed with the renewable energy resources. One such resource is its Arabian sea that can be used to harness tidal energy. There are various dynamic factors that make the renewable energy market more attractive and this is due to the advancement of technology. Tidal energy, therefore, is also an appealing part of the renewable market and the advancement in the technology has allowed the countries to invest in the tidal energy. In the upcoming decades, tidal energy may just become the largest source of energy harnessing not just in Pakistan but across the world. Various studies have suggested tidal energy to be a viable option. However, the downside of this renewable energy resource may well be the limited supply based on the tidal cycles. Another aspect is that, increased cost has played a crucial role in the promotion of tidal energy. However, when this cost is compared with the cost of generating electricity through fossil fuel, tidal energy turns out to be a lucrative option. Harnessing the tidal energy in Pakistan will also allow the fossil-fuel dependent country to reduce the emission of greenhouse gases.

ACKNOWLEDGEMENTS

Thanks to The University of Nottingham, UK for allowing me to get access university's digital database.

REFERENCES

[1] R. H. H. Charlier, *Ocean Energy: Tide and Tidal Power*, Springer, 2010.

[2] J. Twidell, *Renewable Energy Resources*, Routledge, 2005.

[3] C. Khare, S. Nema, P. Baredar, *Tidal Energy Systems: Design, Optimization and Control*, Elsevier, 2018.

[4] J. Hardisty, *The Analysis of Tidal Stream Power*, John Wiley & Sons, 2009.

[5] N. Rehman, Tidal energy resource characterization in Chacao Channel, Chile, *International Journal of Marine Energy*, 20, 1-16, 2017.

[6] A.J.G. Brown, S.P. Neill, M.J. Lewis, Tidal energy extraction in three-dimensional ocean models, *Renewable Energy*, 114(A), 244-257, 2017.

[7] Tide Station Location Guide. (2019). Retrieved from https://www.tide-forecast.com/locations/

DESIGN AND FABRICATION OF COST EFFECTIVE SOLAR WATER HEATER FOR SINGLE HOUSE UTILITY

S. Sheraz Ali[1*], Ateeque Ahmed[2], Bilal Ahmed[2], Shahzaib Abbasi[3], Sumiya Mohsin[2]

[1]Mechanical Engineering Department, Pakistan Navy Engineering College, NUST, Karachi, Pakistan

[2]Mechanical Engineering Department, NED University of Engineering & Technology, Karachi, Pakistan

[3]Department of Power Engineering, Karachi Institute of Power Engineering (KINPOE), Karachi, Pakistan

[*]Corresponding author. Tel.: +92-302-6225332

E-mail address: atteqashfaq@gmail.com

ABSTRACT

The project aims to design and fabricate a solar water heater for single house use. Our first phase comprises of design research. There are lots of designs currently applicable in the world. But we opted for our new design that is Glazed Triangular Solar Collector (GTSC). The major desire of this project is to reduce the cost. The design explains the benefit of triangular glazed solar collector over rest of solar collectors. Its effectiveness arises due to wider use of greenhouse effect; hence it beats up flat plate collectors convincingly. The material selected here is Ethylene Propylene Diene Monomer (EPDM). Being black in color, almost the same thermal properties with copper, it produces a good result. On the other hand, Thermo Plastic Natural Rubber (TPNR) with Stainless Steel (SS) are subject to availability. By the end of the first phase, a need was felt to compare the innovative EPDM solar tubes with the more established copper tubes, therefore the performance of the two can be practically evaluated. Hence in the second phase two solar water heaters one comprising of copper tubes and other consisting of EPDM designed and fabricated. To match our theoretical result with experimental results, we did fabrication of two solar geysers: Copper and EPDM. The aim of the project was to build a cost-effective solar geyser, after analyzing all results, it has been observed that fabrication from the EPDM (rubber) tube effective solar geyser was more effective in terms of cost analysis. In terms of solar geyser performance, from the copper-based geyser, concluding that Copper is acting as a best solar absorber, giving the output of hot water. While EPDM takes time, but, it has to be noted that during the experiment it is verified that if we use EPDM for three consecutive days, it is thermal conductivity increases. It means the more we use EPDM tube the more it will be acting as a good solar absorber. It is concluded that the copper having three times more cost as compare to EPDM. Therefore, it is recommended to use EPDM tubes SWH to reduce the cost of single house utility.

Keywords: Solar Water Heater; Glazed Triangular Solar Collector; EPDM Tubes; Cost Effectiveness

1 INTRODUCTION

The importance of renewable energy is accepted worldwide and policies are executed around the world to promote its use to fulfill the needs of mankind. The dominant sources of renewable energies of today's world are Hydro, Wind, Solar, Ocean energy and Biomass conversion. The sun is the primary source of heat and light and responsible for life on Earth. Understanding the Sun's relationship with Earth is critical for site planning, efficient building design, and controlling unwanted heat gains. The Sun is a giant star and the largest object in our solar system. The energy of the sun is a result of nuclear fusion that occurs at temperatures ranging from 18 to 25 million degrees F [2]. Solar energy solution is a cheap solution for economic crises like in our country. It is the best alternative to produce electricity and do a lot of domestic work. In short, our dependency on conventional energy modes reduces by using substitute renewable energy modes. Solar radiations reaching the earth surface are enormous and sufficient amount of energy that can be utilized cost-effectively and efficiently for water heating. There are numerous solar water heating systems used around the world for domestic water heating.

Solar radiations reaching the earth surface are enormous and sufficient amount of energy that can be utilized cost-effectively and efficiently for water heating. There are numerous solar water heating systems used around the world for domestic water heating. Vacuum tube solar collector is one of the most efficient systems it has high installation cost. A product can never become common until and unless it is in purchasing power of common man. Subsequently, it is necessary to produce cost-effective solar heater for single household use in Pakistan. We can save a lot of electricity and gas by shifting our domestic water heating systems from conventional heating methods to solar water heating. Therefore, it is necessary to produce cost effective solar heater for single household use in Pakistan. We can save a lot of electricity and gas by shifting our domestic water heating systems from conventional heating methods to Solar water heating. In 1767, Swiss scientist Horace de Saussure build the world first ever solar collector. He observed heated water when placed sunrays passed through the black insulated box as shown in Figure 1.1 [1]. In 1891, An American, Clarence Kemp found hot water when black painted water tank placed inside an insulated box. The first time made the SWH as a commercial product is shown in Figure 1.2 [3].

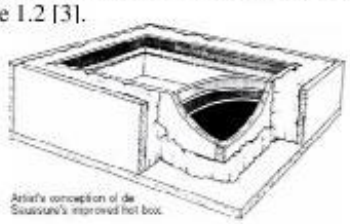

Figure 1. The Concept of Solar Collector

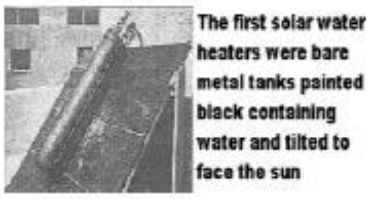

Figure 2. Early Solar Heater

2 GLAZED THERMOSYPHON SOLAR COLLECTOR

The design choice is done on the basis of cost effectiveness, commercial value and the value of the economic result. The word of solar energy has not yet reached the common man in the country. Therefore, we are trying to make it accessible for a simple man, with the allowable cost to spend. We have designed and fabricated a double slope triangular greenhouse chamber with black body effects. The material used is cheaper than a conventional one and reliable. It is available in the market, so one can easily manufacture it without importing any part. One of major use of GTSC is that it is following greenhouse rule. It is environment friendly. The idea of EPDM based triangular solar collector is aforementioned [4]. The material used is EPDM (Ethylene-Propylene-Dimer M-Class rubber) which is made up of TPNR (Thermoplastic Natural Rubber). The working of GTSC is following the fundamentals of glazed flat plate collector. The science involved in doing this is to ensure minimum heat (convective) loss and to ensure the development of vacuum inside the chamber. As radiations pass through the reflected glass. It strikes the collector which raises the temperature of the body and water inside the tube. This then follows the thermosiphon effect, raising the hot water over the storage tank and substitute the cold water to heat. This circulation continues until a uniform temperature is reached across the storage tank. The triangular design ensures the maximum sunshine over the solar absorber and hence maximum output. The 3D design of GTSC, which is shown in Figure 2.

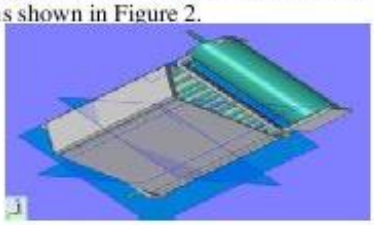

Figure 3. Glazed Triangular Solar Collector

This concept uses an idea of minimal heat loss, by using glazed or double glazed glasses. After making use of all insulating material and placing the collector inside the insulating box, to avoid any heat loss. The glazed glass is put over the box, containing collector/ absorber. It is done so that vacuum is created inside the box. The vacuum doesn't allow further disturbance or traveling of air. As the incident rays fall over the glass, some of the rays reflected and some pass through the glass. It is most important to keep the collector on an optimum angle. As black color is an ideal absorber. Hence the selective coating with black color is done on the collector box as well as the storage tank.

3 DESIGN CALCULATION

The calculation analyze includes some constraints in order to meet some objectives. Here is enlisted the summary of constraints:

Area of solar collector
$A = 1\ m^2$

The volume of the storage tank
$V = 0.015\ m^3$

The range of Diameter of tube
Starting Range – 7 mm
Final Range – 15 mm

3.1 Calculation for Solar Radiation

Solar flux for horizontal and tilted surface

The total radiations falling daily over a place vary place to place. Monthly average daily total radiations (on a horizontal surface) for Karachi are described in Table 3.1. [5]. It is to be noted that less radiation observed in the month of December from cited data. Our analysis focus would be on the month of December.

Table 1. Solar flux on a horizontal and tilted surface

S. No	Month	Solar Radiation Horizontal (W/m^2)	Solar Radiation at 45° tilt (W/m^2)
1	January	183.09	248.4681
2	February	207.88	282.0796
3	March	208.37	282.7581
4	April	254.39	345.2344
5	May	266.52	361.6676
6	June	266.52	361.6676
7	July	266.52	361.6676
8	August	221.62	300.7383
9	September	193.83	263.0409
10	October	213.21	289.3355
11	November	189	256.4784
12	December	164.69	223.5658
	Average	219	298

3.2 Calculation of Tube Length

While we have to do a repetitive iteration to find the optimize diameter that gives optimize tube length. For heat transfer, we have the formula:

- Heat storage equation

$$T_e = T_i \frac{q_s \times A_s}{m.C_p} \quad (1)$$

- Equation change in terms of diameter and half exposed solar collector area

$$L = \frac{(T_e - T_i)m.C_p}{\pi \times d \times q} \quad (2)$$

where, L = length of tube, q_s = heat flux, m = mass flow rate, C_p = specific heat, T_e-T_i = Temperature difference, A_s = Area of tube and d is diameter of tube.

The result obtained, which is shown in Table 3.2.

Table 2. Calculation for Length of Tube

Parameters	Symbols	Values
Temperature Difference	$\Delta T = T_e - T_i$	50 °C
Mass flow rate	M	0.000595 kg/s
Specific heat capacity of water	C_p	4182 J/kg °C
Heat Flux	Q	219 W/m^2
Diameter of tube	D	10.8 mm
Length of tube	L	33 m

Hence for the diameter of 10.8 mm, the result for the total length of the tube comes to be L = 33 m (108 ft).

The relationship between the diameter of the tube and the length of the pipes

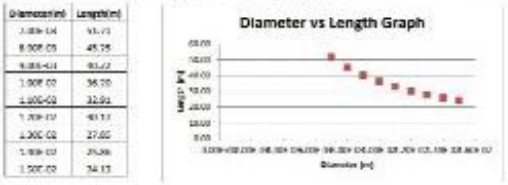

Figure 4. The relation between Diameter and Length of pipe

Correlation between mass flow rate and length of the pipes

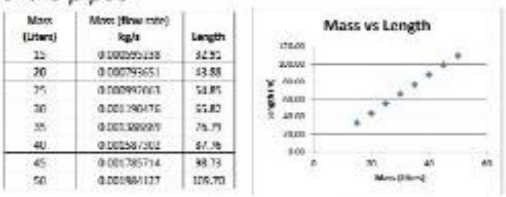

Figure 5. The relation between Mass flow rate and Length of pipe

3.3 Spacing between Tubes

In order to calculate the spacing between the tubes, we introduce a dimensionless parameter "G.X". For 100 % efficiency. As G.X =0.1
where, X = length of the tube

$$G = \left[q_s \times A_s / m.C_p\right]^{\frac{1}{2}} \quad (3)$$

where, Uc is the heat loss conductance and k is the thermal conductivity and t is tube thickness.
U_c for two glass covers is taken as 4 W/m^{2}K. The thickness of the plate 1.5 mm and the material of the tube is copper taken as (k = 386 W/mK). Therefore the value of g is G= 2.63.
Now center to center distance between the tubes is

$$L' = 2X + Dt \quad (4)$$

Spacing between tubes = L' = 0.087 m

3.3 Number of Tubes

The number of tubes is given by total length/spacing between tubes.

$$N = K/L' \quad (5)$$

where, K = total length and L' is spacing between tubes
Number of tubes = N = 30

4 MATERIAL SELECTION

4.1 For Metallic Sheet

Material selection of metallic sheet is purely based on the specific heat capacity of the metal. The less thickness means less mass and thus less heat capacity of the system. By the formula:

$$Q = H(T_f - T_i) \quad (6)$$

where, Q is heat attained by the system and H is heat Capacity of the system, while T_f and T_i are final and initial temperature of the system.

4.2 EPDM Tube Selection

After survey to different industries, EPDM tubes bought for PKR 21 /ft. It is the price for introducing EPDM rubber tubes in Pakistan when mass production will take place this price will go down further.

Figure 6. EPDM Tube

4.3 Copper Tube Selection

As the project is a sort of comparison between Copper and EPDM rubber. It is higher thermal conductivity makes it as a good solar absorbing material, it loses its radiation absorption due to deprivation in color. Due to abundance, it's available everywhere. Price of copper is PKR 70/feet.

Figure 7. Copper Tube

4.4 Manifold Material Selection

For manifold, two copper pipes of 1 in are taken into account. Its gauge is 20. The numbers of tubes, as evaluated are 33, so 33 riser tubes of about half inch (11mm) and calculated length (36 in – 3ft) are divided into a piece. They form an array of tubes or a grid. The headers are first drilled holes of the riser number of 33 from the drilling machine in the machine shop.

4.5 Characteristics of the black ended surface at the bottom and sides

These blackened surfaces are made by painting a 37 gauge. Aluminium sheet of 0.11 mm thickness. The thickness is less to decrease the heat capacity of the black body so that it can quickly achieve the required temperature and start emitting the infrared radiations. If a surface is coated black with increased quantity of carbon, its absorption capacity increased more than 92%.

5 TRANSPARENT INCLINED SURFACES TO FACE THE SUN

We are using glass with inclined surfaces in a triangular form. Therefore, by this arrangement solar radiations at morning and evening strike the glass surfaces at an angle less than the critical angle and most of the radiations are absorbed inside the chamber. Sunrises after 7:00 am in December. Therefore, the demand for hot water in winter increased in the morning. However, most of the radiations should pass through glass which is much possible in the triangular chamber. From the comparison, it is clear that there is not much difference in the critical angles. We can use any glass because the chance of exceeding critical angle is much lesser in our case of the triangular chamber. Silica glass is commonly available and the one with 97% transmittance and 5mm thickness was chosen as tabulated in Table 5.

Table 3. Glass Refractive Index at Critical Angles

Glass	Refractive Index	Critical Angle
Flint Glass	1.6	38.8°
Crown Glass	1.52	41.3°
Silica Glass	1.46	43.4°

Pyrex Glass	1.474	42.9°

6 HEAT TRANSFER CALCULATIONS

6.1 Chamber Analysis

The chamber faces the solar radiation its sides will be made out of blackened aluminium sheet which will absorb heat and emit infrared radiations. A blackened surface though not perfectly black proves to be a good absorber of radiations more than 90% and good emitter of heat in the form of low wavelength radiations. About 45.37 % of these radiations are absorbed by the tubes so as a result they are provided with additional heat flux. The basic information which has made our chamber analysis easy is that isotherms are formed after some time when steady state condition is reached.

6.2 Natural Convection for blackened Metal Sheet

As the solar radiations fall on the collector, the blackened sheets start to heat up. Consequently, it starts to heat up the enclosure air by natural convection and radiation. Natural convection takes place, the Grashof number is among the fundamental characteristics used to classify natural convection and to calculate Nusselt number for natural convection heat transfer and Grashof number (Gr) is

$$Gr = \frac{g\beta(T_s - T_\infty)L_c^{\,3}}{\upsilon^2} \quad (7)$$

where, g = gravitational acceleration, β = Coefficient of volume expansion, (β = 1/T for ideal gases), T_s = Temperature of the surface, T_a = Temperature of Air sufficiently far from the surface, L_c = Characteristic Length of geometry and υ = Kinematic viscosity of the fluid.

Now the Rayleigh number another dimensionless constant. It is calculated by:

$$Ra = Gr.\Pr \quad (8)$$

where, Ra is Rayleigh number, Gr is Grashof number and Pr is Prandlt number.

$$\Pr = \frac{\upsilon}{\alpha} \quad (9)$$

where, ν is kinematic viscosity and α is thermal diffusivity

Finally the Nusselt number determined by using the following formulas:

$$Nu = 0.15 * (Ra)^{\frac{1}{3}} \quad (10)$$

for 10^7 < Ra < 10^11

Now heat transfer coefficient calculated by [9]:

$$h = \frac{Nu \times k}{x} \quad (11)$$

where, k is Thermal conductivity of fluid and x = Characteristic Length of the glass slab.

Finally, the heat transfer to the chamber by heat source i.e. blackened metal sheets are calculated by:

$$q = hA(T_b - T_c) \quad (12)$$

where, T_b is Temperature of blackened surface, T_c is Temperature of enclosure air, h is natural convection heat transfer coefficient and A is the area of bottom plates not covered by tubes.

The output of Natural Convection for blackened Sheet

Table 4. The output of Natural Convection for blackened Sheet

Parameters	Symbols	Values
Grashof Number	Gr	1122510
Prandtl Number	Pr	7.020979
Rayleigh Number	Ra	7881118.9
Nusselt number	Nu	29.850656
Heat Transfer Coefficient	h	3462.6761

6.3 Natural Convection at Inner Surface of Glass Chamber

As the air of chamber starts to heat up, the inner surface of glass gets hot by convection and radiation, from where it is conducted through the glass thickness to outside and then lost to the environment. Now the heat transfer coefficient is determined by Nusselt number. Nusselt number is taken from the experimental results available for the natural convection in an isosceles triangle with discrete bottom heating. These calculations are done by available experimental values of Nusselt number plotted against Grashof number for different inclinations as shown in Figure 6.1. [6].

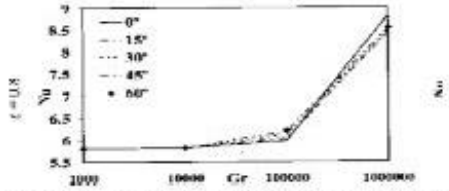

Figure 8. Experimental Values of Nusselt Number

Heat transfer to the chamber by heat source i.e. blackened metal sheets is calculated by [8]:

$$q = hA(T_a - T_{gi}) \quad (13)$$

where, T_{gi} is Temperature of the inner glass surface, T_a is Temperature of enclosure air near to inner glass surface, A is the area of blackened sheets and h is natural convection heat transfer coefficient can be evaluated from equation (6.5).

Nusselt number and Rayleigh number for horizontal tube [9]:

$$Ra = \frac{g\beta(T_s - T_a)D^3}{\nu^2}\Pr \qquad (14)$$

$$Ra \le 10^{12} \Rightarrow Nu = \left\{0.6 + \frac{0.387\sqrt{Ra_D}}{\left[1+\left(\frac{0.559}{\Pr}\right)^{\frac{9}{16}}\right]^{\frac{8}{27}}}\right\}^2 \qquad (15)$$

Output for Natural Convection at Inner Surface of Glass Chamber

Table 5. Output for Natural Convection at Inner Surface of Glass Chamber

Temperatures (°C)			Other Parameters			
Cham Temp	Surface Temp	Film Temp	Ra	Nu	H	A_s
20	80	50	35032.1	2.99	7.45	0.03
40	80	60	17439.4	2.57	6.59	0.03
60	80	70	6727.23	2.12	5.57	0.03

Table 6. Output for Natural Convection at Inner Surface of Glass Chamber

Cham Temp	Convective Heat Loss (W)	Radiation Heat Loss (W)			Total Heat Loss (W)
T	**Q_{conv}**	**Emissivity ε**			**Q**
		0.450	1.000	0.900	
20	15.432	7.189	15.976	14.37	29.810
40	9.099	5.226	11.612	10.45	19.550
60	3.847	2.847	6.328	5.695	9.542

Relation for Chamber Temperature and Total Heat Loss

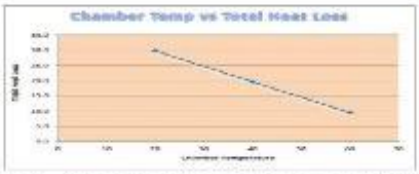

Figure 9. Chamber Temperature vs Total Heat Loss

6.4 Conduction by the Glass Slab

This is the heat lost to the environment as we are taking steady state case and assuming heat generation to be zero. The heat conducted by the glass slab can be found out by Fourier's law:

$$Q = kA\frac{\Delta T}{\Delta x} \qquad (16)$$

Table 7. Conduction by Glass

k glass	Thermal conductivity	1.4 W/mK
ΔT	Difference of temperature	50 °C
A	Area of a glass slab	0.404 m
X	Thickness of the glass slab	0.005 m
Q	**Heat conducted**	**56.56 kW**

6.5 Convection outside of inclined glass surface

Now the heat is conducted through the glass and then lost to the environment from outside of the inclined surface by convection. The wind speed was taken as 3 m/s. Reynolds number was then calculated by

$$\mathrm{Re} = \frac{v..x}{\nu} \qquad (17)$$

where, Re is Reynolds number, v is wind speed (m/s), x is a characteristic length of the glass slab and ϑ is kinematic viscosity of air.

As Grashof number (Gr) is discussed in equation (6.1) will be also used here. As the natural and forced convection both exist here. Therefore, the dominance is explained by the factor [9].

$$\frac{Gr}{Ra^2} \qquad (18)$$

If Gr/ Re^2<1 natural convection is dominant and is considered only. If Gr/Re^2=1 both natural and forced convection are to be taken in to account and if Gr/Re^2>1 forced convection is dominant and is considered only.

By calculation comes out to be less than one (Gr/Re2<<<<1). Therefore, only natural convection is dominant and forced convection effect by gusty wind is thus neglected in the calculations. Prandtl number is another dimensionless constant that is:

$$\Pr = \frac{\upsilon}{\alpha} \qquad (19)$$

where, ϑ is kinematic viscosity and α is thermal diffusivity

Now the Nusselt is calculated [7] by:

$$Nu = \frac{h..x}{k} = 0.0296\,\mathrm{Re}^{0.8}\,\Pr^{1/3} \qquad (20)$$

where, $0.6 < Pr < 60$, $5x10^5 < Re < 10^7$ and convection heat transfer coefficient (h) is determined using equation (6.5).

Finally, the heat loss to the environment is calculated by:

$$q = hA(T_{go} - T_{amb}) \quad (21)$$

where, T_{go} is outside glass surface temperature, T_{amb} is the temperature of environment h is natural convection heat transfer coefficient and A is the area of the glass sheet.

6.6 Conclusion of Chamber Calculations

Natural convection is dominant but the triangular chamber has this inherent property that the chamber air temperature near the glass surface has the temperature difference with the ambient of approximately 5% of base plate temperature and ambient temperature difference. According to Holtzman and GA Hill due to natural convection currents of air inside of a triangular enclosure the layer of air close to the bottom blackened surface has a temperature of 0.85 T_b and temperature of the layer of air close to the inclined surface is ($0.05T_b$ + T_{amb}). If the angle of inclination of glass is kept 45°. The analytical model results also confirmed to the experimental results obtained by the testing of the prototype. This astonishingly reduces the heat loss from the chamber that comes out to be 40 W against incoming of 208 W. Heat losses are only 19.2 % of incoming radiation. These heat losses also include losses by small reflectivity of the blackened body up to 5 – 10%. Solar insulation is taken to be 235 W/m^2 in the morning during winter. Although vacuum tubes have losses of 5 % the cost of a bunch of tubes is high as compared to the chamber.

6.7 STARTING TIME FOR TUBES TO HEAT UP

To calculate the starting time of heating for the collectors we use the formula:

$$Time = t = \frac{Q}{\dot{Q}} = \frac{(H_{epdm/copper} + H_{water})}{\dot{q} A_s} \quad (22)$$

where, H is heat Capacity and A_s is surface area of 0.0616 m^2.

Table 8. Heat Capacity and Properties

Property	EPDM	Copper	Water
Density (kg/m^3)	1200	8940	1000
Specific heat (kJ/kg.K)	2.18	0.385	4.18
Volume (m^3)	$3.078x10^{-5}$	$3.078x10^{-5}$	$6.07x10^{-5}$
Heat Capacity (kJ/K)	0.105	0.0805	0.254

Starting Time for EPDM

t = 20 minutes

Starting Time for Copper

t = 22 minutes

The Relation between Starting Time of EPDM and Heat Flux

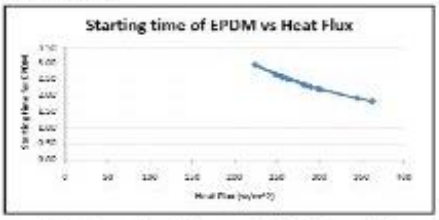

Figure 10. Starting Time of EPDM vs Heat Flux

The Relation between Starting Time of Copper and Heat Flux

Figure 11. Copper Starting Time for different Heat Flux

If we keep the outer surface temperature of tube equal to 70 ^{0}C and ambient temperature equal to 20 ^{0}C then by varying heat flux, time variations to heat up the tube for the required temperature of the outer surface is clear from the Figure 6.3 and 6.4.

6.8 Heat losses

The heat losses from the chamber are calculated by using relevant heat transfer equations and research paper results. The radiations absorbed by the tubes and base is about 90% due to the high absorptivity of EPDM and blackened surface with Aluminium substrate. 10% of radiations are reflected from blackened surfaces will strike the glass slab. Some of these radiations are reflected back because of their high incident angle which is greater than a critical angle which results in total internal reflection.

Now the major portion of these radiations which are absorbed by the tubes is conducted to water inside

the tubes. Convection heat transfer takes place at the surface of tubes and blackened Aluminium sheet which will increase the temperature of the air inside the chamber. Heat will also be delivered to air by radiations from the fore mentioned surfaces.
The difference between the outer and inner temperature of the tube has already been calculated. By using these formulae the heat losses are determined. Those are submitted in the calculation sheets.
Heat delivered to water inside the tube can be found out by:

$$Q_{water} = \frac{k}{\Delta x}(T_{s,out} - T_{s,in}) \quad (23)$$

where, K is thermal conductivity, Δx is thickness, $T_{s,out}$ and $T_{s,in}$ are exit and inlet temperatures of a pipe.

$$Q_{conv} = hA(T_{s,out} - T_a) \quad (24)$$

where, h is convective heat transfer coefficient, A is surface area, $T_{s,out}$ and T_a is the surface and ambient temperature.

$$Q_{conv} = \sigma\varepsilon(T_{s,out}^4 - T_a^4) \quad (25)$$

where, σ is Stefan-Boltzmann constant, Ɛ is the emissivity, $T_{s,out}$ and Ta is the surface and ambient temperatures.
The net heat transfer can be explained by the equation

$$Q_{Total} = Q_{water} + Q_{conv} + Q_{rad} \quad (26)$$

6.9 Flow Analysis

As Reynolds number is:

$$Re = \frac{\rho VD}{\mu} \quad (27)$$

The results show that the flow is laminar.

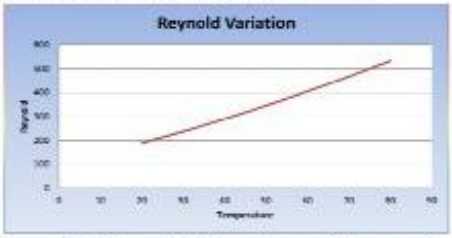

Figure 12. Reynolds Number vs Temperature

7 COST ANALYSIS FOR TWO SWH

Table 9. Cost Estimation for each Material in PKR

Material	Quantity	Price (PKR)
EPDM tube	108 ft	3030
Copper pipe	108 ft	10590
Base frame (Angle Iron)	2 (1m x 1m)	5880
Plywood	3 (8 x 4) ft	2170
Aluminum insulating Sheet	3 x 12 ft	700
Bonding Materials		840
Black Carbon powder	1 kg	126
Black paint	1 Ltr	280
Anti-Corrosion Spray	2	420
Insulated Tanks	2 * 15 Ltr	7000
Welding (Gas, brazing)		2800
Thermo pole sheet	2 x 3 ft	290
Copper Manifold	1 in, 2*7ft	4000
Collector & Tank stand		7000
Tube cutter	1	200
Glazed Glass	4 * (39*27) in	3530
Plumbing		3640
TOTAL		**PKR 52,496**

Table 10. Cost Comparison

Copper GTSC SWH	EPDM GTSC SWH
PKR 30,447	PKR 22,048

8 FABRICATION MODE

Fabrication is a real step towards the reality of any design project. Solar water heater requires deep focus in fabrication. Our key objective is to ensure cheap fabrication, so that it can be easily accessible to a common man. However, the criteria of effectiveness and reliability could not be neglected during the manufacturing. Since our project is based on production of two small solar water heater, in an experimental mode, to prove that EPDM provides as a best solar geyser. Therefore, fabrication of single solar geyser could not correct to be judged. For that we have to see its future success. Only a batch production can provide the cost effectiveness in fabrication in reality. However, special care has been taken in the design and fabrication of our Solar Water Heater. No part or item of the project is imported. All items and parts are purchased from the local market, in reasonable price. Furthermore, the assembly of all parts into a system is done manually without any help from industry or fabricator. Hence the production can be done simply by single house utility. The part used in fabrication mode of solar

water heater simply implies the general study of heating and it's widely available in the market. The time frame is satisfied according to the plan and the work is done under the time frame.

8.1 Components at Site

- Water storage tanks
- Adjustable Collector & Tank stand
- Triangular Glazed Thermo siphon Solar collectors (Base)
- Manifold (Headers & Risers)

Water Storage Tanks

Capacity of tanks is15 Ltr, Diameter of tank is 52 inch, length and width is 21x17 in.

Figure 13. Water storage Tanks

Adjustable Collector

Figure 14. GTSC Adjustable collector stand

Solar Collector (Triangular Glazed Thermo siphon)

The area of solar collector 1 m^2

Figure 15. Base Frame of GTSC

Manifold (Headers & Riser Assembly)

Manifold is an array of tubes that enables the flow of water inside the collector. It is the passageway of flow of cold and hot water. For manifold, two copper pipes of 1 in are taken in account. Its gauge is 20. The numbers of tubes, as evaluated are 30, so 30 riser tubes of about half inch (11mm) and calculated length (36in) are divided into piece.

Figure 16. Manifold - Header & Riser Assembly of Copper GTSC

Final module EPDM and Copper GTSC

Figure 17. EPDM GTSC (Right) and Copper GTSC (Left)

9 EXPERIMENTAL SETUP RESULTS

9.1 The experimental values for the Copper GTSC

Table 11. Temperature Reading of Copper GTSC for December

Time	Temperature (°C)
8 am	43
9 am	51
10 am	59
11 am	63
12 pm	74
1 pm	71
2 pm	69
3 pm	65
4 pm	58
5 pm	55

9.2 The experimental values for the EPDM GTSC

Table 12. Temperature Reading of EPDM GTSC for December

Time	Temperature (°C)
8 am	40
9 am	46
10 am	55
11 am	61
12 pm	68
1 pm	64
2 pm	62
3 pm	54
4 pm	52
5 pm	50

9.3 Performance of SWH in December

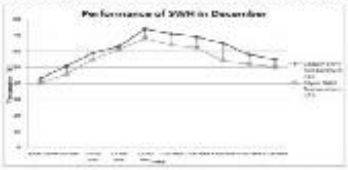

Figure 18. Performance of SWH in December

10 CONCLUSION

The testing result yields that both geyser are functional. The aim of the project was to build a cost effective solar geyser, and that is fabrication from the EPDM (rubber) tube. The second objective of its compare to the solar geyser using copper as a solar absorber is also tested. Concluding we obtained that Copper is acting as a best solar absorber, giving output of hot water quickly. While EPDM takes time, but, it has to be noted that during research experiment it is verified that if we use EPDM for three consecutive days, its thermal conductivity increases. It means the more we use EPDM tube the more it will be acting as a good solar absorber. Compare to copper in beginning it is not equal, but with passage of time it's heating capacity increases due to inherent properties. It was not hidden, that copper is conventionally a best choice as a solar absorber. Therefore, it comes best to be a solar water heater. But seeing its cost, estimating three times to that of EPDM, it's not favorable for a common man. On the other hand, EPDM can be a suitable replacement to all of these conventional solar absorbers. Its performance is increased day to day, as it is practically tested. The aim of making awareness to the common man in our nation can be fulfilled through the use of EPDM as a Solar Water Heater. The fabrication cost is relatively high as compare to market, as it is not been fabricated in batch. It is experimentally fabricated and only its proof to concept model is tested. Hence, if the government takes seriousness in developing solar plants to drive the nation advancement in market, then the price could go further down. In this way, we could curb the conventional energy use and could utilize the better use of renewable energy such like Solar Energy. Also, if it is manufactured on an industrial scale, the price could be reduced significantly.

ACKNOWLEDGEMENTS

The authors are thankful to Prof. Dr. Shafiq R Qureshi for his support and authors would also like to thank Faculty of Mechanical Engineering PNEC NUST, Karachi for providing the lab facilities.

REFERENCES

[1] Mohammed, Mohammed J., Haitham M. Mikhlif, and Ahmed N. Abed. "Design Solar Box Cooker with Low Cost Materials." journal of the college of basic education 13, no. 59 (2009): 71-78.

[2] Ateeque Ahmed, Anjum Khalid, Bilal Ahmed, Sumiya Mohsin: Impact of Solar Radiation on Building Envelope using Energy Plus Software. 7th International Mechanical Engineering Congress 24-25 March 2017, IEP Karachi; 03/2017

[3] Islam, M. Raisul, K. Sumathy, and Samee Ullah Khan. "Solar water heating systems and their market trends." Renewable and Sustainable Energy Reviews 17 (2013): 1-25.

[4] Qureshi, Shafiq R., Waqar A. Khan, and Waqas Sarwar. "EPDM based double slope triangular enclosure solar collector: a novel approach." The Scientific World Journal 2014 (2014).

[5] Khan, Nasim A, "Solar Energy Guide and Data Book for Pakistan". College of Electrical and Mechanical Enineering.

[6] Masters, Gilbert M. Renewable and efficient electric power systems. John Wiley & Sons, 2013.

[7] J. Holman, Heat Transfer, McGraw-Hill Science/Engineering/Math, New York, NY, USA, 9th edition, 2001.

[8] B. Norton, "Anatomy of a solar collector: developments in materials, components and efficiency improvements in solar thermal collector systems," Refocus, vol. 7, no. 3, pp. 32–35, 2006.

[9] Y. A. Cengel, Heat Transfer: A Practical Approach, Mcgraw-Hill, Desoto, Tex, USA, 2nd edition, 2002.

ENERGY EFFICIENCY IMPROVEMENT OF WATER-COOLED CHILLERS USING ORGANIC RANKINE CYCLE INTEGRATED WITH RENEWABLE ENERGY SOURCES

M. T. Nasir* and H. H. Taimuri
Pakistan Air Force-Karachi Institute of Economics and Technology, Korangi Creek, Karachi

*Corresponding author. Tel.: +92-3452658511;
E-mail address: tauseef@pafkiet.edu.pk (M. T. Nasir)

ABSTRACT

The modern dilemmas of electricity deprivation, and degradation of environment has urged a search for clean and sustainable energy resources as well as to improve the existing equipment. In this research owing to the drive to improve the existing technologies, a scheme to improve the industrial (large sale) chillers has been made. The prospects of using the chiller's condenser outlet water and improving its energy content by the utilization of the renewable energy sources to power an Organic Rankine Cycle (ORC) is studied. By using R134a as the working fluid for the ORC system and raising the condenser outlet temperature to 110°C of a 15 ton chiller, the proposed scheme improves the COP of the chiller from the rated value of 4.5 to 5.87.

Keywords: Organic Rankine Cycle; Air Conditioning; Chillers

1 INTRODUCTION

Large scale chillers (considered to be 15 tons and above) are widely employed to fulfill air conditioning requirements in offices, shopping malls, hospitals etc. Most of these chillers are based on the Vapor Compression Cycle (VCC) technology and consumes vast amount of electricity. The general schematic and the temperature-entropy diagram of the VCC are given below:

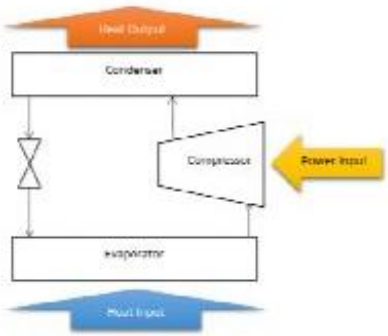

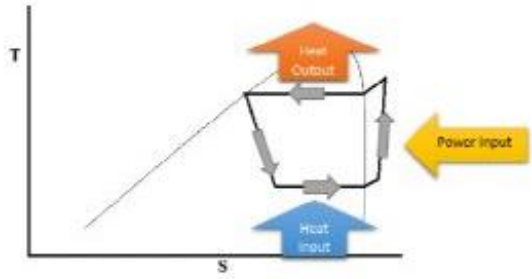

Fig 1. (Top) Schematic and (bottom) Temperature-entropy (T-S) diagram of a Vapor Compression Cycle.

The conventional configuration of an air conditioning chiller, positioned on buildings is presented below in Fig.2.

According to an estimate by Li et.al [1], around 30-50 % of electricity supplied to urban areas, during the summer season is being utilized by the air conditioning application. Reducing the consumption of electricity for air conditioning application thus can have far reaching positive effects. Realizing the importance of this issue,

several researches have been conducted and can be found in Ref. [2-5]. In this proposal, a unique scheme, and according to the best of author's knowledge not found anywhere has been proposed.

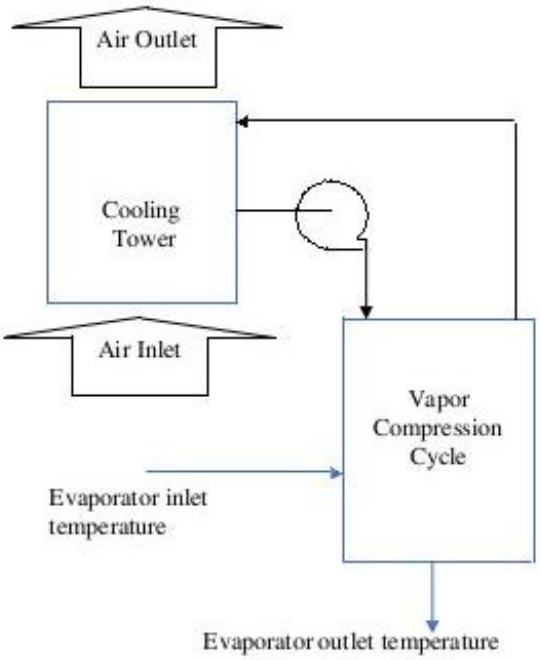

Fig 2. Conventional configuration of an air conditioning chiller

To enhance the efficiency of the existing chillers, thereby reducing the electricity consumption a scheme is proposed. In this proposed scheme, an Organic Rankine Cycle (ORC) and renewable energy harnessing equipment is attached in the circuit to make the existing chillers efficient. ORC is a technology that employs organic compounds as its working fluid instead of water. As the normal boiling temperature of these compounds is much lesser than that of the water, this technology holds the capacity to generate mechanical power using low grade heat. This low grade heat can come from flat plate solar collectors, geothermal sources, low caloric value biomass, various sources of waste heat in industrial and commercial processes and utilities, or even a combination of these sources [6]. The schematic and the T-S diagram of the ORC are shown below:

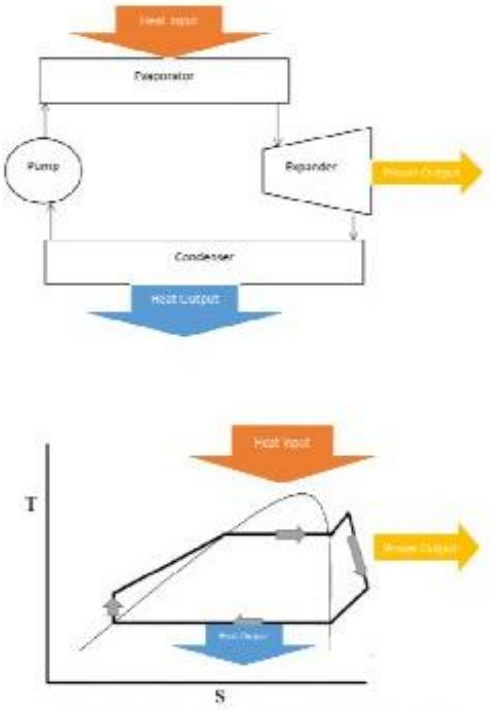

Fig 3. (Top) Schematic and (bottom) Temperature-entropy (T-S) diagram of an Organic Rankine Cycle

2 PROPOSED SCHEME

The proposed scheme alters the layout of the conventional chiller systems by enhancing the temperature of the VCC condenser outlet temperature by using renewable energy sources, and passing it through the ORC. The schematic of this scheme is provided in Fig. 4. The pressure of the condenser chilling water is raised by using the pump 1 and divided into three streams. The pressure of this stream is raised to ensure no formation of steam, as a component of this stream is supposed to be heated to above its normal boiling point temperature. One of the streams is passed through the recuperator and then to the renewable energy sources. Here the temperature of this stream is raised and then sent to the evaporator of the ORC unit. From the other two streams, one of them (B) is sent to the ORC condenser. The streams are then mixed together to obtain an intermediate temperature stream at point H. This stream then passes through the recuperator, then to the cooling

tower, from where it shall go back to the condenser, thereby completing the loop.

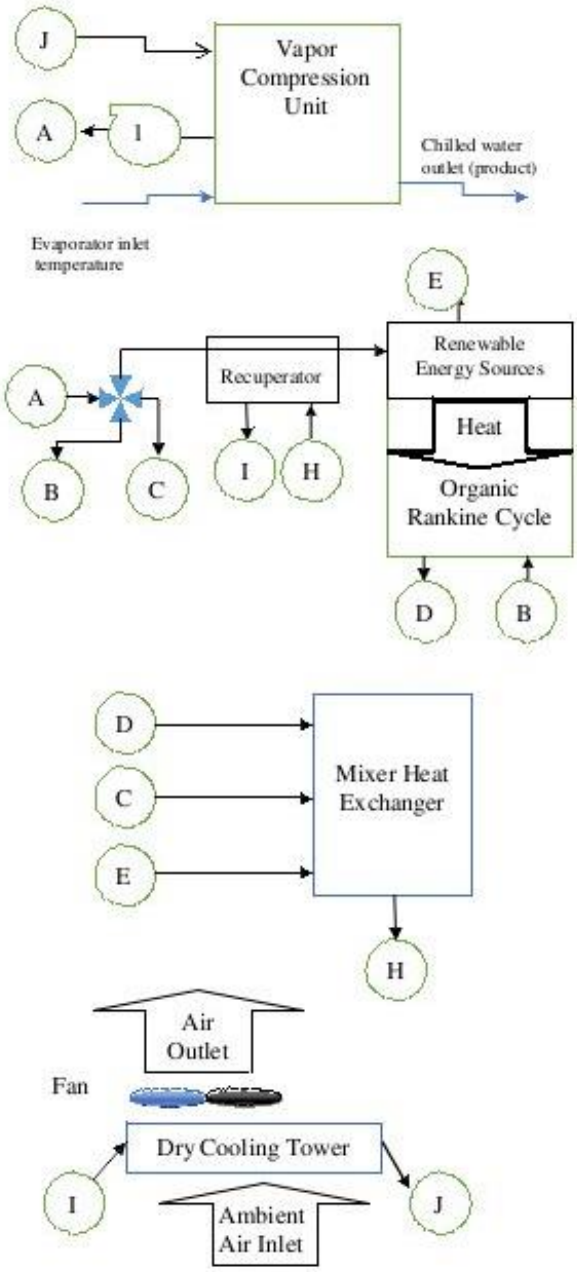

Fig 4. Schematic of the proposed scheme

3 PRELIMINARY ANALYSIS AND RESULTS

The heat losses and pressure drops are considered negligible within pipes and heat exchangers. And the isentropic expansion of the expander in the ORC section is considered to land at saturated vapor. R134a is considered to be the ORC working fluid. The chiller capacity is assumed to be 15 ton, and the outlet temperature and flow rate of its condenser chilling water is considered to be 45°C and 3 kg/s. Such conditions are approximated after the Carrier AquaSnap ® 30 MP [7]. To conduct the basic results, it is assumed that the renewable energy sources are used to raise the temperature to 110°C. The ORC condenser temperature is taken to be at 60°C. The pinch point in the heat exchangers of the ORC is assumed to have a value of 5°C, and the recuperator effectiveness is assumed to have a value of 0.7 (70 %). The isentropic efficiency of the pump and the expander are chosen to be 90 % each. The mass flow rate of the heat source entering the ORC evaporator is taken to be 0.5 kg/s. And the temperature increment of the ORC condenser was assigned a value of 10°C (that is from 45°C to 55°C). The variation of the net work done, the ORC evaporator outlet temperature, mass flow rate of the ORC system, and the outlet temperature at point H (please see fig.4) against the evaporator pressure are presented below, in fig 5, 6, 7, and 8:

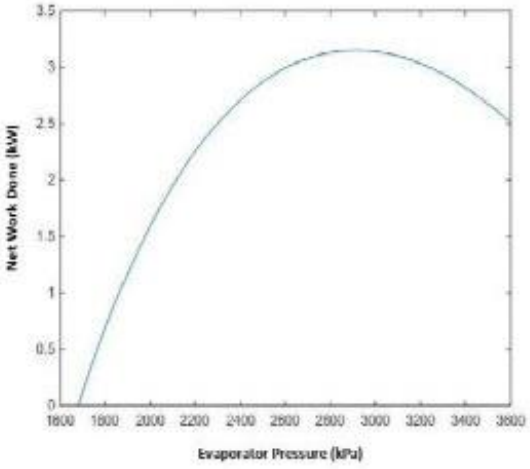

Fig 5. Variation of net work done against the evaporator pressure (Pressure limit from saturation temperature a 60 °C to 90 °C)

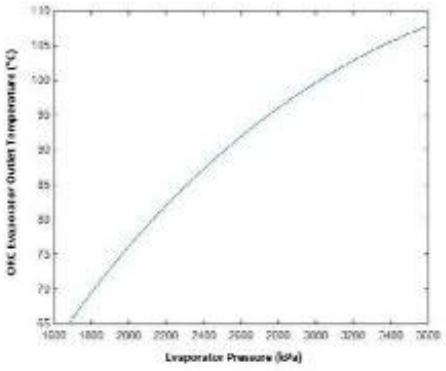

Fig 6. Variation of ORC evaporator outlet temperature against the evaporator pressure

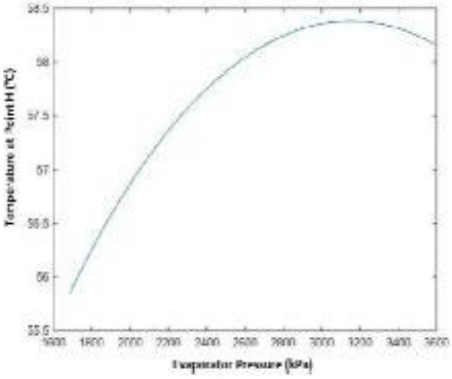

Fig 7. Variation of temperature at point H against the evaporator pressure

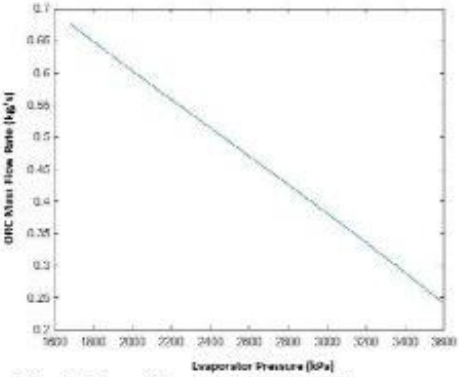

Fig 8. Mass flow rate against the evaporator pressure

Considering the maximum net work done to be the primary objective, the results at the optimum point are as follows:

Heat source temperature = 110°C.

Pump 1 (please refer to Fig 4.) = 0.05 kW. The work done required to raise the pressure of the condenser chiller from 1 atm to around 170 kPa (saturation temperature of water at 115°C).

Expander work output = 3.66 kW.

ORC pump work require input = 0.52kW.

Net work done = 3.14 kW.

Evaporator saturation pressure = 2728 kPa.

Condenser saturation pressure = 1628 kPa.

ORC mass flow rate = 0.41 kg/s.

Turbine inlet temperature = 87°C.

Temperature at point H = 58°C.

Temperature at the inlet of the renewable energy sources = 57°C (a gain of 12°C from the VCC condenser temperature of 45°C).

Inlet temperature of the cooling temperature = 56°C.

Fan power consumption = 1.1 kW (considering he air velocity to be 10 m/s for the conventional case (plee see Fig 2.), and carrying out the basic calculations)

Rated original COP [7] = 4.5.

New COP = 5.87.

Conclusion

The improvement in the energy is enormous but additional concerns particularly related to cost, and operations need to be assessed way more thoroughly to portray the complete picture. In this arrangement, further improvements can be made,

for example by using recuperators at additional places, such as stream (E) in Fig 4.

To the best of author's knowledge such a proposed scheme has never been analysed and therefore offers a great potential for future research and improvement.

REFERENCES

[1] C. Li, J. Zhou, Y. Cao, J. Zhong, Y. Liu, C. Kang, Y. Tan, Interaction between urban microclimate and electric air-conditioning energy consumption during high temperature season, Applied Energy 117 (2014) 149-156.

[2] C. W. Chan, J. Ling-Chin, A. P. Roskilly, A review of chemical heat pumps, thermodynamic cycles, and thermal energy storage technologies for low grade heat utilization, Applied Thermal Engineering 50 (2013) 1257-1273.

[3] K. J. Chua, S. K. Chou, W. M. Yang, Achieving better energy-efficient air conditioning – a review of technologies and strategies, Applied Energy 104 (2013) 87-104.

[4] J. S. Brown, P. A. Domanski, Review of alternate cooling technologies, Applied Thermal Engineering 64 (2014) 252-262.

[5] M. Zeyghami, D. Y. Goswami, E. Stephanakos, A review of solar thermo-mechanical refrigeration and cooling methods, Renewable and Sustainable Energy Reviews 51 (2015) 1428-1445.

[6] P.Colonna, E. Casati, C. Trapp, T. Mathijssen, J. Larjola, T. E. Turunen-Saaresti, A. Uusitalo, Organic Rankine Cycle Power Systems: from concept to current technology, applications and outlook to the future, Journal of Gas Turbines and Power 137 (2015) 100801-1 to 100801-19.

[7]http://www.carrier.com/commercial/en/us/products/chiller-components/water-cooled-chillers/30mp/

Carbon Steel calibration tube inspection by Internal Rotary Inspection System (IRIS) Technique

Faisal Ahmed*, Dr. Syed Anwar ul Hasson, Mr. Mahmood Khan

*email: faisalcrk@gmail.com, contact no: +923444157525

ABSTRACT

NDT plays a key role in the field of tube inspection. IRIS (Internal Rotary Inspection System) is an ultrasonic based NDT technique designed for the inspection of defects in tubes. Multiview software version 6.0 is used with MS-5800 equipment for the inspection and results analysis. Carbon Steel (grade C-1020) calibration tube which is prepared according to ASME standard Section-V Article 17 is inspected through IRIS. 5 defects, include OD groves, tapered flaw and short and long wall losses, of different dimensions are detected and discussed. C-scan shows different color intensity according to defect depth and B-scan shows the circumferential wall loss of tube at the position of defect. All these results are obtained at very low probe pulling speed of almost 4 mm/sec. The analyzed values of defect are very close to the exact values and shapes of defect are read very efficiently by instrument.

INTRODUCTION

Heat transfer is the key process that occurs in most of the industries inside heat exchangers and steam generators. So their performance and availability need to be set up to the mark through health monitoring for continuous production and profitability. The major concern during inspection is the condition of tubes. Usually Carbon steel tubes are generally found in conditions where either steam or water is present on one side of the tube. These conditions are also some of the most corrosive so their damage probability have increased a lot [1].

In order to know the condition of tubes, different NDT methods are developed for inspection of different tube materials. Generally for the non-ferromagnetic materials, Eddy Current testing method is more proficient than the other NDT methods [2]. But in the case of ferromagnetic materials, like carbon steel, which also is a great proportion, in service, Eddy current method cannot be used due to large variations in permeability of carbon steel [3] and so require a technique on which this change has no effect. IRIS on the other hand is an ultrasonic based technique which is useful for both ferromagnetic and non-ferromagnetic materials quite efficiently.

This paper presents the work of inspection through IRIS technique on a carbon steel calibration tube of grade C-1020. This tube is prepared according to ASME Section-V Article 17 standard [4]. Preparation of calibration tubes of same material and similar dimensions with artificial defects is important to set the equipment parameters near to the actual scenario.

The basic principle of IRIS is given in the methodology along with the procedure and instrument details. The specification of tube and major parametric values that are set during inspection are also provided. Then the results of inspection and the discussion upon different scans gained during inspection, their patterns, values of defect, comparison of analyzed values and actual value of defect and probable reasons behind all that undesired black spots and regions are descriptively mentioned under the heading of results and discussions. The conclusion of this work is presented at the end and summarize the findings through this procedural work.

METHODOLOGY:

IRIS equipment includes: (i) The test head with probe, mirror, water driven turbine and centering device (ii) the water supply regulator, water pump, filter to remove foreign particles, hoses to connect and cables to send and receive the signals and (iii) the Acquisition unit and laptop with installed MutiView software version 6.0. The schematic of the test head with a high frequency ultrasonic transducer and rotating mirror is shown in figure 1. A small turbine rotor is connected to a mirror. The turbine is rotated by water (couplant), pumped by a submersible pump. Each rotation of the mirror constitutes one revolution of the ultrasonic beam and shows a rectilinear picture (B-scan) and color picture (C-scan). A target pin in the turbine interrupts the beam during each revolution, thus providing the pulse for initiating the trigger onto screen [3].

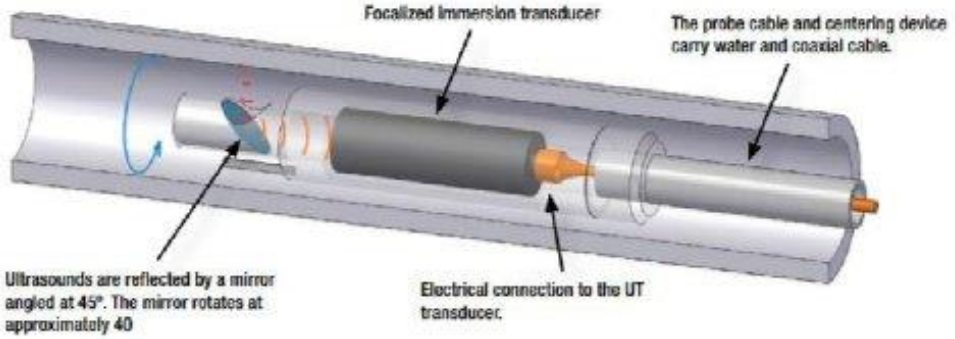

Figure 1. Schematic of IRIS head includes high frequency ultrasonic transducer and mirror attach with water driven turbine

In the first step of inspection, the system is calibrated onto the sound part of a calibration tube of same material [5]. This ensures that the system parameters are selected in the said ranges correctly and the instrument is reading the sound part the way it should be. The calibration tube is of carbon steel of length 4 ft., Outer Diameter of 19 mm and wall thickness of 2.3 mm. Artificial defects are produced on this tube according to ASME Section-V Article 17 [4]. The C-Scan of sound part is shown in figure 2. Values of some important parameters that are set during this first step are mentioned in table 1.

Table 1. Parametric values set for the calibration at sound portion of tube

Parameter	Value
Gain 1	31 dB
Gain 2	45 dB
Blanking	0.7 mm
RPM of turbine	44
Probe Pulling Speed	4 mm/sec
Pulse Repetition Frequency (PRF)	10,000
DAC Slope	0.9375
Probe Delay	23.08 (µs)
Target gate from	26.38 (µs)
Target gate to	29.36 (µs)

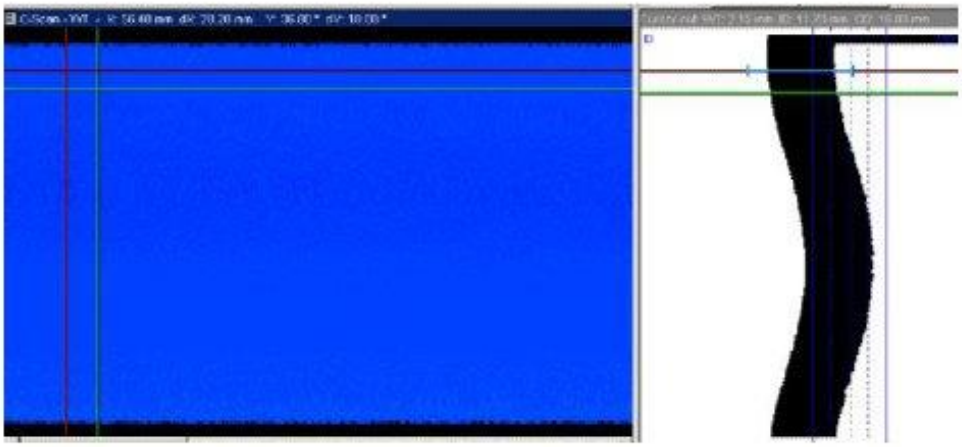

Figure 2. B and C-scans of sound part of calibration tube of carbon steel

After the instrument is calibrated at sound part, then the whole tube is inspected [5-6] by putting the tube in a water tank that also contains pump. This arrangement is adopted only to not makeup the water every time for the pump and it does not affect the results. The tube is placed such that location of defect 1 is on the far side and defect 5 is on the near side of guide tube from which the probe is inserted and pulled out from the tube. According to the ASME code, the inspection is always done while pulling the probe, so this rule is followed during acquisitions. The inspection is done at a very low probe pulling speed of almost 4 mm/sec. The turbine speed is regulated through the opening and closing of a valve attached to the filter in the path of water flowing towards the test head. The arrangement is shown in figure 3.

Figure 3. Water filter along with rpm controlling valve, pressure gauge and black wire to send and receive signals

The arrangement of probe head with its constituents is shown in figure 4.

Figure 4. Complete arrangement of inspection probe, includes guide tube, plastic centering device, transducer and turbine turbine

RESULTS AND DISCUSSIONS:

A carbon steel tube of 4 ft. length is inspected through IRIS technique. 5 defects of different sizes and shapes are inspected and detected by the equipment and are analyzed by software through red and green cursors [6].

Figure 5 shows the C-scan of carbon steel tube. When probe is pulled, C-scan start developing from left to right and live B-scan continue to develop along with axial probe movement. 5 defects of different size and shapes are detected while probe moved inside the tube. These 5 defects are named as defect 1, defect 2, defect 3, defect 4 and defect 5 (from left to right on C-scan). There is also a black region at the right bottom corner in C-scan in figure 5. This is due to the sudden change in speed of turbine and noise inclusion when the probe is at the near end of tube and all this is occurs due to the jerk of hand as when the probe pulling is almost complete and probe is at the near end of the tube (the end where the guide tube of steel is present, near the hands of operator), the operator experience difficulty in probe movement due to smaller diameter of guide tube from which the centering device cannot easily pass [5]. Due to this the scan of defect 5 shows red color a lot which is not the actual color dedicated to 40% WL, so defect 5 is inspected separately and is

shown in later part of results and discussions. Figure 5 also contains the B-scan which is vertical and D-scan which is horizontal. B-scan is of the sound part and usually of that region which is lying under the vertical red cursor. UT Gain Setting box shows the values of parameters set at the calibration and upon which the tube is inspected. The details of these defects are mentioned in table 2. Wall thickness of these defects are measured by ultrasonic thickness meter DMS-2 whose least count is 0.01 mm. Several readings of same defect I taken and the average values are mentioned in table above. Note that the DMS-2 meter is first calibrated at 3 mm thickness block and then all the values of wall thickness are measured

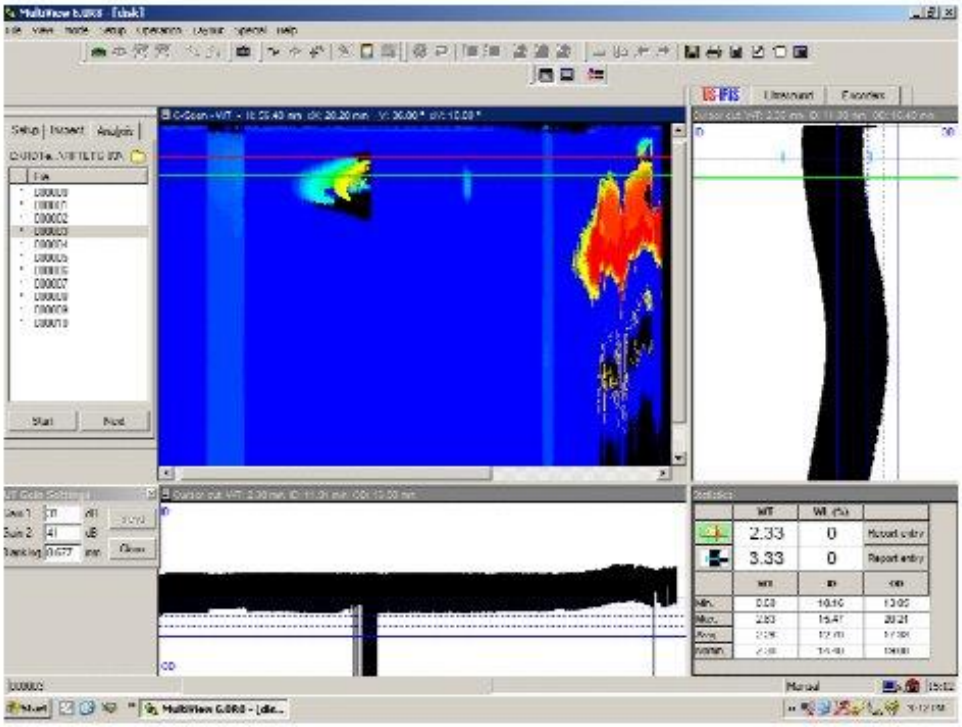

Figure 5. C-scan of a carbon steel tube, showing 5 defects of different size and shape

Table 2. Names and details of defects

Defect Name	Description	Wall Thickness (mm)
Defect 1	Long circumferential grove of 10% Wall Loss	2.083
Defect 2	Tapered flaw of 60% Wall loss at the deepest point	1.13 (at deepest point)
Defect 3	20% Wall loss long	1.885
Defect 4	Short circumferential grove of 10% Wall loss (WL)	2.087
Defect 5	Short wear scar of 40% Wall loss	1.087

Defect 1:

Defect 1 is a long circumferential grove of 10% WL and is scanned first. Actual figure of this defect is shown in figure 6 and its C-scan is shown in figure 8. Figure 8 shows the value of defect, when analyzed through the software by putting the red cursor onto the scan, is 9% WL which is very close to the actual value of defect which is 10% WL. B-Scan is also smooth because of no other defect except the wall thinning uniformly across the circumference. The black little regions around the defect are due to the deflection of some of the ultrasonic waves away from probe from the edges of defect [5]. One important thing to mention here is the shape of defect which is read excellently by the equipment.

Figure 6. Actual diagram of defect 1

Defect 2:

This is a tapered flaw which has 60% Wall loss at the deepest point and shown in figure 7. The C-scan of defect is shown in figure 9. The value of defect is read as 56% through software which is quite close to actual value 60% WL. B-Scan also show the wall thinning of tube in the region of defect. The changing of color inside the scan of defect is because this defect's deepest value is 60% WL and reduce to nominal tube thickness of 2.3 mm. The shape of the defect read excellently by the equipment but the complexity of shape cause the deflection of ultrasonic waves in larger amount and so the black region exist inside the scan especially near the deepest edge. The black strips which are extended towards the right side in the B-Scan tells us the absence of back wall echo from the boundaries of defect which again indicate towards its complexity.

Figure 7. Actual Diagram of defect 2

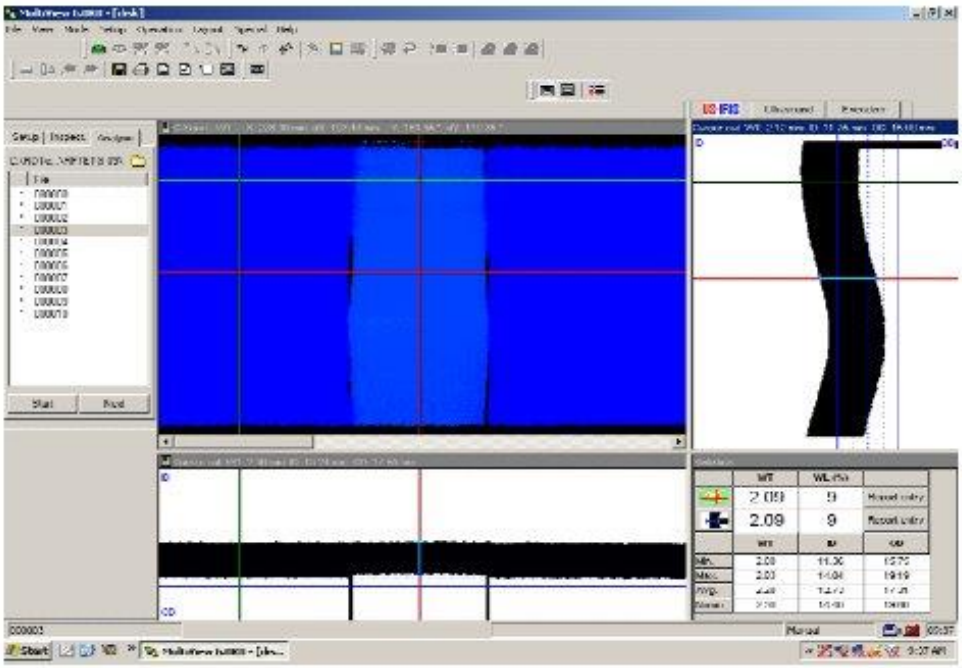

Figure 8. B and C-scans of defect 1 along with the analyzed value through software

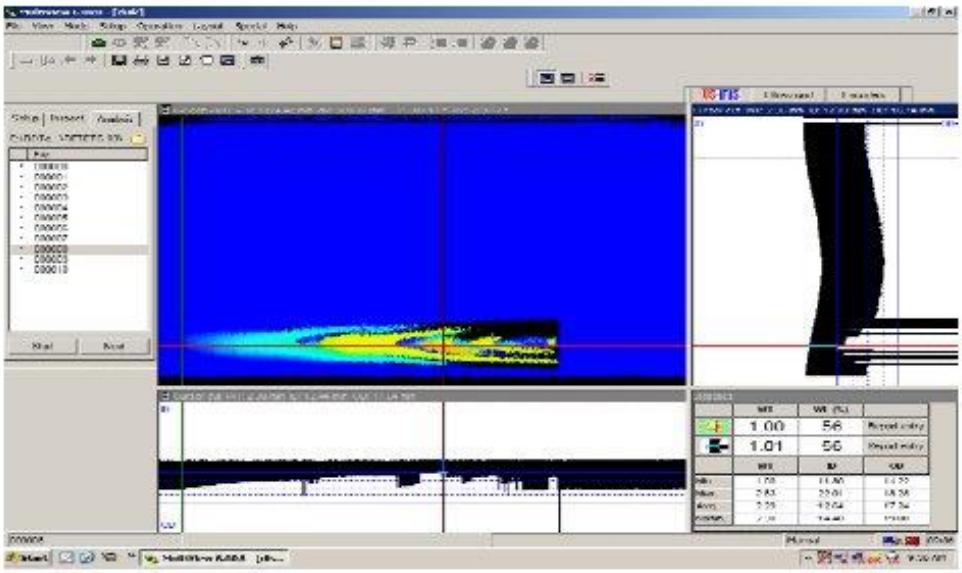

Figure 9. B and C-scans of defect 2 along with the analyzed value through software

Defect 3:

Defect 3 is a 20% WL long. Actual diagram is shown in figure 10 and its C-scan is shown in figure 12. The value of defect when analyzed through software is 18% WL which is very accurate when compare with the actual value of 20% WL. B-Scan also shows notable wall thinning across the cross section of tube. The little black spots around the defect are due to the deflection of some of the ultrasonic waves from the edges of defect away from probe. The shape of the defect read very well by the equipment.

Figure 10. Actual Condition of defect 3

Defect 4:

Defect 4 is a short circumferential grove of 10% WL. Its actual diagram is shown in figure 11 and its C-Scan is shown in figure 13.

Figure 11. Actual Condition of defect 4 over the surface of tube

The value of defect read and analyzed by software is 8% WL which is close to 10% WL, the actual value of circumferential grove. B-scan is smooth and show no other defect present n this circumference except the uniform wall thinning which is analyzed. C-scan shows the shape of

defect accurately but the black spots around the defect are due to the deflection of some of the ultrasonic waves from the edges of defect away from probe.

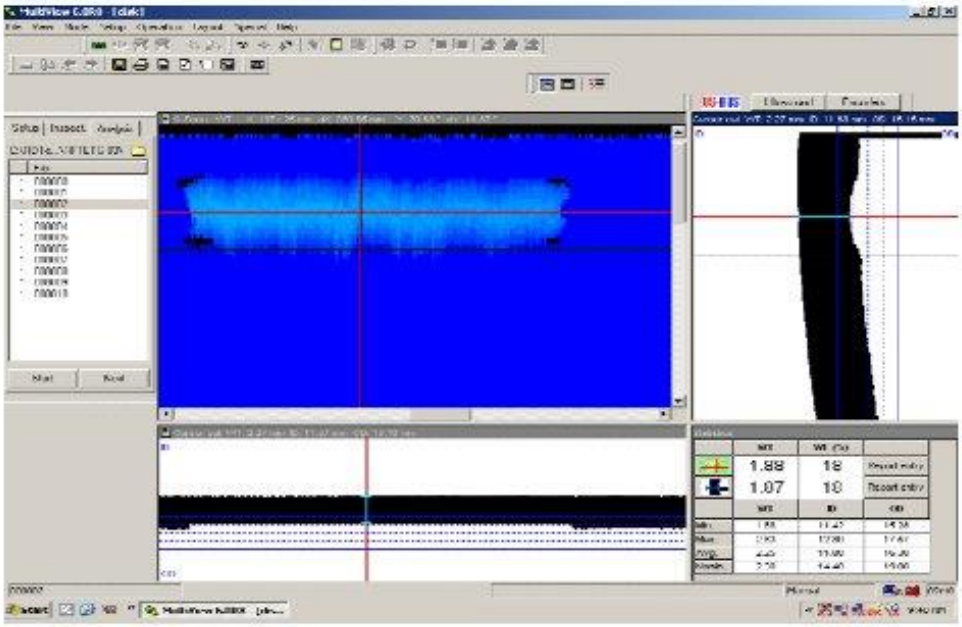

Figure 12. B and C-scans of defect 3 along with the analyzed value through software

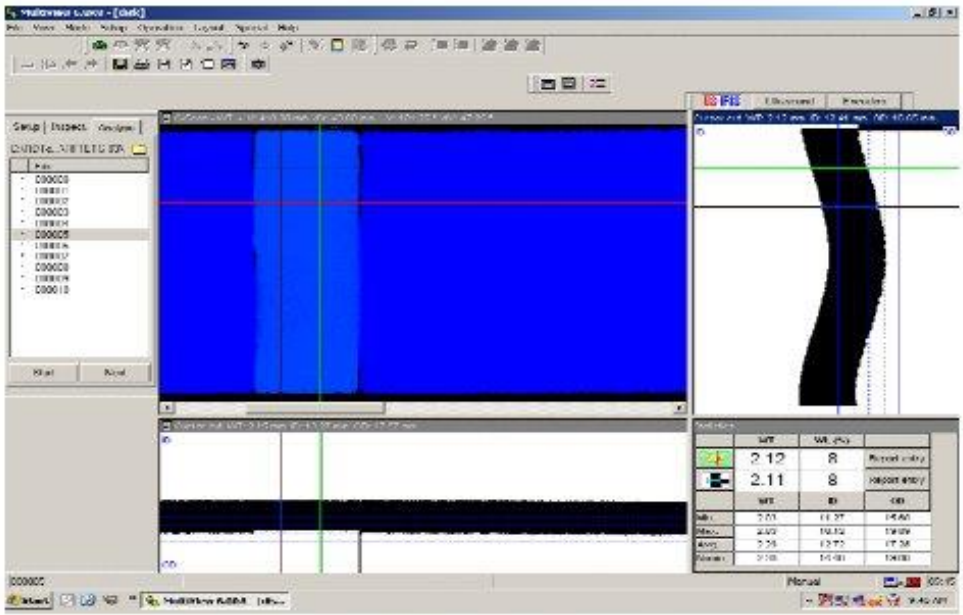

Figure 13. B and C-scans of defect 4 along with the analyzed value through software

Defect 5:

Defect 5 is a short wear scar of 40% Wall loss and is inspected separately by keeping this defect on the far side to guide tube to avoid any jerks during pulling or noise to interrupt the scan. The actual condition of this short defect is shown in figure 14 and its C-scan is shown in figure 15.

Figure 14. Actual condition of defect 5 onto the surface of tube

As this is a very short and edgy defect, so the true value of defect is very difficult to measure and requires very slow pulling speed around 3 mm/sec, that's why there are black strips in both B-scan and C-scan which indicates the absence of back wall echo due to the deflection of ultrasonic waves away from the probe and not received from the boundaries. But the shape of defect is read very well by the equipment. These type of scars are generally produce due to wear onto the surface

when any impact of foreign tool happens onto the tube surface especially during machining processes.

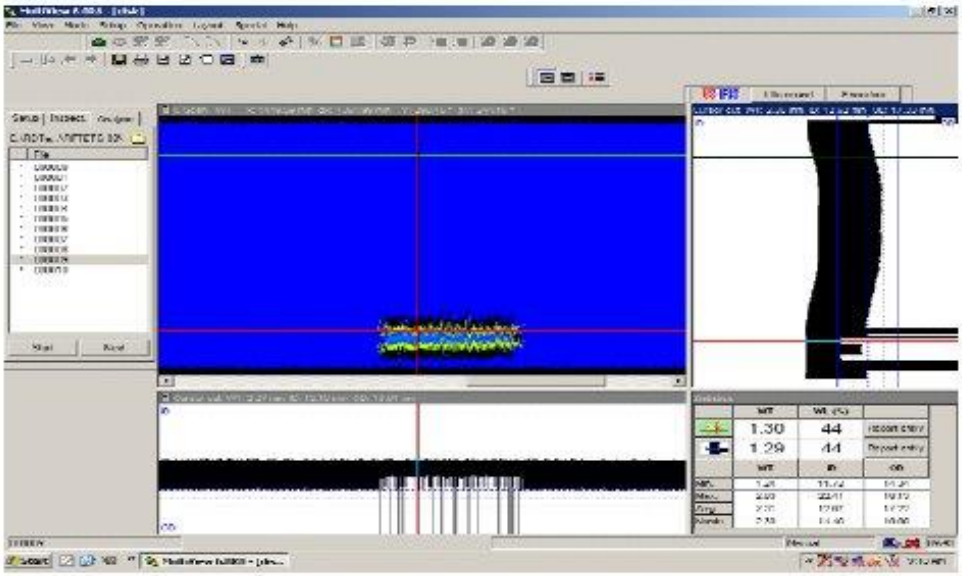

Figure 15. B and C-scans of defect 5 along with the analyzed value through software

CONCLUSION:

A carbon steel tube is inspected through IRIS mode on Multiview MS-5800 equipment. It contains artificially generated defects of certain dimensions. All the defects are discussed separately and descriptively under the heading of results and discussions and we can have some of these points as the conclusion of this experiment.

- The values of defects inspected through the technique and analyzed through the software are not exact but very close to the real dimensions of actual defect
- The color pellet is set accurately and so the colors accurately shows the intensity and depth of defect present onto the surface
- The shape of defect which is very important in any tube inspection is excellently read by the equipment
- The shape of the defect plays very important role in the determination of its exact value. The more is the edges and sudden changes in thicknesses of tube wall, the more we move away from the actual wall loss values of defect and more it requires to inspect that defect more steadily and by putting more efforts to it. Also the edges cause the ultrasonic waves to deflect away from the probe and they are nor received and so the black region introduced into the scan.

REFERENCES:

[1]. Walter Matulewicz, Gilles Rousseau and Marc Grenier, "Recent Advances in Carbon Steel Tube Inspection",

[2]. Anmol Birring, "Eddy Current Testing vs. Ultrasonic IRIS for Inspection of Heat Exchanger Tubing" Non-destructive Evaluation, Inc.

[3]. A. JOSEPH, GOVIND K. SHARMA AND T. JAYAKUMAR, "Ultrasonic internal rotary inspection system (iris) for heat exchanger and steam generator tubes", Journal of Pure and Applied Ultrasonic, Volume 31 (2009) pp. (24-30)

[4]. ASME Section V, Article 17

[5]. OLYMPUS IRIS Setup Guide, Manual Version B, June 2008

[6]. OLYMPUS MutiView™, User's Manual, Software Version 6.0, October 2003

Process optimization for flue gas scrubbing using ionic liquid as solvent

Bilal Kazmi[1*], junaid haider[2], saud Hashmi[3],Zahoorul Hussain Awan[1], shahzar khan[3]syed john hassan zaidi[1],

[1]Department of Chemical Engineering, NED University of Engineering and Technology
[2]School of Chemical Engineering, Yeungnam University, Gyeongsan 712–749, Republic of Korea
[3] Department of polymer and petrochemical Engineering, NED University of Engineering and Technology

[*]Corresponding author. Tel.: +923122600296
E-mail address: bilalkazmi91@gmail.com (Bilal Kazmi)

ABSTRACT:

The human development and progress have gradually altered the environment. A continuous transformation of the natural resources is required in order to keep the cultural and living conditions of the people. A growing energy demand is product of the use of faster transportation means, and as well of the industrialization. Gas separation processes became a key operation for diminishing the conventional green house contaminant gases and improving energy balance in the industry. The CO_2 is produced by the refining and the chemical sector as a by product of manufacturing processes. The goal of this research to study the potential of the Room Temperature Ionic Liquids (RTILs) as absorption solvents for the industrial separation of CO_2 from flue gas. The designed solvent is aimed to have the most promising combination of ions in the liquid structure and includes the identified specific functionalities. Then as a consequence of the structural composition and chemical functionalization of the RTILs, the performance of absorption agent is expected to be improved.

Keywords: ionic liquid, physical absorption, Aspen Plus, MDEA, Cosmo Sac

1. INTRODUCTION

The total World's population was carefully assessed to be promptly 7.2 billion in 2013. Statistic future projections shows it's increment to 9.5 billion by 2050 and to 10.9 billion by 2100 and so is there local demand for the energy is creeping as well. Modern day power plants traditionally using fossils as fuels (the Coal Power Plants (CPP)) are being used as reliable energy sources for the power generation across the developed world mainly because of the more significant calorific values & easy processing of coal. The coal fired power plants constitutes a significative portion for power generation across the world [1]. Therefore, Climate change is considered as a critical issue in the world occurring mainly because of global warming [2]. Global warming is typically defined with the adequate level of greenhouse gas emissions(GHGs). However, when coal is typically burnt for energy production the major issue encounters due to its burning is direct emissions of greenhouse gases (G HG's) which constitute mainly of carbon

dioxide (CO_2) & sulphur dioxide (SO_2) exiting the stacks as flue gases.

Middle income countries like Mexico, Nigeria, Pakistan and Philippines are presently considered as the major emitters in terms of environmental discharge. Pakistan is currently establishing various coals - fired power plants based projects to meets its energy requirements. In 2016, Pakistan's CO2 emissions per capita were 0.92 metric ton [3]. World bank also issued an alert in their recent report in 2018 which claims that by 2050 the average temperatures are projected to increase to 2.5C under the climate sensitive scenario which represents a future in which some collective action is initiated to limit greenhouse gas emissions (GHGs) and up to 3.0C under the carbon intensive scenario[4]. Pakistan environmental protection agency also stated in 2009 that there was a large presence of high suspended particulate matter in air and it is found to be three times higher than the safe standards [5]. Although Pakistan's CO2 emissions per capita fluctuated substantially in recent years but the CO2 Control remain up until now the problem to be combating to prevent any significant consequence [6,7].

Carefully controlling the elevated level of potential contaminants in the flue gases is imperative as it is undoubtedly an established fact that these potential pollutants are traditionally the probable cause for the ever – rising phenomenon of global warming which is undoubtedly gaining serious attention worldwide. To typically limit the enhanced greenhouse effect, there have been invariably several new methodologies explored & developed with ample time. Carbon capture & Storage (CSS) has been the most widely accepted economical methods among others on large-scale application to reduce the greenhouse emissions. By typically employing this holistic approach, the continual use of fossil fuel without significantly contributing to global warming can be guaranteed. There undoubtedly exists a large dependence on fossil fuel as a reliable source of renewable energy for many marked years, which statistically constitutes to about 85% of the total domestic & worldwide use. Apart from being typically the conventional & most common sources of energy; the considerable difficulties which ranges from technical, fiscal and social aspects instantly puts hinders the considerable progress of renewable sources as possible alternatives to fossil fuel for successful commercialization. So, the viable option of continual use of fossil fuels must be critically worked before actually considering some other alternative just to evade the imminent danger of global warming [8].

Ionic Liquids (ILs) are inevitably the new & improved synthesised solvents that have scarcely gained prominent consideration in last few years [9, 10]. They are salt in liquid state with their melting point at or around the room temperature. Ionic liquids consist merely of a large organic cation (Imidazolium[11]pyridinium[12]pyrrolidinium[13]quaternary ammonium[14] & quaternary phosphonium[15]) & inorganic anion (iodide, bromide, chloride, tetrafluoroborate[16], hexafluorophosphate[17],trifluoromethanesulfonate[18],bis(trifluoromethanesulfonyl) imide, etc. .ILs exhibits several overwhelming advantages against the amine based solvents which erroneously includes, negligible vapour pressure (thereby preventing the release of the solvent in the environment), lower corrosivity, thermal stability at elevated temperature, easy regeneration & greater flexibility in IL choice by merely employing different anion – cation configurations for customized applications & most importantly low energy requirement for solvent regeneration

[19].The potential IL candidate for the scrubbing process for flue gas capture is inevitably required to demonstrate higher affinity & selectivity towards CO2 against the others such as, N 2, O2 and H2S which are also present in the flue gas stream [20].
In this complex scenario, process simulation should play a determinant role not only in the synthesis and analysis of the new processes based on the use of ILs, but also because it can contribute to conform multifactorial and consistent sets of criteria for selecting the ILs with optimized properties for a specific application but using process simulators to model ILs is not as simple as we thought it would be as most of the ILs are un included in the database of the simulators. So to model them, various predictive methods are combined for the determination of the properties of the IL and their mixture with process simulator. Therefore, COSMO (co-inductor like screening model) based thermodynamic models are providing a source of answer to all these queries as it based on the parameterization of the molecular structure of the component [20,21,22]. This thermodynamic model utilizes the quantum chemistry concept which represents an attractive approach for the prediction of the priori properties of the ILs. This methodology has started to be applied to areas classically covered by chemical engineering in the last years giving computational tools to researchers and process engineer as it requires only few general parameters which results in a realistic and good qualitative prediction of the ionic liquid properties taking advantage of this we have implemented the COSMO based model on the Aspen Plus and carry out various conceptual studies for the sustainable development of an alternative approach for the flue gas capturing mechanism using ILs.

2. PROPOSED DESIGN

2.1 Defining IL as a user component:

Since ILs are unincluded in Aspen Plus data bank. So to properly include them on Aspen plus one typically considers ILs as essential pseudo-components. For this specific purpose certain scalar properties of ILs are genuinely needed to be included which includes their fluid density, normal boiling temperature (Tb), molecular weight(MW),critical temperature (Tc), critical pressure (Pc), critical volume (Vc), acentric factor(ω) need to be specified. These unique properties are accurately calculated using correctly the standard method as stated valderama et al. since Cosmosac model does not require binary parameters.Therefore, for each component, it has six input parameters SGPRF1 to SGPRF5 are typically five molecular component sigma profile parameters which adequately describes the complex nature of the chemical components selected as well as the polarized charge over the component structure. CSACVL is invariably the component volume parameter always defined in cubic angstroms, regardless of chosen units sets.

2. THERMODYNAMIC MODEL

The sustainable development of the efficient thermodynamic predictive model for the necessary calculation of the thermo physical properties of ILs could be properly used as valuable tool to progressively reduce the experimental work [23]. The cosmosac thermodynamic model is ostensibly based on solvation concept which relates polarizability and electric field on the molecule surface. It uses wisely the concept quantum chemical calculation[24]. Developed Cosmosac model efficiently utilizes particular atoms as the fundamental building blocks for correctly predicting phase equilibrium instead of functional groups. This model formulation thoughtfully

provides a considerably more enormous range of practical applicability than group-contribution methods i.e. UNIFAC. The necessary calculation for liquid non ideality is only slightly more computationally intensive than activity-coefficient models such as NRTL or UNIQUAC[25]. Cosmosac and standard UNIFAC model can consider nearly same, because it is invariably does not wholly rely on the experimental prediction and almost virtually applicable to any system [26].

The Cosmo-SAC model carefully calculates liquid activity coefficients. The fundamental equation for the Cosmo-SAC model is:

$$\ln y_i = \frac{A_i}{a_{eff}} \sum_{\sigma_n} p_i(\sigma_m)[\ln \Gamma_s(\sigma_m) - \ln \Gamma_i(\sigma_m)] + \ln y_i^{SG} \quad (1)$$

$$\ln \Gamma_s(\sigma_m) = -\ln\left[\sum_{\sigma_n} p_s(\sigma_n)\Gamma_s(\sigma_n) exp\left[\frac{-\Delta W(\sigma_m \sigma_n)}{kT}\right]\right] \quad (2)$$

$$\ln \Gamma_i(\sigma_m) = -\ln\left[\sum_{\sigma_n} p_i(\sigma_n)\Gamma_i(\sigma_n) exp\left[\frac{-\Delta W(\sigma_m \sigma_n)}{kT}\right]\right] \quad (3)$$

$$p_i(\sigma) = \frac{A_i(\sigma)}{A_i} \quad (4)$$

$$p_s(\sigma) = \frac{\sum_i x_i A_i(\sigma) p_i(\sigma)}{\sum_i x_i A_i} \quad (5)$$

$$\Delta W(\sigma_m \sigma_n) = \frac{\alpha'}{2}(\sigma_m + \sigma_n)^2 + \Delta W^{HB}(\sigma_m \sigma_n) \quad (6)$$

$$\ln y_i^{SG} = \ln \frac{\varphi_i}{x_i} + \frac{z}{2} q_i \ln \frac{\theta_i}{\varphi_i} + l_i - \frac{\varphi_i}{x_i} \sum_j x_j l_j \quad (7)$$

$$\theta_i = \frac{x_i q_i}{\sum_j x_j q_j} \quad (8)$$

$$\varphi_i = \frac{x_i r_i}{\sum_j x_j r_j} \quad (9)$$

$$l_i = \frac{z}{2}(r_i - q_i) - (r_j - 1) \quad (10)$$

$$r_i = \frac{V_i}{V_{eff}} \quad (11)$$

$$q_i = \frac{A_i}{A_{eff}} \quad (12)$$

Where

y_i = Activity coefficient of component *i*

y_i^{SG} = Staverman-Guggenheim model for combinatorial contribution to γ_i

$\Gamma_s(\sigma_m)$ = Segment activity coefficient of segment σ_m in solvent mixture

$\ln \Gamma_i(\sigma_m)$ = Segment activity coefficient of segment σ_m in component *i*

$p_i(\sigma_m)$ = Sigma profile of component *i*

$p_i(\sigma_m)$ = Sigma profile of solvent mixture

σ = Surface charge density

$\Delta W(\sigma_m \sigma_n)$ = Exchange energy between segments σm and σn

$\Delta WHB(\sigma_m \sigma_n)$ Hydrogen bonding contribution to exchange energy between segments σm and σn

z = coordination number

V_i = molecular volume of component i

A_i = molecular surface area of component i

A_{eff} = standard segment surface area 7.50 Å^2

V_{eff} = Standard component volume, 66.69 Å^3

A_{eff} = Standard component surface area, 79.53 Å^2

α' = Misfit energy constant

Cosmo sac thermodynamic model requires only few general adjustable parameters which not dependent on temperature, and results in a good qualitative and quantitative predictions for the activity coefficients of ILs. Therefore, Cosmo sac is now readily being used as an efficient thermodynamic predictive model for the screening, selection, and design of processes based on ILs [26].

3. BASE CASE

The process schematic which contains the absorption tower & the stripper for the regeneration of solvent for the amine based technology is depicted in (Figure 1)

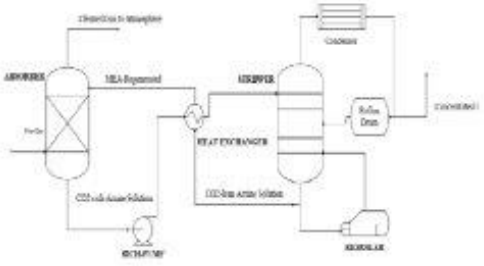

Figure 1 Base case for the removal of CO_2 using MDEA

The MEA based CO_2 capture methodology comprises of two essential fundamental units, the Absorption Column, in which the chemisorption of CO_2 takes place in MEA & the other fundamental unit comprises of the Regenerator Column, from the bottom of which lean solvent is obtained. In a typical scheme the CPP emission is cooled and is counter currently interacted with the Aqueous MEA solution in the absorber. The MEA chemically absorbs CO_2 & forms a reaction product (carbamate). The cleaned & treated gas is vented from the top of the absorber into the atmosphere. The bottom product of the absorption column is then directed through a process heat exchanger, and then into the regenerator in which heat is added to the CO_2 rich stream through reboiler using LP - steam. The products formed during the chemisorption process is thermally decomposed, consequently recovering the solvent as Lean MEA as bottom & a CO_2 enriched stream as the overhead product. The hot CO_2 laden solvent is then directed again to the heat exchanger, where its temperature is lowered down & routed to the absorption column for continuous operation. Due to the MEA loss some amount of MEA is added as Make – up to make sure the continuity of the operation.

3.1 Optimized case:

In this case, the Absorber operates under pressure (P=10 MPa) .The absorption column was simulated using Radfrac, and the equilibrium calculations were based on our experimental measurements using COSMO-SAC. The absorber pressure and IL circulation rate were optimized to maximize CO_2 recovery and minimize energy consumption. The inlet flue gas concentration was the same as the MEA base case. The IL used in this case belongs to the Pyridinium class of the ILs Enters the absorption column and flowed counter-current to the flue gas. The treated gas is vented from the top of the column and, because of the very low vapor pressure for

the IL, a secondary scrubber (i.e., wash-water section) to remove traces of IL from the vent is not required. The CO_2 concentration in the vent stream is reduced to the same concentration as in the MEA scrubbing system. The IL-absorption column was modelled using 10 theoretical stages.

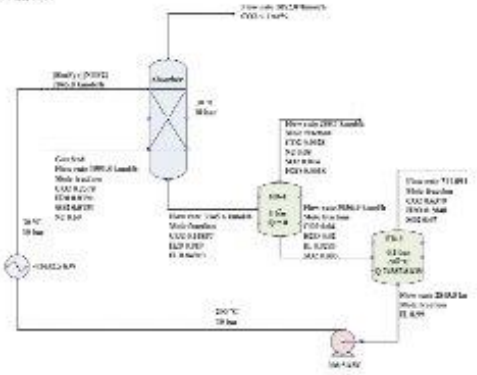

Figure 2 ionic liquid based process for the removal of CO_2

4. RESULTS AND ANALYSIS:

4.1. Effect of absorption column stages on L/F ratio

Since the ionic liquids are expensive so, optimum L/F ratio is required at fixed number of stages (10) found to be 3.6. The column operated at 10 bar pressure. Similarly for (Bmpyr)(NTF2), 14 stages are required for maximum removal (>97%) of CO_2 with L/F ratio of 3.8 as shown in figure 3. More than 99% CO_2 is removed from the bottom stream of the absorption column. Solvent stream is allowed to enter the flash drum, where pressure of the IL-rich stream is reduced to 1 bar for recovery of further CO_2 contents remaining in the following stream. The IL-stream is then discharged to second drum for stripping of acid gas from IL at reduced pressure up to 0.1 bar, temperature is increased to remove the water from IL. The IL is again recycled back to the absorption column by increasing its pressure 10 bar.

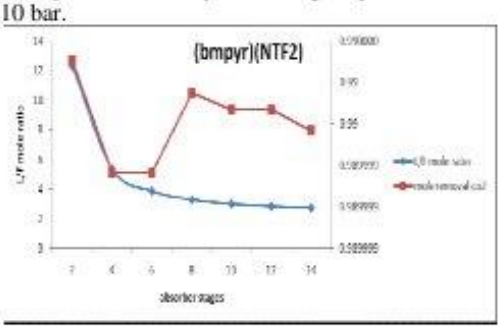

Figure 3 effect of number of theoretical on liquid to feed (L/F) ratio and removal of CO_2

4.2. Effect of pressure & temperature on removal

Sensitivity analysis on flash drum is carried out at varying pressure and temperature conditions to reduce the energy requirement of the system. Figure 4 shows the effect of pressure on the removal of gases based on FD-2 liquid stream. Despite the higher boiling range of IL, under vacuum conditions it is ready to lose some contents that must be considered while process evaluation. However, flash column is operated at 0.1 bar to maximize the solvent regeneration where, most of the gases separated. The flash drum has kept with duty zero to assess the maximum removal of gases. Since the IL is very expensive so the maximum recovery is needed

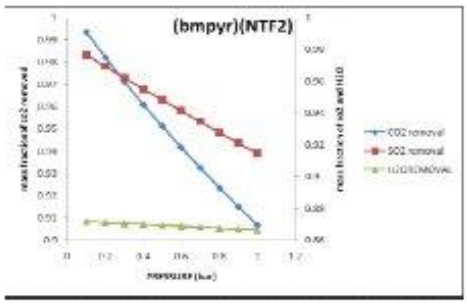

Figure 4 effect of pressure on CO_2 removal

After passing through the second flash, most of the IL is recovered According to the process there is no waste of IL as column running at 0.1 bar. At the elevated temperature, duty increases rapidly in order to satisfy the process requirements i.e. complete removal of acid gas from IL stream. At 200 °C almost complete water is removed

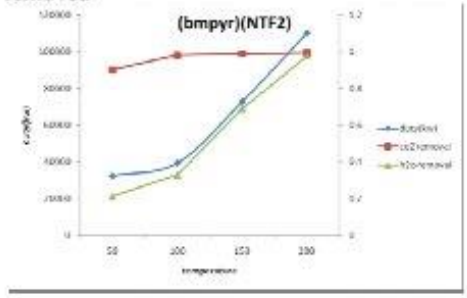

Figure 5 effect of temperature on CO_2 removal

5. CONCLUSION:

In future, the governments may continue to impose increasingly stringent requirements for reducing emissions of greenhouse gases. Thus, work aimed at providing an energy effective way of capturing greenhouse gases and for the treatment of flue gas , which is reflected by our analysis done using an industrially used software, ASPEN PLUS by providing Ionic liquids as a promising potential solvent as substitute against the Amines.

6. FUTURE RECOMMENDATION

Since the Ionic Liquids are expensive, so a blend of Amines with IL can be used which could be more economically feasible for both Acid gas absorption & CO_2 capture from CPP's, which could eventually result in the more efficient technological innovation towards a healthier & greener environment.

7. ACKNOWLEDGMENT

We are thankful to prof dr victor ferro from Universidad Autónoma de Madrid for providing us the technical support in terms of the cosmosac parameters and able to utilize them on the process simulator scale.

8. REFERENCES

[1] G.T. Rochelle, Amine Scrubbing for COCapture, Science (80) 325 (2009)

[2] M. Taheri, C. Dai, Z. Lei, CO_2capture by methanol, ionic liquid, and their binary mixtures: Experiments, modeling, and process simulation, *AIChE J.* (2018).

[3] M.A. Khan, M.Z. Khan, K. Zaman, M.M. Khan, H. Zahoor, RETRACTED: Causal links between greenhouse gas emissions, economic growth and energy consumption in Pakistan: A fatal disorder of society, *Renew. Sustain. Energy Rev.* 25 166–176. (2013)

[4] P. Changes, South Asia ' s Hotspots, 2018.

[5] united nations enviroment program, the enviroment and climate change outlook of pakistan, 2013.

[6] M.H. Alvi, Impact of Financial Development, Economic Growth and Energy Consumption On Environmental Degradation:

Evidence from Pakistan, (2010).

[7] Z. Mustafa, Climate Change and Its Impact With Special Focus in Pakistan, Symp. "Changing Environ. Pattern Its Impact with Spec. Focus Pakistan." (2011).

[8] C. Kale, A. Górak, H. Schoenmakers, Modelling of the reactive absorption of CO_2 using mono-ethanolamine, *Int. J. Greenh. Gas Control.* 17 (2013) 294–308.

[9] M. Hasib-ur-Rahman, M. Siaj, F. Larachi, Ionic liquids for CO_2 capture—Development and progress, *Chem. Eng. Process. Process Intensif.* 49 (2010) 313–322.

[10] L. Zhu, G.W. Schade, C.J. Nielsen, Real-Time Monitoring of Emissions from Monoethanolamine-Based Industrial Scale Carbon Capture Facilities, *Environ. Sci. Technol.* 47 (2013) 14306–14314..

[11] C. Cadena, J.L. Anthony, J.K. Shah, T.I. Morrow, J.F. Brennecke, E.J. Maginn, Why is CO_2 so Soluble in Imidazolium-Based Ionic Liquids, *J. Am. Chem. Soc.* (2004).

[12] V.C.A. Ward, G. Munch, N. Cicek, L. Rehmann, Direct Conversion of the Oleaginous Yeast Rhodosporidium diobovatum to Biodiesel Using the Ionic Liquid [C2mim][EtSO4], *ACS Sustain. Chem. Eng.* (2017).

[13] A. Vollas, T. Chouliaras, V. Deimede, T. Ioannides, J. Kallitsis, A. Vollas, T. Chouliaras, V. Deimede, T. Ioannides, J. Kallitsis, New Pyridinium Type Poly(Ionic Liquids) as Membranes for CO_2 Separation, Polymers (Basel). 10 (2018) 912.

[14] P. Kilaru, G.A. Baker, P. Scovazzo, Density and Surface Tension Measurements of Imidazolium-, Quaternary Phosphonium-, and Ammonium-Based Room-Temperature Ionic Liquids: Data and Correlations, *J. Chem. Eng. Data.* 52 (2007) 2306–2314.

[15] L.A. Blanchard, Z. Gu, J.F. Brennecke, High-Pressure Phase Behavior of Ionic Liquid/CO_2 Systems, *J. Phys. Chem. B.* (2001).

[16] Á.P.S. Kamps, D. Tuma, J. Xia, G. Maurer, Solubility of CO_2in the ionic liquid [bmim][PF6], *J. Chem. Eng. Data.* (2003).

[17] H. Sakhaeinia, V. Taghikhani, A.H. Jalili, A. Mehdizadeh, A.A. Safekordi, Solubility of H2S in 1-(2-hydroxyethyl)-3-methylimidazolium ionic liquids with different anions, *Fluid Phase Equilib.* (2010).

[18] S. Zeng, X. Zhang, L. Bai, X. Zhang, H. Wang, J. Wang, D. Bao, M. Li, X. Liu, S. Zhang, Ionic-Liquid-Based CO_2 Capture Systems: Structure, Interaction and Process, *Chem. Rev.* (2017).

[19] J. Kumełan, Á. Pérez-Salado Kamps, D. Tuma, G. Maurer, Solubility of CO_2 in the ionic liquid [hmim][Tf2N], *J. Chem. Thermodyn.* 38 (2006) 1396–1401.

[20] Y. Ma, J. Gao, Y. Wang, J. Hu, P. Cui, Ionic liquid-based CO_2 capture in power plants for low carbon emissions, *Int. J. Greenh. Gas Control*. (2018).

[21] V.R. Ferro, J. de Riva, D. Sanchez, E. Ruiz, J. Palomar, Conceptual design of unit operations to separate aromatic hydrocarbons from naphtha using ionic liquids. COSMO-based process simulations with multi-component "real" mixture feed, *Chem. Eng. Res. Des.* (2015).

[22] V.R. Ferro, C. Moya, D. Moreno, R. Santiago, J. De Riva, G. Pedrosa, M. Larriba, I. Diaz, J. Palomar, Enterprise Ionic Liquids Database (ILUAM) for Use in Aspen ONE Programs Suite with COSMO-Based

Property Methods, *Ind. Eng. Chem. Res.* (2018).

[22] T. Zhou, Z. Qi, Model-based method for the screening of solvents for chemical reactions, *Chem. Eng. Sci.* 115 (2014) 177–185.

[23] R. Fingerhut, W.-L. Chen, A. Schedemann, W. Cordes, J. Rarey, C.-M. Hsieh, J. Vrabec, S.-T. Lin, Comprehensive Assessment of COSMO-SAC Models for Predictions of Fluid-Phase Equilibria, *Ind. Eng. Chem. Res.* 56 (2017) 9868–9884.

[24] N.D. Austin, N. V. Sahinidis, D.W. Trahan, A COSMO-based approach to computer-aided mixture design, *Chem. Eng. Sci.* 159 (2017) 93–105.

[25] Z. Xue, T. Mu, J. Gmehling, Comparison of the a Priori COSMO-RS Models and Group Contribution Methods: Original UNIFAC, Modified UNIFAC(Do), and Modified UNIFAC(Do) Consortium, *Ind. Eng. Chem. Res.* 51 (2012) 11809–11817.

[26] R. Xiong, S.I. Sandler, R.I. Burnett, An Improvement to COSMO-SAC for Predicting Thermodynamic Properties, *Ind. Eng. Chem. Res.* 53 (2014) 8265–8278.

SIMULATION & MODELLING OF LNG INTEGRATED AIR SEPARATION PROCESS

Muhammad Naqi Raza[1*], Zahoor-ul-Hussain[1], Saud Hashmi[2]

[1]Department of Chemical Engineering NED University of Engineering & Technology Karachi.

[2]Department of Polymer & Petrochemical Engineering NED University of Engineering & Technology Karachi.

Corresponding author: Tel. +923463275830

E-mail address: naqiraza65@gmail.com

ABSTRACT:

Liquefaction and Separation of Air requires a huge amount of energy due to air compression and expansion of nitrogen after re-compression. The Cost of products (Oxygen, Nitrogen etc) depends upon the required purity and specific power of plant. Specific power is the ratio of power consumed to unit product produced. For liquefaction, compressed Nitrogen is cooled down to desired temperature by Joules Thompson (J-T) Effect. The J-T effect is produced by re-compression of nitrogen to high pressure and its expansion to low pressure. The re-compression of nitrogen requires a huge amount of energy which increases the overall cost of the process. This paper propose LNG (Liquefied Natural Gas) Integrated Air Separation process. The purpose of integration is regasification of LNG while extracting its large amount of cold energy and exchanging it with compressed Nitrogen for its liquefaction which in later stage cool down the compressed air. The whole process while considering all the safety aspects is simulated on ASPEN PLUS. The theoretical results from the simulation are impressive in terms of specific power (0.673 KWh/Nm^3) and as product LO_x purity (>99.7 %).

Keywords: Air Separation Process, Specific Power, LNG

INTRODUCTION

In order to transport reserves of remote natural gas into the network and long distance supply, transporting natural gas in liquefied form become the most cost-effective and appropriate solution [1, 2]. LNG is transported at -162 ^{0}C and slightly above atmospheric pressure on the vessel called LNG carrier [1]. 478 LNG carriers

were in activity at the end of 2017 [1]. Typically, at the end of the LNG supply chain consumer require the LNG to be converted back to gas state. Almost for per ton of LNG 240 KWh cold energy is fruitless during regasification process [3]. Natural gas accounts to one quarter of the global energy demand, of which approximately 10% supplied as liquefied natural gas [1, 2]. Japan, China and South Korea has the biggest market share for import of LNG in world by 28.8%, 13.5% and 13.2% respectively [1]. While Pakistan has market share of 1.7% with nominal regasification capacity of 10 MT but utilizing only 54% [1].

In theoretical aspects, air separation is the lone process that could completely recover LNG cold energy on the available temperature range during regasification. Traditional ASU cold boxes for nitrogen liquefaction involve temperature down to about -190 ^{0}C.

Numerous configurations have been studied by different researchers for integration of LNG regasification to conventional Air separation process or novel air separation process. XU et al [4] make comparison of traditional LNG integration in ASU with their suggested novel scheme and found energy efficiency up to 66% by the increase of 28%. Maximum operating pressure of system reduced from 2.6 MPa to 1.5 Mpa. At the same interval column pressure also reduce from 0.5 Mpa to 0.35 Mpa. Power consumption also reduced from 0.358 KWh/kg to 0.313 KWh/kg. But in traditional unit inlet temperature for nitrogen compressor is -83 ^{0}C and in novel one air, nitrogen and LNG are in same exchanger this may be safety hazard.

Tesch et al [5] make exergy analysis of the LNG integrated ASP and compare two designs and found energy efficiency of 64% for design 2 as compare to design 1 efficiency of 58% with LNG pressure of 120 bar. While with LNG pressure of 20 bar found energy efficiency of 53% for design 2 as compare to 49% for design 1. In this work they neglect safety aspects by using LNG in intercoolers of compressors and also use with air in main heat exchanger.

Ebrahimi et al [6] evaluate LNG integrated ASU by thermodynamic and economic while also make pinch analysis of main heat exchangers. In this paper they also neglect safety aspects and use LNG and air in same exchanger

Chao Fu et al [7] perform the exergy analysis for the double column distillation column. Theoretical specific power consumption was 0.049 KWH/kg, while the actual power consumption was around 4.7 times the theoretical minimum. A 19% reduction in specific power consumption

could achieve if isentropic efficiency of compressor increased from 0.74 to 0.9.

Tesch et al: [8] make exergetic and economic evaluation of four LNG integrated ASU. Two units with nitrogen liquefaction block while remaining two are without nitrogen liquefaction block. Safety related concepts are considered in two units while remaining two are without safety aspects. While economic analysis found that system with safety concept is 9% more expensive. In this work all products are low purity except LN in two cases with nitrogen liquefaction block.

It is found from literature review that maximum researchers [4, 5, 6, 7, 8] neglect safety aspects of plant and there only focus is product recovery. Due to market, there are different needs for different locations. Safety aspects considering in [8] also has low purity of products. This research focus is to study the LNG integrated ASU of with LO_x as a product with considering safety aspects.

PARAMETERS SELECTION

The standard pointer to estimate ASU design is the power consumption per amount of liquid oxygen or nitrogen produced. As the quantity of product recovered is based on the flow rate of feed air and refrigeration from refrigeration unit or LNG feed, both the feed air and the LNG feed characteristics must be fixed for simulated cases and reported in Table 1 & 2 respectively. Purity and specifications of products of simulated model in research work are shown in Table 3. Outlet conditions from purification block reported in Table 4.

Table 1: Air Composition

Components	**Mole Fraction**
Nitrogen	0.772
Oxygen	0.208
Argon	0.0095
Carbon Dioxide	0.0003
Water	0.0102
Air Flow	6600 Nm^3/hr

Table 2: LNG Composition

Composition	**Mole Fraction**
Methane	0.8698
Ethane	0.0935
Propane	0.0233
Butane	0.0063
Nitrogen	0.0071

Table 3: Products Purity & Specifications

Products	**LO_x**
Pressure	120 KPa
Temperature	-180.5 ^0C
Purity	>99.7

Table 4: Outlet Conditions of Purification Stage

Parameter	
Temperature	10^0C
Air Composition	Free From Contaminants CO_2, H_2O, SO_2

PROCESS SIMULATION

ASPEN PLUS is well known simulation software. It is was used for simulation and modelling due to good. The equation of state selected was Peng-Robinson [8].

$$P = \frac{RT}{(c+V_m)-b} - \frac{a}{(V_m+c)(V_m+c+b)+b(V_m+c-b)}$$

Air enters at ambient conditions T=25 ^{0}C and P=1.013 bar. LNG is fed to the system with a pressure $P_{LNG,in}$ = 5 bar and a temperature of $T_{LNG,in}$ = -162 ^{0}C. A simulated case of LNG regasification integrated in Air Separation process studied in this research work.

Process Description

Air separation unit consist of four blocks:

1) Compression & Purification
2) Main heat exchanger
3) Column
4) Refrigeration block

Air with ambient conditions enter into three stage compression block where it is compress up to 5.6 bar pressure. To reduce power consumption due to high specific volume, compressor unit consist of intercoolers. Finally, air discharge from after cooler at pressure of 5.6 bar with temperature 40 ^{0}C enters into purification block.

Purification block consist of air pre-cooling unit decrease the temperature of incoming air upto 10 ^{0}C results in condensation of moisture content. Another part of purification block is absorbers. There are two absorbers one is in action while another is in regeneration step. Absorber remove contaminants of feed air like CO_2, SO_2, etc.

After purification block air enters into main heat exchanger where its temperature is reduce up to -173 ^{0}C by waste nitrogen from top column and recycle nitrogen from high pressure column. Then air enters into HPC of column block.

Column block has two sections high pressure column and low pressure column. Both column are interconnected by evaporator/condenser, an exchanger, evaporator for low pressure column and condenser for high pressure column. Air enters into high pressure column, distillate

is pure nitrogen while bottom product known as Rich Liquid has >35% O_2 and <65% N_2. RL enters into LPC where it separates into LO_x and waste nitrogen. Distillate is waste nitrogen and bottom product is LO_x.

Another important part is Refrigeration block. This is main source for providing cooling to system. This consist of Nitrogen recycle compressor, booster/turbine, nitrogen chiller and heat exchanger. In this nitrogen from HPC after transferring cooling to feed air enter into NRC and after further compression in booster its pressure increases up to 30 bar. Approximately 80% of recycle nitrogen enters turbine and after expansion transferring cooling to remaining 20% flow of recycle nitrogen. This 20% recycle nitrogen enters into HPC as a reflux.

In LNG integrated system booster/turbine and nitrogen chiller are completely vanished due to cooling transfer by LNG, results in reduction of capital up to appreciable extent.

While another side this integration reduce power consumption of Nitrogen recycle compressor. Fig 1 is simulated case of LNG integrated Air Separation unit.

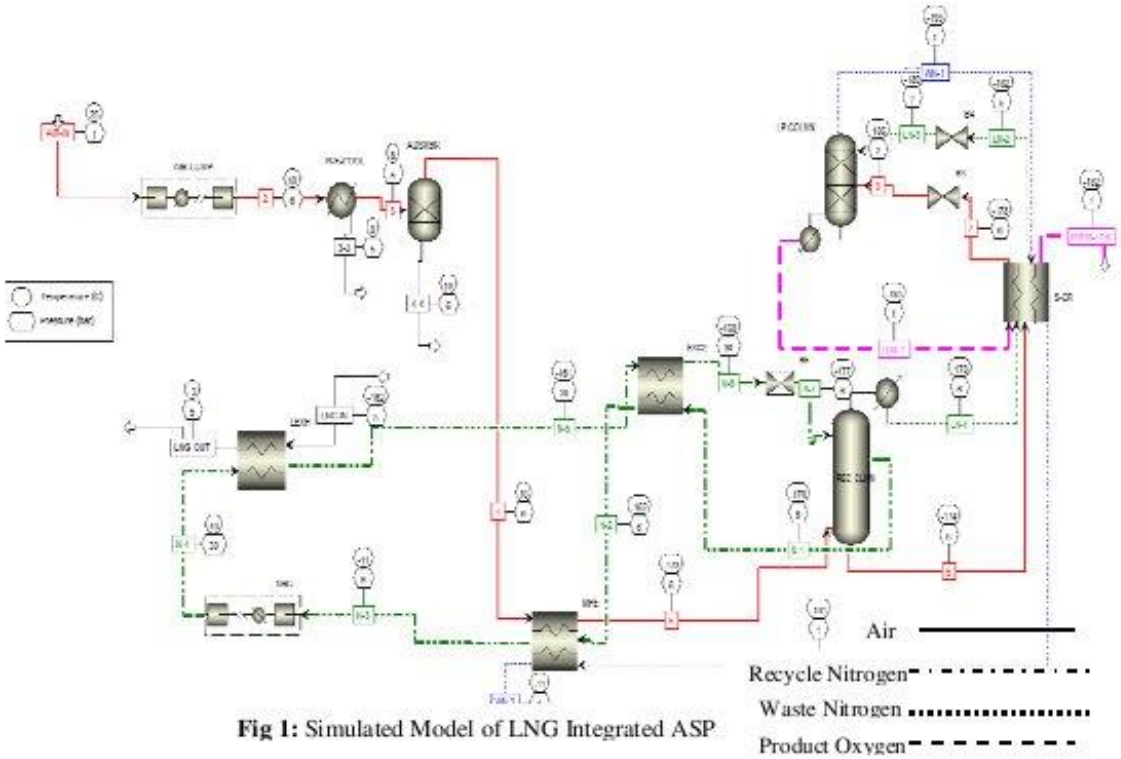

Fig 1: Simulated Model of LNG Integrated ASP

RESULTS AND DISCUSSION

Simulation Result of LNG Integrated Air Separation Unit

As discussed in process description booster/turbine and N_2 Chiller are completely vanished in LNG integrated unit while power consumption of NRC reduced due to this integration. Table 5 & 6 show physical properties and composition of stream. According to Table is clear that after integration with LNG almost all the useful cold energy of this stream will be transferred to recycle nitrogen of ASU and its temperature will reduce from 40 to -162C. Fig: 2 show composition of RL in Low pressure column as reported in process description it must be consist of >35% oxygen.

Table 5: Streams Result of REC-Column

		1/AIR	5/FEED-AIR	6/RL	LN-1	N-1
Temperature	^0C	25	-173	-173.8	-177.8	-177.8
Pressure	Bar	1	5	5.5	5.5	5.5
Vapor Fraction		1	1	0	0	1
Mole Flow	Nm^3/hr	6600	6468	3500	2968	2230
Mass Flow	kg/hr	8498	8328	4618	3709	2787
Enthalpy	Watt	-212100	-484130	-494210	-405530	-171260
Mole Flow	Nm^3/hr					
N_2		5095	5095	2127	2968	2230
O_2		1373	1373	1373	0	0
Ar		63				
Mole Fraction						
N_2		0.772	0.788	0.608	1	1
O_2		0.208	0.212	0.392	3 PPM	3 PPM
Ar		0.009				

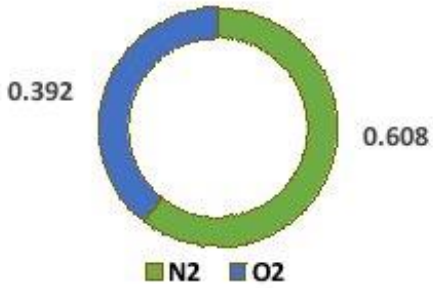

Fig 2: Components Mole Fraction in Rich Liquid

Table 6: Streams Result of LP-Column

		LO_X-1 / LO_X	**LN-3 / REF-IN**	**WN-1 / WASTE-N_2**	**PROD-LO_X**
Temperature	°C	-180	-191.6	-192.7	-182
Pressure	Bar	1.4	2	1.4	1.4
Vapor Fraction		0	0.082	1	0
Mole Flow	Nm^3/hr	1354	2968	5114	1354
Mass Flow	kg/hr	1933	3709	6395	1933
Enthalpy	Watt	-213280	-415140	-407140	-215080
Mole Flow	Nm^3/hr				
N_2		0	2968	5095	0
O_2		1354	0	19	1354
Mole Fraction					
N_2		trace	1	0.994	trace
O_2		1	10 PPM	0.006	1

consumed to unit product produce. Total power consumption and specific power of

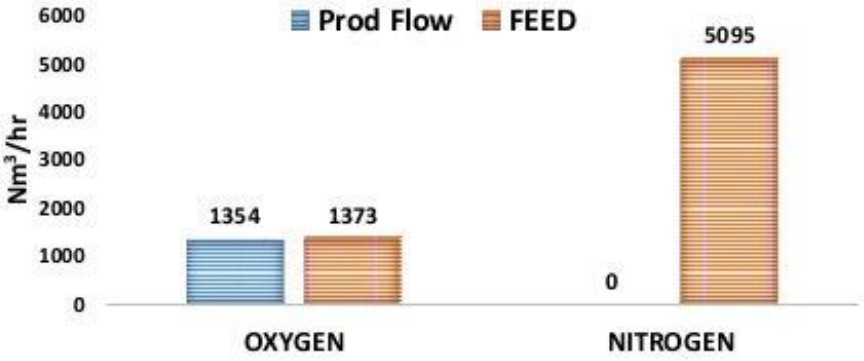

Fig 3: Feed/Production Of Components

Fig: 3 show comparison of feed air oxygen flow and product oxygen flow. Almost 99% of oxygen recovered [Fig: 5] with both units reported in Table 7. LNG integrated system is most power efficient as compare to conventional unit due to

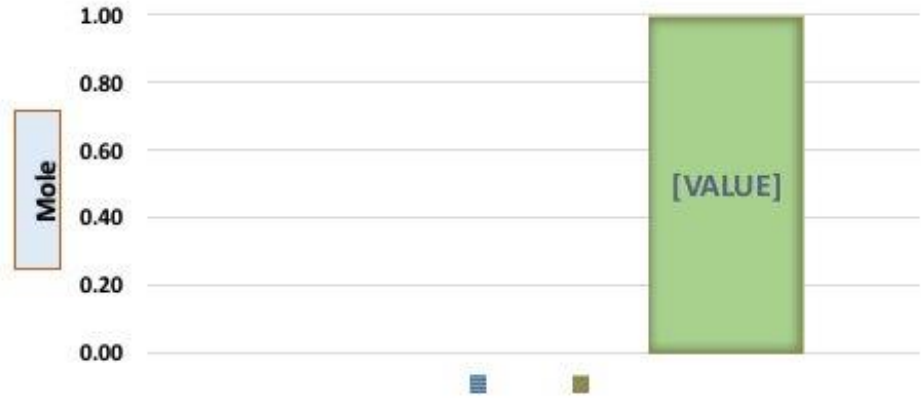

Fig 4: Product Composition

mole fraction of 1 in LO_x product [Fig: 4].

Power Consumption

Classic parameter to estimate the efficiency of the unit is specific power of plant. Specific power is ratio of power NRC power consumption As reported in Fig: 6 & 7, main Components in ASU, consume maximum power are air compressor and nitrogen compressor. Almost 83% power is consumed by both

compressors in LNG integrated air separation unit. LNG integration outcomes in reduction of NRC power consumption results in reduction of specific power of products.

Key source of refrigeration in conventional air separation unit is nitrogen recycle compressor and expander. While LNG integration results, decrease in power consumption of nitrogen recycle compressor.

Flow of NRC in conventional unit is up to

Table 7: Total Power Consumption KW-hr

EQUIPMENT NAME	LNG INTEGRATED ASP
Compressors/Expanders	753.00
Pumps	76.00
Refrigeration Unit	50
Cooling Tower	32
Total Power KW/hr	**911.00**
Specific Power KW-hr/Nm^3	**0.673**

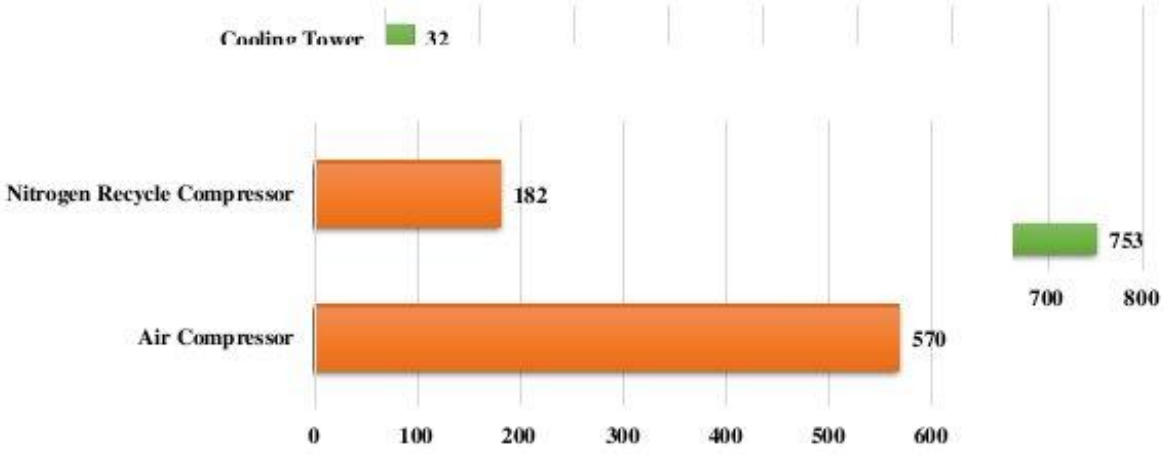

Fig 6: Compressors Power Consumption in kW

13900 Nm^3/hr while this flow reduces up to 2200 Nm^3/hr in LNG integrated unit.

Specific power of product reported in Fig 8. LNG integration simulated case results 0.673 KW-hr/Nm^3 specific power of product. Maximum reduction of power in LNG integrated unit is due to reduced flow of NRC

CONCLUSION

In this paper LNG integrated Air separation unit were simulated , studied and evaluated, It is cleared that power consumption and total capital investment for LNG integrated ASU is very low.

Key points of research work are:

1. Design of Sequence of Operation & Simulation with Considering safety aspects
2. High purity >99.7% LO_X Product
3. Specific Power of integrated unit is 0.673 KW-hr/Nm^3
4. Less capital investment

In future, work could be extended by economic analyses and comparative study with conventional air separation unit. While also could study the effect of adding by product of LN on specific power.

REFERENCES:

1. International Gas Union, World LNG report 2018 (2018) [cited December 26, 2018]. URL http://www.igu.org/publications/2018-world-lng-report

2. BP, BP Energy Outlook - 2018 edition: Outlook to 2040 (2018) [cited 02 January, 2019]. URL www.bp-energy-outlook-2018.pdf

3. Liu H, You L. Characteristics And Applications Of The Cold Heat Exergy Of Liquefied Natural Gas. Energy Convers Manage 1999;40:1515–25.

4. Process Study and Exergy Analysis of a Novel Air Separation Process Cooled by LNG Cold Energy XU Wendong, DUAN Jiao1, MAO Wenjun DOI: 10.1007/s11630-014-0679-5

5. Advanced exergy analysis applied to the process of regasification of LNG (liquefied natural gas) integrated into an air separation process Stefanie Tesch, Tatiana Morosuk, George Tsatsaronis

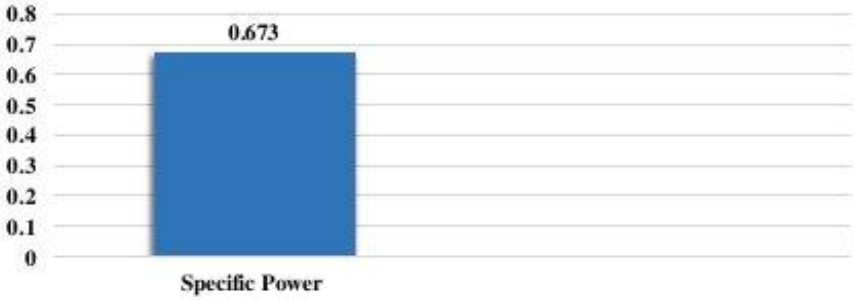

Fig 8: Specific Power kW-hr/Nm^3

http://dx.doi.org/10.1016/j.energy.2016.04.031 58

6. Optimal design and integration of a cryogenic Air Separation Unit (ASU) with Liquefied Natural Gas (LNG) as heat sink, thermodynamic and economic analyses Armin Ebrahimi, Masoud Ziabasharhagh http://dx.doi.org/10.1016/j.energy.2017.02.145

7. Fu C, Gundersen T. Using exergy analysis to reduce power consumption in air separation units for oxy-combustion processes. Energy 2012;44:60e8.

8. Exergetic and economic evaluation of safety-related concepts for the regasification of LNG integrated into air separation Stefanie Tesch, Tatiana Morosuk, George Tsatsaronis 10.1016/j.energy.2017.04.043

FLOW AND HEAT TRANSFER CHARACTERISTICS OF MICROCHANNEL HEAT SINK WITH CYLINDRICAL RIBS AND CAVITIES

Faraz Ahmad, Taqi Ahmad Cheema*, M. Mohib Ur Rehman
Faculty of Mechanical Engineering, Ghulam Ishaq Khan Institute of Engineering Sciences and Technology, Swabi, KPK, Pakistan.

*Corresponding author: *Tel.:* +92-938-271858; *Fax:* +92-938-281000;
E-mail: tacheema@giki.edu.pk ; taqi_cheema39@hotmail.com

ABSTRACT

Microchannel Heat Sink (MCHS) with different configurations of cylindrical ribs and cavities are simulated to investigate the effect of ribs on base wall, side wall and all walls on flow and thermal characteristics of MCHS. The case of all wall ribs is compared with the case of all wall cavities and the mixture of both ribs and cavities. Furthermore, the effects of staggered rib configuration and stream wise spacing between ribs (S_r) are investigated for the case of all wall ribs. The hydraulic characteristics of various microchannels is compared with each other and smooth channel in terms of friction factor (f). However, the thermal characteristics are quantified in terms of Nusselt number (Nu). Moreover, the overall performance of various configurations is compared with the smooth channel in terms of thermal enhancement factor (η). The study has been simulated over a Reynolds number (Re) ranging from 100 to 1000. The maximum Nu achieved is 19.6 for the case of all wall ribs (S_r = 0.4 mm) with a friction factor of 1.8 at Re = 1000. Moreover, the maximum η achieved is 1.02 for the case of side wall ribs at Re= 100.

Keywords: Microchannel heat sink, Ribs, Cavities, Nusselt number, Friction factor, Thermal enhancement factor.

1 INTRODUCTION

Conventional air cooling technologies are inadequate to dissipate the large quantity of heat flux generated in modern electronic systems because of its miniaturization. An alternative technique to conventional cooling methods, the idea of microchannel heat sink (MCHS) was therefore presented in 1981 by Tuckerman and Pease [1], which was capable of dissipating 7.9×10^6 W/m^2. It was proved by Hongqi et al. [2] that MCHS can dissipate heat in a better way because of increase in effective cooling area.

A lot of research has been dedicated to investigate the performance parameters of MCHS and provide a better cooling technology to the modern world. These techniques include alteration in geometry of the channel [3] and the disruption of flow through various modifications at wall surface like installing ribs, cavities and grooves etc. [4]. Many experimental and numerical studies in the literature are dedicated to investigate the effect of such modifications like cavities and ribs on the thermal and hydraulic characteristics of MCHS [5-9]. For instance, Wang et al. [10] introduced micro scale ribs on the heated walls of MCHS. They investigated numerically and experimentally the effect of different relative rib heights on MCHS. They proposed that increase in relative rib height increases the Nusselt number of rib-grooved MCHS, because it involves more fluid in mixing. The thermal enhancement factor in this study was less than unity, because the heat transfer was unable to offset the pressure drop. Moreover, Khan et al. [11] numerically investigated various configurations of ribs in MCHS with fixed width and length of rib in a Reynolds number ranging from 100 to 500.

Furthermore, Xia et al. [12] numerically investigated the characteristics of MCHS with reentrant cavities of triangular shape. They reported that the formation of vortices can greatly enhance the

fluid mixing. This study found that the complex geometry enhances the heat transfer not only because of the vortex formation, but may also be due to the interruption of boundary layers.

Apart from the above mentioned studies, some researchers combined the ribs and cavities to investigate their effects on thermal and hydraulic characteristics of MCHS. For example, Ghani et al. [13] introduced sinusoidal cavities between rectangular ribs, and numerically investigated their effects on the performance of MCHS. They showed that combining ribs and cavities led to a higher thermal enhancement factor, because the larger pressure drop can be compensated by cavities. Furthermore, Li et al. [14] numerically investigated the effect of different geometric configurations of fins and cavities on the thermal and hydraulic characteristics of MCHS. They reported that the influence of fin is more than the shape of cavity on hydraulic and thermal performance of MCHS.

Although the above alterations and modifications improve the heat transfer characteristics, however at the same time, the frictional losses also increases due to which power consumption increases. A criteria is therefore need to be defined to assess the design of ribs in the channel in terms of both frictional and heat transfer losses. In this regard, Webb [15] proposed the concept of performance evaluation criteria (PEC), which can also be called as thermal enhancement factor (η).

The present study aims to conduct numerical simulations to compare the effect of ribs on base, side, and all walls of MCHS. Moreover, the effect of staggered condition of ribs and stream wise spacing (S_r) on flow and thermal characteristics in terms of friction factor (f), Nusselt number (Nu) and thermal enhancement factor (η) has been investigated.

2 MATERIALS AND METHODS

2.1 Computational domain

A rectangular channel is considered as the computational domain in the present study, because its thermal resistance is lower than that of trapezoidal and triangular channels as reported by Wang et al. [3]. The computational domain of smooth microchannel is shown in Fig. 1.

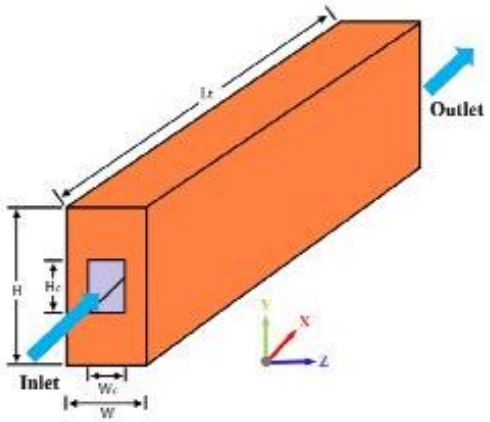

Fig. 1 Computational domain of smooth channel

Moreover, the geometric parameters are given in Table 1 and the constant thermo-physical properties of the materials for fluid (water) and solid (copper) domain are provided in Table 2. The ribs are mounted at the centerline of each wall of the microchannel as shown in Fig. 2. The shape of cavity is exactly same as that of rib. The stream wise spacing between the consecutive ribs (S_r) is varied from 0.4 to 1.2mm.

Table 1 Geometric parameters

Parameters	L_r	H	W	H_c	W_c	D_r	H_r	S_r
Values (mm)	10	1.5	0.6	0.5	0.35	0.2	0.1	0.4, 0.8, 1.2

Table 2 Thermo-physical properties of materials

Materials	ρ (kg/m^3)	Cp $(J/kg/K)$	k $(W/m/K)$	μ $(kg/m/sec)$
Copper	8978	381	387.6	
Water	998.2	4182	0.6	0.001003

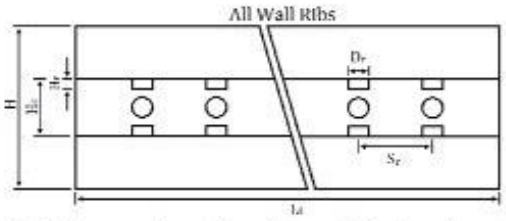

Fig. 2 Geometric configurations of ribs (x-y plane)

2.2 Governing equations

Constant thermo-physical properties for Newtonian fluid is considered assuming that the flow is laminar, steady and incompressible. The effects of body forces and radiation heat transfer are neglected. Considering the above assumptions, the equations of momentum, continuity and energy for fluid and solid domain can be written as:

$$(u \cdot \nabla)u = -\frac{\nabla p}{\rho} + \frac{\mu}{\rho}\nabla^2 u \quad (1)$$

$$\nabla \cdot (\rho u) = 0 \quad (2)$$

$$u \cdot \nabla T_f = \frac{k_f}{\rho C_p}\nabla^2 T_f \quad (3)$$

$$k_s \nabla^2 T_s = 0 \quad (4)$$

Where μ, ρ and k_f are the dynamic viscosity, density and thermal conductivity of the working fluid (water), and k_s is the thermal conductivity of the solid domain (Copper).

The applied boundary conditions to solve the above governing equations are as follows:

At inlet surface ($x = 0\ mm$):

$$u = u_{in}; T_f = T_{in} \quad (5)$$

Where $T_{in} = 293.15\ K$ and u_{in} is the uniform inlet velocity that can be calculated from Re which is ranging from 100 to 1000 in the present study.

At outlet surface ($x = 10\ mm$):

$$p = p_{out} = 1\ atm \quad (6)$$

No slip condition is given at the inner wall of the channel.

$$u = v = w = 0 \quad (7)$$

At the bottom surface ($y = 0$):

$$-k_s \frac{\partial T_s}{\partial y} = q_w = 100\ W/cm^2 \quad (8)$$

Adiabatic boundary condition is applied at the remaining surfaces.

$$\frac{\partial T_f}{\partial x} = \frac{\partial T_s}{\partial x} = 0 \quad (9)$$

2.3 Mesh independence test

FLUENT 15.0 is used to conduct numerical simulations with the convergence criteria set to be less than 10^{-6} for all the variables. A Hex Dominant mesh is used to discretize the ribs in fluid domain as shown in Fig. 3. To check the reliability of the solution, a mesh independence test is performed for the case of all wall ribs (S_r = 0.4mm) with grid numbers ranging from 533693 to 1090950 at Reynolds number 300.

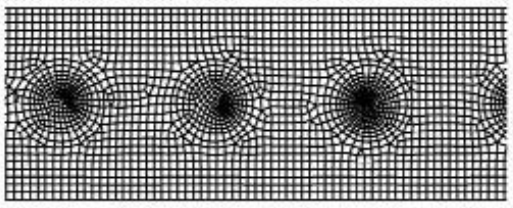

Fig. 3 Mesh structure showing the discretization of ribs in fluid domain (x-y plane)

The relative error for any parameter (M) between the finest grid (M_1) and other grids (M_2) is calculated by the following equation;

$$E\% = \left|\frac{M_2 - M_1}{M_1}\right| \times 100 \quad (10)$$

Where M stands for any parameter, such as pressure drop, Nusselt number etc.

Table 3 Mesh independence test

No. of Mesh	No. of elements	Δp	E%	Nu	E%
1	533693	13602	6.76	13.15	4.53
2	633500	13985	4.14	12.9	2.54
3	740566	14688	0.67	12.55	0.23
4	864545	14625	0.24	12.56	0.15
5	1090950	14590		12.58	

Table 3 presents the relative error for Nusselt number and pressure drop. As the number of elements increases above 0.6 million, the relative error becomes less than 1% for both the Nusselt number and pressure drop, so mesh 3 is the selected mesh for this study where number of elements and nodes are 740566 and 163553 respectively.

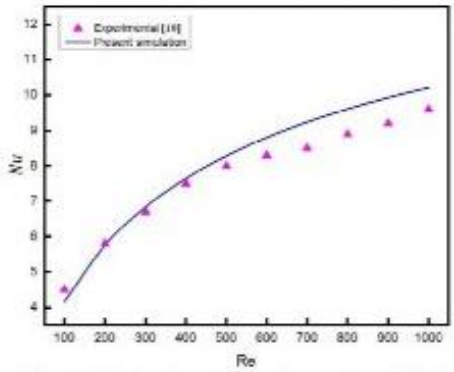

Fig. 4 Validation of Nusselt number with Ref. [7]

3 RESULTS AND DISCUSSIONS

3.1 Model validation

The Nusselt number computed from the present model is validated with the experimental work of Guilian et al. [10]. Fig. 4 shows that the experimental results are in good agreement with the present simulations, so the present model can be used to predict the thermal and hydraulic characteristics of MCHS.

3.2 Characteristics of velocity and pressure distribution

Fig. 5 shows the pressure and velocity distribution for different MCHS with different configuration of ribs. The left side of Fig. 5 shows the pressure distribution in which all wall ribs having rib spacing 0.4 mm witnessed the maximum pressure drop because the small spacing between the ribs means more number of ribs, thus leading to more blocking of flow. It is clear that the pressure drop increases with decrease in rib spacing because of the increasing non-uniformities in velocity distribution which leads to the interruption of velocity boundary layer.

The right side of Fig. 5 shows the non-uniformities in velocity distribution. It is obvious that the decrease in rib spacing (S_r) promotes the chaotic mixing due to which the non-uniformities in velocity increases. The increase in mixing promotes the heat transfer rate at the cost of increase in pressure drop which leads to more power requirement. The increase in power requirement can be reduced by introducing cavities of the same cross section between the ribs, because the presence of cavity reduces the blocking effect and provides more volume for fluid flow.

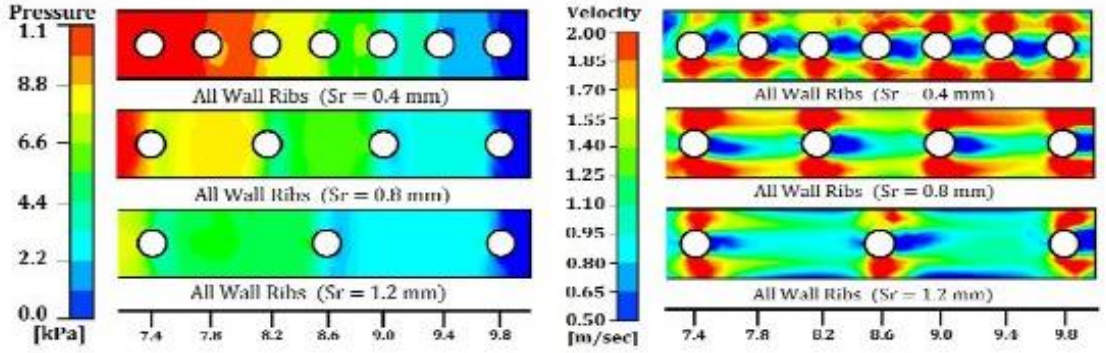

Fig. 5 Pressure and Velocity distribution (x-y plane) for different configuration of fins and cavities at z = 0.46 mm for *Re* = 300

3.3 Data reduction

The friction factor can be given as:

$$f = \frac{2D_h \Delta p}{L_t \rho_f u_m^2} \quad (13)$$

Nu can be calculated as:

$$Nu = \frac{hD_h}{k_f} \quad (14)$$

Where u_m, h and D_h are the mean velocity, heat transfer coefficient and hydraulic diameter respectively, and can be given as follows:

$$h = \frac{q_w A_{base}}{2(W_{ch}+H_{ch})L_t \Delta T} \quad (15)$$

$$D_h = \frac{2H_c W_c}{H_c+W_c} \quad (16)$$

Where q_w, A_{base} and ΔT are the heat flux, area of the base surface and average temperature difference between the inlet wall of the channel and the fluid respectively. L_t, W_{ch} and H_{ch} are the length, width and height of the channel respectively.

The expression for the thermal enhancement factor (η) can be expressed as follows:

$$\eta = \frac{Nu/Nu_0}{\sqrt[3]{f/f_0}} \quad (17)$$

Where Nu_0 and f_0 are the Nusselt number and friction factor of smooth microchannel respectively.

The variation of friction factor with Reynolds number is shown in Fig. 7. The smooth channel has the lowest friction factor because of the absence of any blocking effect. Fig. 7 (a) shows that the friction factor of MCHS with ribs on all walls is more than that of side walls and base walls, because of maximum non uniformities and mixing. Moreover, the friction factor increases as the spacing between the consecutive ribs decreases as shown in Fig. 7 (b). The friction factor for offset condition is more than aligned condition for $Re < 400$, but for the $Re > 400$, the friction factor for offset condition becomes less than that of aligned condition. Fig. 7 (c) shows that the friction factor of cavity is far less than ribs (S_r = 0.4mm), thus introducing cavities between ribs reduces the friction factor of MCHS with all wall ribs.

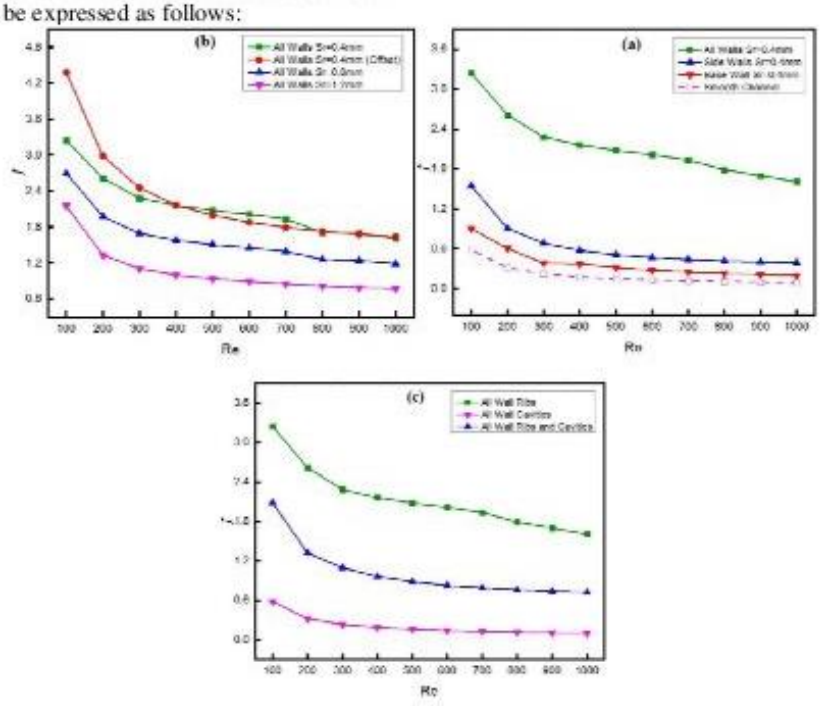

Fig. 7 Effect of Reynolds number on friction factor (f), for various configurations of ribs and cavities

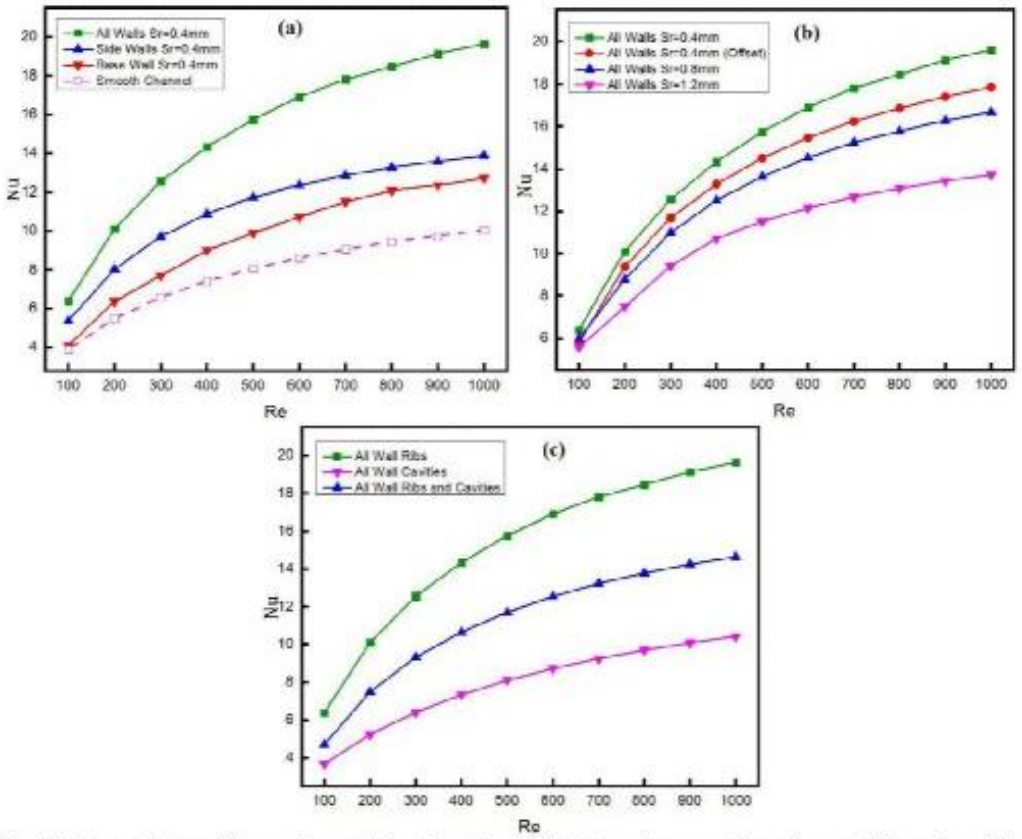

Fig. 8 Effect of Reynolds number on Nusselt number (*Nu*), for various configurations of ribs and cavities

The introduction of ribs and cavities in the channel improves the rate of heat transfer as shown in Fig. 8. The comparison of ribs on different wall configurations is shown in Fig. 8 (a). It is clearly shown that the MCHS with all wall ribs ($S_r = 0.4$mm) has the highest value of Nusselt number because of its largest surface area and the higher flow disturbances, which can be seen in Fig. 7 in terms of friction factor. Moreover, it can be seen from Fig. 8 (b) that the Nusselt number increases with the decrease in rib spacing and vice versa. Fig. 8 (c) compares the Nusselt number of ribs and cavities. It can be examined that the sole effect of cavity on friction factor and Nusselt number is negligible, but it gives better results when used in combination with ribs.

The overall performance of MCHS can be evaluated in terms of thermal enhancement factor (η), which accounts for both the heat transfer and pressure drop. It can be seen from Fig. 9 that the thermal enhancement factor for all configurations is less than unity, thus indicating that the negative effect of pressure drop occurred because of ribs dominates the positive effect of heat transfer improvement. Although the Nusselt number is higher for all wall ribs, but it has a lower value of η than base and side wall ribs as shown in Fig.9 (a). The effect of rib spacing on η has been plotted in Fig. 9 (b), which shows that the increase in rib spacing increases the thermal enhancement factor. Moreover, Fig. 9 (c) shows the comparison of ribs and cavities in which the cavities obtain the value of η nearly equal to 1, because the cavity neither increases the pressure drop nor the Nusselt number.

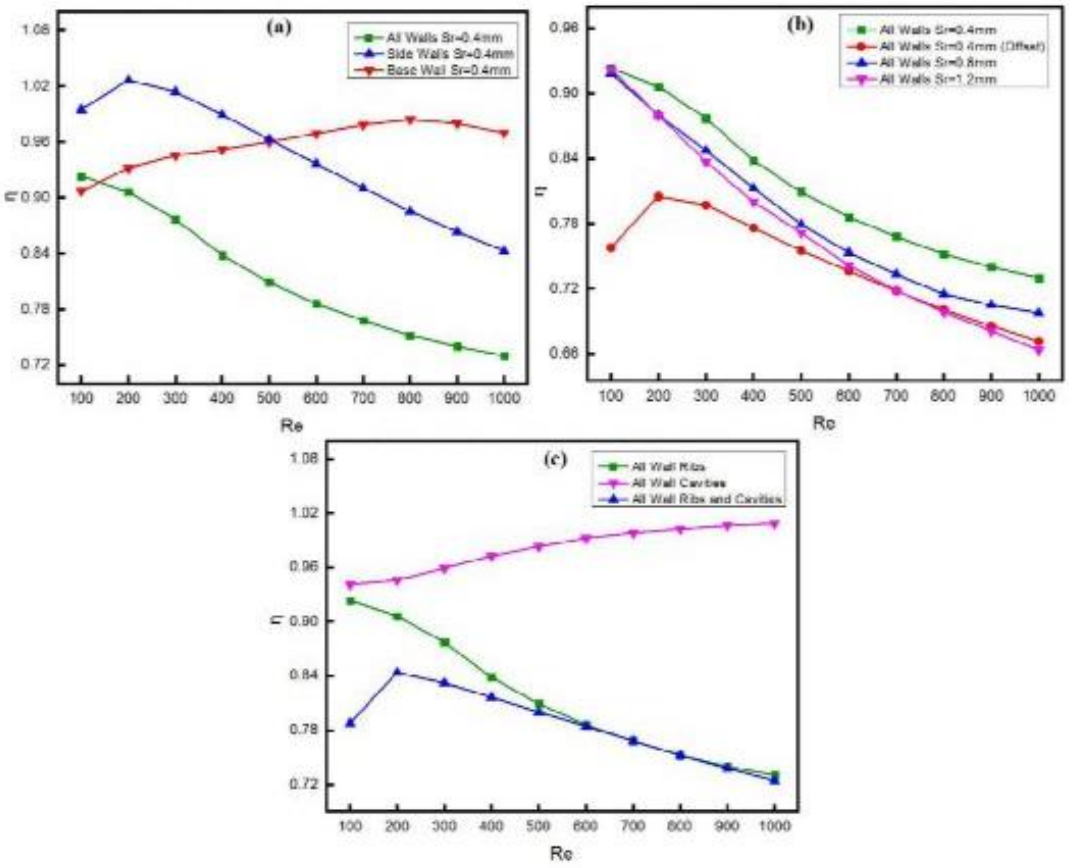

Fig. 9 Effect of Reynolds number on thermal enhancement factor for various configurations of ribs and cavities

4 CONCLUSIONS

1. The sole effect of cavity is negligible on the flow and heat transfer characteristics, but the use of cavity with the combination of ribs helps in reducing the high pressure drop occurred because of ribs.
2. The staggered condition is not helpful in the present study, because it increases the friction factor with decrease in Nusselt number, thus leading to a lower thermal enhancement factor.
3. The application of turbulence promoters (ribs and cavities) leads to a better rate of heat transfer, but at the same time, it increases the pressure drop very significantly. Although each configuration in the present study achieves a better enhancement in Nusselt number, but none of these configurations achieve the thermal enhancement factor of 1. It is because of the fact that improvement in Nusselt number is unable to compensate the high pressure drop in the present study. So, more focus needs to be given to improve the thermal enhancement factor of the present configuration, which can be recommended as a future research.
4. Since the thermal enhancement factor is based on the first law of thermodynamics, so it gives only quantitative analysis. For qualitative analysis, the method of entropy generation and exergy analysis should be done to compare the present cases on the basis of second law of thermodynamics.

ACKNOWLEDGEMENT

The authors acknowledge the support of Interdisciplinary Engineering, Modelling and Simulation Research Group (IEMSRG) of Ghulam Ishaq Khan Institute of Engineering Sciences and Technology, Topi, 23460, KPK, Pakistan.

REFERENCES

[1] D. B. Tuckerman, R. F. W. Pease, High-performance heat sinking for VLSI, IEEE Electron device letters, 2(5), 126-129, 1981.

[2] J. Hongqi, Z. Li, N. Yuxi, Z. Junjie, L. Suping, M. Xiaoyu, Design and simulation of a novel high-efficiency cooling heat-sink structure using fluid-thermodynamics, Journal of Semiconductors, 36(10), 102006, 2015.

[3] H. Wang, Z. Chen, J. Gao, Influence of geometric parameters on flow and heat transfer performance of micro-channel heat sinks, Applied Thermal Engineering, 107, 870-879, 2016.

[4] A. Dewan, P. Srivastava, A review of heat transfer enhancement through flow disruption in a microchannel, Journal of Thermal Science, 24(3), 203-214, 2015.

[5] A. Abdollahi, R. N. Sharma, H. A. Mohammed, A. Vatani, Heat transfer and flow analysis of Al2O3-Water nanofluids in interrupted microchannel heat sink with ellipse and diamond ribs in the transverse microchambers, Heat Transfer Engineering, 39(16), 1461-1469, 2018.

[6] Y. Li, G. D. Xia, D. Ma, Y. Jia, J. Wang, Characteristics of laminar flow and heat transfer in microchannel heat sink with triangular cavities and rectangular ribs, International Journal of Heat and Mass Transfer, 98, 17-28, 2016.

[7] P. Li, Y. Luo, D. Zhang, Y. Xie, Flow and heat transfer characteristics and optimization study on the water-cooled microchannel heat sinks with dimple and pin-fin, International Journal of Heat and Mass Transfer, 119, 152-162, 2018.

[8] A. G. Fedorov, R. Viskanta, Three-dimensional conjugate heat transfer in the microchannel heat sink for electronic packaging, International Journal of Heat and Mass Transfer, 43(3), 399-415, 2000.

[9] A. Abdoli, G. Jimenez, G. S. Dulikravich, Thermo-fluid analysis of micro pin-fin array cooling configurations for high heat fluxes with a hot spot, International Journal of Thermal Sciences, 90, 290-297, 2015.

[10] G. Wang, D. Niu, F. Xie, Y. Wang, X. Zhao, G. Ding, Experimental and numerical investigation of a microchannel heat sink (MCHS) with micro-scale ribs and grooves for chip cooling, Applied Thermal Engineering, 85, 61-70, 2015.

[11] A. A. Khan, S. M. Kim, K. Y. Kim, Performance Analysis of a microchannel heat sink with various rib configurations, Journal of Thermophysics and Heat Transfer, 30(4), 782-790, 2015.

[12] G. Xia, L. Chai, H. Wang, M. Zhou, Z. Cui, Optimum thermal design of microchannel heat sink with triangular reentrant cavities, Applied Thermal Engineering, 31(6-7), 1208-1219, 2011.

[13] I.A. Ghani, N. Kamaruzaman, N.A.C. Sidik, Heat transfer augmentation in a microchannel heat sink with sinusoidal cavities and rectangular ribs, International Journal of Heat and Mass Transfer, 108, 1969-1981, 2017.

[14] Y. Li, G. D. Xia, Y. Jia, D. Ma, B. Cai, J. Wang, Effect of geometric configuration on the laminar flow and heat transfer in microchannel heat sinks with cavities and fins, Numerical Heat Transfer, Part A: Applications, 71(5), 528-546, 2017.

[15] R. L. Webb, Performance evolution criteria for use of enhanced heat exchanger surfaces in heat exchanger design, Int. J. Heat Mass Transfer 24, 715–726, 1981.

STUDY OF THE EFFECT OF CONFLUENCE ANGLE ON MIXING QUALITY IN MICROMIXERS USING CFD

Urooj Fatima[1], M. Shakaib[2*], Inayatullah Memon[1]
[1] Chemical Engineering Department, NED University of Engineering & Technology, Karachi, Pakistan
[2]Mechanical Department, NED University of Engineering & Technology, Karachi, Pakistan

[*]Corresponding author. Tel.: 92 21 99261261 x 2334;
E-mail address: mshakaib@neduet.edu.pk

ABSTRACT

Three dimensional numerical simulations were performed on three micro-channels with varying confluence angles to study the effect of angle of confluence, Reynolds number and flow rate ratio on flow dynamics and mixing characteristics. Appropriate combination of angle of confluence, Reynolds number and flow rate ratio can increase the mixing quality. The results indicate that decreasing the angle of confluence and increasing the Reynolds number and flow rate ratio increases the mixing quality.

Keywords: Micromixer; mixing quality; CFD

1 INTRODUCTION

Some of the significant applications of micro-channels are that, using fuel cell technology, they are used to manufacture electronic devices [1] and they are also used in the design of microreactors. Large area-to-volume ratio with considerably enhanced heat and mass transfer are only a few incentives for rampant research work of micromixer technology.

In a micromixer fluid from two or multiple entrances are mixed together and are diverted to the mixing channel. Laminar flow conditions are prevalent which limit mixing by diffusion only. However [2] highlighted mixing can be enhanced by vortex formation even at low Renoylds number in micromixers since three laminar flow regimes are possible namely stratified regime, vortex regime and engulfment regime.

Several studies have been done to study the effect of channel geometry, angle of confluence, bent and spatial arrangements of channel to improve the mixing performance [3-7]. Furthermore studies comprising of variation in flow rate in a T type micromixer was carried by [8-9]. In this paper, we carry out CFD modelling to study the effect of angle of confluence, Reynolds number and flow rate ratio on mixing quality.

2 MODELLING PROCEDURE

Simulations were performed for three microchannel angles 120°, 150° and 180° and the effect of various volumetric flow rates were examined on mixing quality. Figure 1 shows the microchannel geometry for one of the confluence angles. In all cases 0.85 mm was the diameter and 15 mm was the length. The tracer solution is one feed that enters the inlet channel while water was the other feed.

The 3D geometries were created in ANSYS Workbench and for modelling FLUENT software was used. Steady state condition and laminar flow was considered for the simulations. Constant inlet velocities and Newtonian fluids were two assumptions that were taken. Horizontal placement of channels ensures that gravity effect can be ignored. The initial gauge pressure was 0 Pa and the temperature was 300 K.

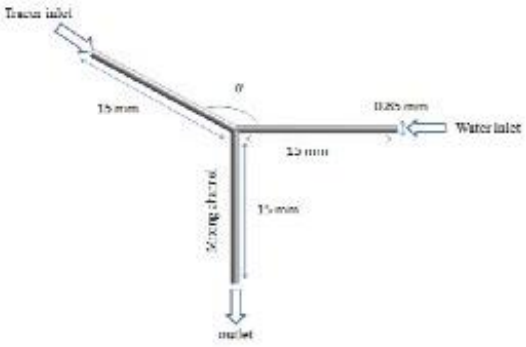

Figure 1. Schematic view of microchannels

For meshing, the domain was separated into two volumes. In total mesh contained 8.5 x10^5 control volumes.

Laminar model and species transport without reaction were applied. Velocity inlet was the boundary condition set for inlets and pressure outlet was the boundary condition set for outlet. The standard SIMPLE algorithm was used in solution controls. The second order upwind scheme was used for mass transfer and momentum. The convergence plot is shown in Figure 2.

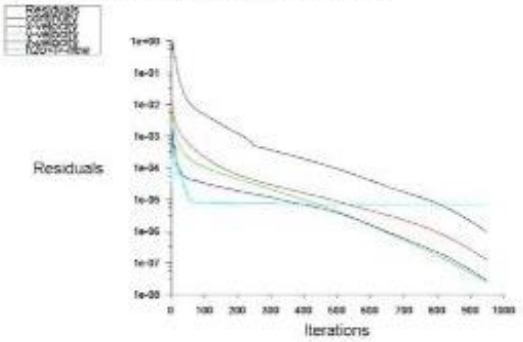

Figure 2. Residuals versus iterations

3 PARAMETERS

3.1 Mixing quality

Mixing quality is defined as follows:

$$\alpha = 1 - \sqrt{\frac{\sigma^2}{\sigma_{max}{}^2}} \qquad (1)$$

According to Equation (1), α=0 means no mixing is taking place and the two fluids are segregated. α=1 means mixing is complete.

3.2 Flow rate ratio

Due to the various confluence angles used for microchannel geometries the inlet volumetric flow rate ratios significantly affects the mixing quality. Therefore, for different confluence angles, flow rate of one of the inlets was varied and its effect on mixing quality was examined. The formula for flow:

$$R = \frac{Q_{water}}{Q_{tracer}} \qquad (2)$$

where Q_{water} is the flow rate of water and Q_{tracer} is the flow rate of tracer solution. The water inlet velocity was set as 0.15 m/s and the tracer inlet velocity used was 0.05 m/s and 0.15 m/s. The corresponding flow rate ratios are R=3 and R=1.

4 RESULTS AND DISCUSSION

Figure 3 shows the CFD predicted contours of concentration of water and velocity at R=1 for different confluence angles. At the outlet, the value of Reynolds number was 255. The generated vortices enhance mixing. Two vortices that are symmetrical to each other are formed near the periphery of the mixing channel for T shaped channel while for 120° and 150° confluence angles asymmetrical vortex is formed at the right side of the mixing channel. The formation of asymmetrical vortex is the most probable reason for more efficient mixing with decrease in confluence angle.

The mixing qualities as a function of distance for different confluence angles for flow rate ratios R=1 and R=3 are displayed in Figure 4. For both flow rate ratios microchannel with confluence angle 120° has the highest mixing quality and the microchannel with confluence angle 180° has the lowest mixing quality. In order to understand this trend Figure 5 and Figure 6 shows water concentration contours at outlet cross section and velocity vectors at x=1mm . Four small vortices at R=1 are formed for confluence angle 150° and 180° while two vortices are produced for 120°. Mixing occurs by diffusion only at the interface of fluids in

this case. In case of R=3 two large vortices are produced which spreads the fluid from the centre towards the periphery of the channel which

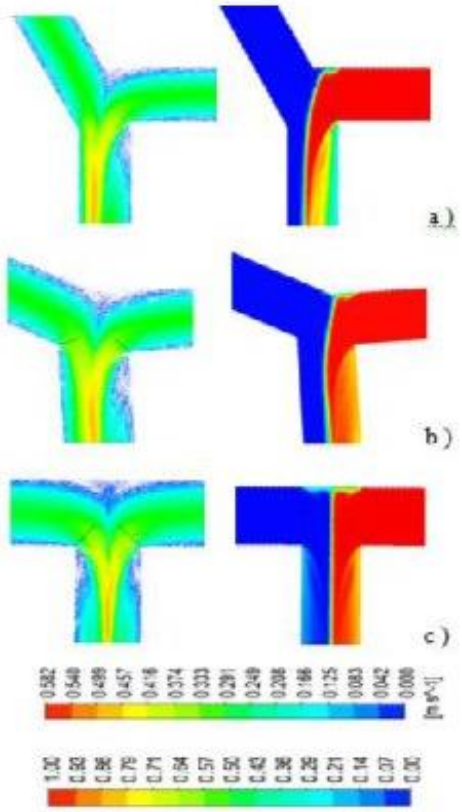

Figure 3. Flow patterns and concentration contours at various angles (a) θ=120°, (b) θ=150°and (c) θ=180°.

means mass transfer not only occurs due to diffusion but due to convection dominant mixing mechanisms.

According to a study [2] for a rectangular shaped cross section it was found for Reynolds number less than 200 an increase in mixing quality reaches up to 28%.

At Re = 255, which has been used in this study, the T shaped channel mixing quality is 22.6 %. The slight difference may be attributed to the difference in hydraulic diameter and geometry of mixing channel.

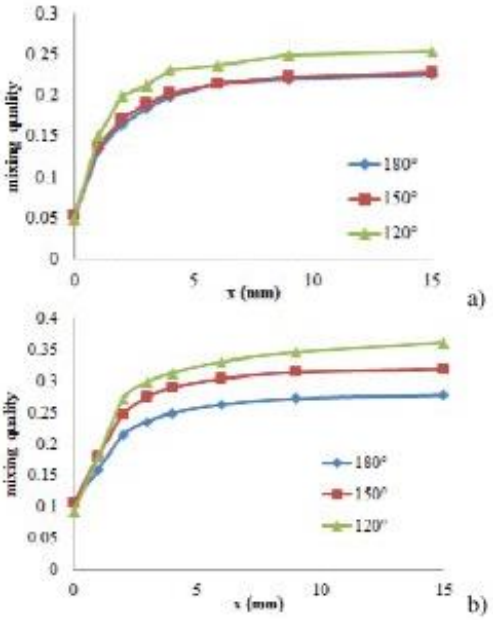

Figure 4. Mixing quality as a function of position at (a) R=1 and (b) R=3

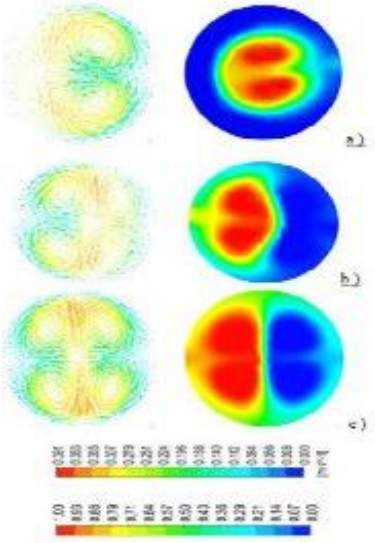

Figure 5. Velocity vectors and concentration contours of water (kmol/m^3) at R=1 for various confluence angles θ (a) θ=120°,(b) θ=150°and (c) θ=180

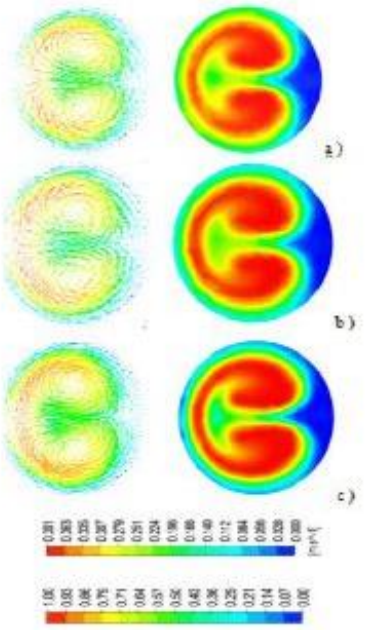

Figure 6. Velocity vectors and concentration contours of water (kmol/m^3) at R=3 for various confluence angles θ (a) θ=120°,(b) θ=150°and (c) θ=180°.

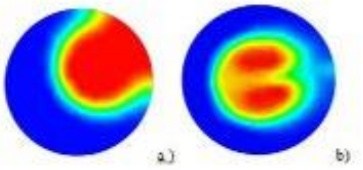

Figure 7. Concentration contours of water (kmol/m^3) at Re=85 and Re=255 for confluence angles θ=120°

The effect of Reynolds number is also studied. Increasing Re from 85 to 255 results in increase in mixing quality for all confluence angles. For Re=85 the flow is stratified flow and mixing is due to diffusion only whereas for Re=255 the flow is in engulfment regime and convection dominant mechanisms promote mixing as shown in Figure 7.

5 CONCLUSION

CFD modelling is used to study mixing in three different shape micromixers. The effect of flow rate, Reynolds number and confluence angle on mixing quality was studied. In general 120° shaped channel has the best performance than other micro-channels and mixing worsened when confluence angle gets closer to 180°. Increase in mixing quality for 120° shaped channel is observed for increase in the Reynolds number and flow rate ratio. Future work will include study on a wider range of confluence angle, Renoylds number and flow rate ratio.

ACKNOWLEDGEMENTS

The authors acknowledge the support provided by the NED University for this work.

REFERENCES

[1] Kothare MV, "Dynamics and control of integrated microchemical systems with application to micro-scale fuel processing" *Comput Chem Eng* , 30,1725–34, 2006.

[2] Engler M, Kockmann N, Kiefer T, Woias P. "Numerical and experimental investigations on liquid mixing in static micromixers.", *Chem Eng J* ,101, 315–22, 2004.

[3] Nobuaki Aoki, RyotaUmei, Atsufumi Yoshida, Kazuhiro Mae, "Design method for micromixers considering influence of channel confluence and bend on diffusion length", *Chemical Engineering Journal* , 167, 643–650, 2011.

[4] Masoud Rahimi, Mona Akbari, Mohammad Amin Parsamoghadam, Ammar Abdulaziz Alsairafi, "CFD study on effect of channel confluence angle on fluid flow pattern in asymmetrical shaped microchannels", *Computers and Chemical Engineering* ,73, 172-182, 2015.

[5] Nobuaki Aoki, Takashi Fukuda, Norihide Maeda, Kazuhiro Mae, "Design of confluence and bend geometry for rapid mixing in microchannels", *Chemical Engineering Journal* , 227, 198–202, 2013.

[6] Masoud Rahimi ,Neda Azimi , Mohammad Amin Parsamogadam, Alireza Rahimi, Mohammad Moein Masahy, "Mixing performance of T, Y, and oriented Y-micromixers with spatially arranged outlet channel evaluation with Villermaux/

Dushman test reaction", *Microsyst Technol*, 23 ,3117–3130, 2017.

[7] Kashid M, Renken A, Kiwi-Minsker L, "Mixing efficiency and energy consumption for five generic microchannel designs", *Chem Eng J* ,167,436–43, 2011.

[8] A. Soleymani, E. Kolehmainen, I. Turunen, "Numerical and experimental investigations of liquid mixing in T-type micromixers" , *Chemical Engineering Journal,* 135S , S219–S228, 2008

[9] C.A. Cortes-Quiroz, A. Azarbadegan, M. Zangeneh, "Effect of channel aspect ratio of 3-D Tmixer on flow patterns and convective mixing for a wide range of Reynolds number" , *Sensors and Actuator*, B 239 ,1153-1176, 2017

THERMODYNAMIC ANALYSIS OF VACUUM MEMBRANE DISTILLATION (VMD) TO DESALINATE SEA WATER USING SOLAR ENERGY

Syed Asad Jamal [1], Muhammad Asif [1,*], Muhammad Suleman [1]

[1] Faculty of Mechanical Engineering, GIK Institute of Engineering Sciences and Technology, Topi, Pakistan.

* Corresponding author: masif@giki.edu.pk

ABSTRACT

Vacuum membrane distillation is an emerging technology for sea and brackish water desalination. In the present study, a mathematical model of heat and mass transfer for VMD is established. Physical and hydrodynamic parameters are integrated with the governing equations of heat and mass transfer. These governing equations are numerically solved using in-house coding in Mathcad. The simulation results are validated with the experimental data available in the literature. A flux sensitivity analysis is performed by considering the impact of influential operating parameters such as feed temperature, salt concentration and vacuum pressure on the performance of VMD. The detailed thermodynamic modelling and analysis of VMD process provide an optimal operating conditions and roadmap to establish economic feasibility of the process at large scale.

Keywords: desalination, heat transfer, mass transfer, solar energy, vacuum membrane distillation

1 INTRODUCTION

The earth is composed of 70% water, out of which 97% is in the oceans and seas and is not drinkable because of its salty nature [1]. The other 2% is locked in icecaps and glaciers, and the fresh water available for user accounts for less than 0.5% of the earth's total water supply [2]. Being a basic human need, the remaining fresh water is not directly accessible because it is present in the deep aquifers. Hence the scarcity of fresh water has become a global issue, and the society has arrived at the problem of shortage of drinkable water. However, the said problem may be addressed by treating the sea water and the brackish water to make it drinkable. Various techniques are available to desalinate seawater such as reverse osmosis and multi-stage flash. These techniques require higher operating and maintenance cost, and they cannot be operated using a low-grade energy source such as solar energy. An alternative to existing methods of seawater desalination is membrane distillation (MD).

MD processes possess many appealing features, especially when coupled with solar energy or low-grade heat source. Some features are; (i) low operating pressure and temperature, (ii) simple membrane construction, (iii) low energy consumption when waste heat is available, (iv) low sensitivity to salt concentration, (v) theoretically 100% salt rejection, (vi) high potential for the utilization of a low grade heat (i.e., solar energy) and (vii) no extensive pretreatment [3-7].

Membrane distillation can be classified into four types: air gap membrane distillation (AGMD), direct contact membrane distillation (DCMD), sweeping gas membrane distillation (SGMD) and vacuum membrane distillation (VMD) [8-10]. The main difference in these configurations lies in the type of condensing design (cold side) and are classified based on the way pressure-difference is created between feed and the permeate side. In DCMD, cooled permeate stream is in direct contact with the opposite side of the membrane. The condensing medium for the vapour is the permeate liquid, which cannot pass through the pores. This simple design requires only external cooling of the permeate stream. The AGMD uses an air gap on the permeate side of the membrane. The vapor which passes through the membrane pores are condensed on the cold surface. The presence of an air gap between the membrane and the condensation surface reduces the heat loss by conduction, and as a result, improved thermal efficiency compared to DCMD. However, a major disadvantage of AGMD is the high mass transfer resistance due to the air gap as it limits the permeate flux. SGMD has

received relatively little attention in the literature. In this configuration, a carrier gas is swept across the permeate side of the membrane, entraining the vapor which is condensed outside the membrane module. This is typically used where volatile vapors are being distilled, and an inert carrier gas carries the vapors to a separate condenser [11]. Another MD configuration that is similar to AGMD is the vacuum membrane distillation (VMD). The difference between the two lies in the pressure difference across the membrane. In VMD configuration, pressure is lower than the atmospheric pressure. Comparison between the MD configurations shows that VMD process involves low mass transfer resistance and can produce permeate flux at low operating temperature [12, 13].

In addition to sea and brackish water desalination, VMD is also being used for fermentation [14, 15], juice and coffee concentration in the food industry [16-24], removal of volatile organic compounds from aqueous solution [25-34], mineral recovery [35] and for regeneration of liquid desiccant air conditioning system [36, 37]. To predict the accurate permeate flux and behavior of heat and mass transfer in the VMD, a detailed integrated heat and mass transfer model is essentially required. In this study, we have developed an integrated heat and mass transfer model of VMD process. The model is solved using the in-house coding in Mathcad. The simulation results are validated with the experimental data of the previously published literature. The results obtained can be used as a guide to operate VMD at optimal operating conditions and a roadmap for large scale VMD process.

paper should be submitted on A4 (210mmx297mm) page and typed in a two-column format as shown in this manuscript template. The text should fit exactly into the type area. The correct settings of margins are illustrated in Figure 1. Page numbers should not be inserted on any page.

2 METHOLODOLOGY

2.1 Mass Transfer Model

Mass transfer in MD occurs by convective and diffusive transport of vapors across the microporous membrane. The driving force for mass transfer is the difference in water vapor pressure on either side of the membrane. Resistance to mass transfer comes from both the membrane structure and the presence of air trapped within the membrane. The resistance imposed by the membrane structure in the absence of air can be termed as frictional mass transfer resistance and can be described by either Knudsen diffusion model or the Poiseuille flow model, the latter being dominant when the membrane pore size is larger than the mean free molecular path of the gaseous water molecules [38]. As the mean free molecular path of saturated water vapor at 60°C is around 3µm (a typical MD pore size), both models must be considered. To calculate mass flux from Knudsen diffusion model following equation is used [39]:

$$J_k = 1.064\frac{r\varepsilon}{\tau\delta}\left(\frac{M}{RT_{avg}}\right)^{0.5}(P_i - P_v) \quad (1)$$

Where P_v and P_i are water vapor pressure at vacuum side and membrane-feed interface, respectively; r, δ, τ and ε are the pore size, membrane thickness, tortuosity and porosity of the membrane, respectively; and T_{avg}, R, and M are average absolute temperature in membrane pores, universal gas constant and molecular weight of water, respectively.

On the other hand for Poiseuille's flow regime the equation used is:

$$J_p = 0.125\frac{r^2\varepsilon}{\tau\delta}\left(\frac{MP_{avg}}{\eta RT_{avg}}\right)(P_i - P_v) \quad (2)$$

Where P_{avg} and η are average vapor pressure and viscosity of water vapor, respectively.

A question arises that which of these models should be used to calculate the VMD flux. Knudsen diffusion is dominant when the pore size of the porous membrane is smaller than the mean free molecular path.

Dimension less number called Knudsen number is used to specify the flow type, which is described as follows:

$$Kn = \frac{\lambda}{L} \quad (3)$$

Where λ is the mean free molecular path and L is a physical scale characteristic length [11]. In this study, the characteristic length would be the pore size of the membrane.

On the other hand, if the pore size of the membrane is greater than the mean free path, then Poiseuille's flow regime is used. In this study, membrane pore size smaller than the mean free molecular path is

adopted, so the Knudsen diffusion model is considered.

In another VMD modeling study, Lovineh et al. (2013) [40] neglected the Poiseuille's flow contribution and assumed Knudsen flow to be the dominating mass transfer mechanism. The linearity of Knudsen's flow equation along with the linear relationship confirmed experimentally [33, 41] between the water vapor mass flux and the partial pressure difference, supported by Lovineh et al. [40] modeling assumption.

2.2 Salinity equations

For calculation of flux as a dependence up on salinity following equations were used [42]:

$$J_w = \frac{K_m}{\sqrt{M_w}}\left(\alpha_w X_w P_i(T_i) - P_p\right) \quad (4)$$

where J_w, α_w, $P_i(T_i)$, M_w, K_m and P_p are the molar water flux, water activity coefficient, the partial vapor pressure at the membrane temperature, the molar mass of water, membrane Knudsen permeability coefficient, the pressure at permeate side, respectively.

$$\alpha_w = 1 - 0.5X_s - 10X_s^2 \quad (5)$$

Where X_s is the salt molar fraction.

$$K_m = \frac{2}{3}\frac{\varepsilon r}{\tau\delta RT_m}\sqrt{\frac{8RT_i}{\pi}} \quad (6)$$

2.3 Heat transfer model

For calculation of heat transfer through the membrane the following equation is used [39]:

$$Q = h(T_b - T_i) \quad (7)$$

where h, T_b, and T_i are the heat transfer coefficient, bulk-feed temperature, and membrane-interface temperature, respectively. T_b is an independent quantity whereas T_i and h are evaluated theoretically.

Calculation of heat transfer coefficient

The governing equations are coupled and solved step by step to calculate the heat transfer coefficient. Equations from [43] and [44] are used:

$$h = \frac{Nu\,k}{d_h} \quad (8)$$

Where Nu, k, and d_h are the Nusselt number, the thermal conductivity of fluid and hydraulic diameter, respectively.

$$Nu = 0.029Re^{0.8}Pr^{0.33} \quad (9)$$

Where Re and Pr are Reynold and Prandtl number, respectively.

$$Re = \rho V\frac{d_h}{\mu} \quad (10)$$

Where ρ, V and μ are the density, velocity, and viscosity of the fluid, respectively.

$$Pr = \frac{\mu C_p}{k} \quad (11)$$

Where C_p is the specific heat of fluid.

$$d_h = d_o\frac{1-\emptyset}{\emptyset} \quad (12)$$

$$\emptyset = N_f\left(\frac{d_o}{d_s}\right)^2 \quad (13)$$

Where d_o, d_s, N_f, ϕ are the outer diameter of the fiber, inner shell diameter, number of hollow fibers and module packing density of the VMD, respectively. The equations to calculate k are adopted from the reference [43].

$$\mu = \mu_w\mu_R \times 10^{-3} \quad (14)$$

$$\mu_w = exp\left(-3.79418 + \frac{604.129}{139.18 + T}\right)$$

$$\mu_R = 1 + AS + BS^2$$

$$A = 1.474 \times 10^{-3} + 1.5 \times 10^{-6}T - 3.927 \times 10^{-8}T^2$$

$$B = 1.0734 \times 10^{-5} - 8.5 \times 10^{-8}T + 2.23 \times 10^{-10}T^2$$

Where μ is in kg/ms; T: 20 < T < 180 °C and S: 0 < S < 130 g/kg.

$$C_p = A + BT + CT^2 + DT^3 \quad (15)$$

$$A = 4206.8 - 6.6197S + 1.2288 \times 10^{-2}S^2$$

$$B = -1.1262 + 5.4178 \times 10^{-2}S - 2.2719 \times 10^{-4}S^2$$

$$C = 1.2026 \times 10^{-2} - 5.3566 \times 10^{-4}S + 1.8906 \times 10^{-6}S^2$$

$$D = 6.8777 \times 10^{-7} + 1.517 \times 10^{-6}S - 4.4268 \times 10^{-9}S^2$$

Where C_p is in kJ/kg°C; T: 10 < T < 180 °C and S: 20 < S < 160 g/kg

$$\log_{10}(k_w) = \log_{10}(240 + AS) + 0.434 \times \left(2.3 - \frac{343.5 + BS}{T + 273.15}\right)\left(1 - \frac{T + 273.15}{647.3 + CS}\right)^{\frac{1}{3}} \quad (16)$$

$$k = k_w \times 10^{-3}$$

$$A = 2 \times 10^{-4}$$

$$B = 3.7 \times 10^{-2}$$

$$C = 3 \times 10^{-2}$$

Where k is in W/m K; T: 20 < T < 180°C and S: 0 < S < 160 g/kg.

Integration of mass and heat transfer model

In the VMD process, the mass and heat transfer rates are interconnected. A change in one of them induces a change in the other. According to Alsaadi et al. (2014) [39], the two rates are related by the equation:

$$J = h(T_b - T_i) = J g_v - C_m(P_i - P_p)g_v \quad (17)$$

Where g_v and C_m are enthalpy of saturated vapor and mass permeability coefficient of the membrane, respectively.
To calculate g_v, we used the following equation [43]:

$$g_v = 2501.689845 + 1.8069160157T + 5.087717 \times 10^{-4}T^2 - 1.1221 \times 10^{-5}T^3 \quad (18)$$

Where T is valid in range 0.01-200°C.

3. SOLUTION PROCEDURE

A numerical iterative method is used to solve for the value of flux using Mathcad's in-house coding.

4. RESULTS AND DISCUSSION

4.1 Validation of model

Heat transfer coefficient h calculated from equations (5) - (16) gives h = 2919 W/m^{2}K and Alsaadi et al. [39] experimentally calculated h =2800 W/m^2 K.

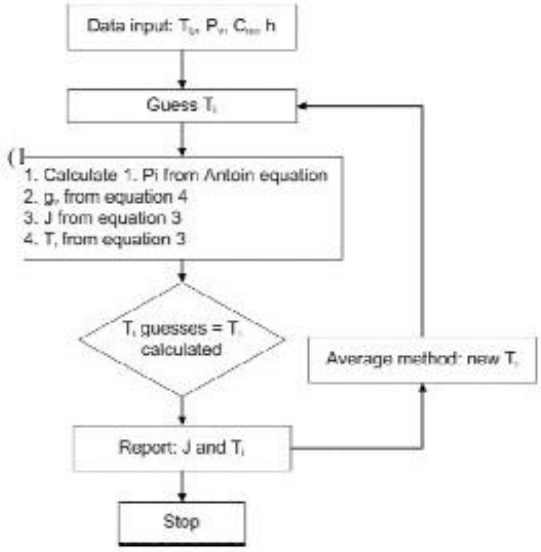

Figure 1. VMD Model iteration

Membrane properties used in the study are as follows: outer fiber diameter: 2.6 mm, shell diameter: 0.025 m, number of fibers: 40, fiber length: 0.47 m, feed inlet velocity: 0.2 ms^{-1}, inlet feed salinity: 35 g/kg. Simulation is carried out at a feed temperature of 70°C and permeate side pressure in the range of 10 kPa to 65 kPa and compared with the experimental data of the Y. Wang et al. (2015) [45]. The simulation results are in good agreement with the experimental data as shown in Figure 2.
The mathematical model of heat and mass transfer in VMD process is solved by using in-house coding in Mathcad.
Figure 1 shows the effect of inlet bulk feed temperature T_b on the VMD permeate flux with a flow rate of 2 L/min. The results indicated that the permeate flux was increased by increasing the bulk temperature of the feed. Due to temperature polarization, the interface temperature T_i will be different than T_b and would equilibrate somewhere between T_b and the saturation temperature of vacuum pressure T_{sat}. If we assume the vacuum pressure to be constant, then T_{sat} would also remain constant, and decrease the bulk temperature of feed such that it approaches T_{sat}.

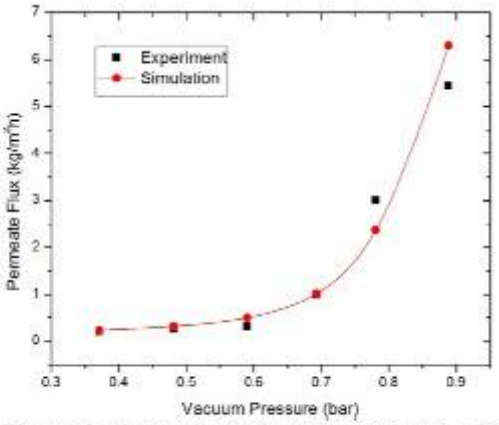

Figure 2. Comparison of results generated with experimental results of Y. Wang et al. [45]

Then, T_i will also be approaching T_{sat}, resulting in the process becoming heat transfer limited [8]. This effect is shown by the green plot that, at P_v=12kPa, T_{sat}=49.4°C, and T_b=50°C the flux is almost zero. And also, at this point, T_i will achieve a value between 49.4°C and 50 °C, and it was simulated to be 49.7°C.

Vacuum pressure is applied to the permeate side of the VMD. Figure 2 shows the effect of vacuum pressure on the permeate flux with a flow rate of 2 L/min. As we increase the vacuum pressure the permeate flux decreases. An increase in vacuum pressure means an increase in saturation temperature, now depending on the value of T_b, T_i will equilibrate between T_b and T_{sat}, and thus the operable range of VMD would vary. If we simulate VMD at a different value of T_b the value of permeate flux changes as well. We achieved maximum permeate flux at higher value of T_b and lowest value of P_v. The results indicated that at feed temperature of 80°C, and vacuum pressure of 34 abs kPa, the permeate flux reaches up to 15.23 kg/h·m^2.

Figure 3 shows the variation in permeate flux (J) and interface temperature (T_i) with pressure difference across the membrane (ΔP). It illustrates how T_i at equilibrium affects the flux of a VMD process operating at constant P_v and at constant T_b. Pressure difference across the membrane is the driving force and plays a vital role in the transfer of molecules across the membrane, and this pressure difference is dependent on the temperature difference. As the mass transfer process occurs through the membrane interface, it is at the temperature of the interface. That is why for mass transfer to occur, P_i should be greater than P_v and thus T_i to be greater than T_{sat}. As T_i would be less than T_b, it will equilibrate some between the two. If T_i approaches toward T_{sat}, permeate flux approaches zero as the difference between P_i and P_v approaches zero and according to Alsaadi et al. [8], the process becomes heat transfer limited. If T_i approaches toward T_b, meaning that no temperature polarization occurs, then VMD flux would be limited by C_m. Changing the value of C_m by using a different membrane would result in a different value of VMD flux.

Figure 4 shows how the flux is affected by the salt concentration of the bulk feed at P_v=20 kPa and a flow rate of 2 L/min. By increasing the salt concentration of the feed VMD flux decreases until it reaches a steady value and does not further decrease.

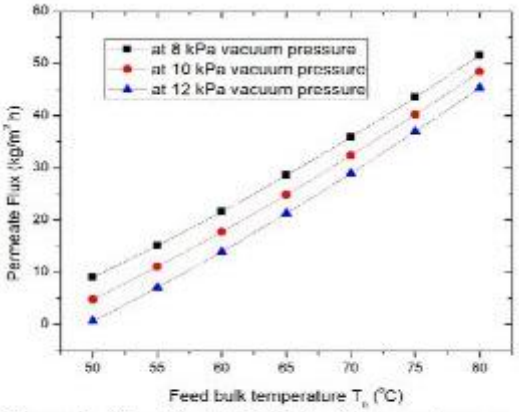

Figure 3. The effect of Bulk feed temperature on permeate flux.

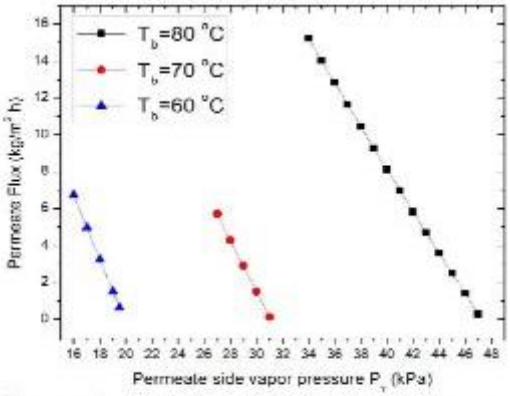

Figure 4. The effect of vacuum pressure on permeate flux

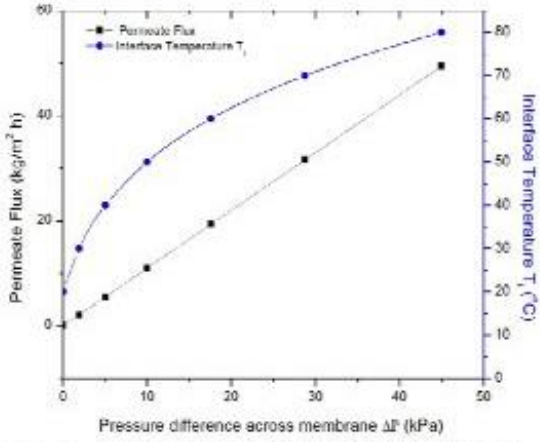

Fig. 5. Variation of J (permeate flux) and T_i (interface temperature) with ΔP (pressure difference across the membrane).

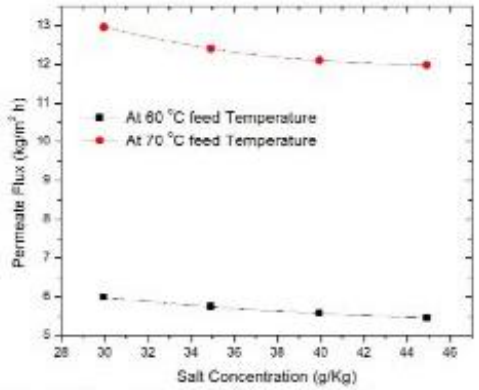

Fig. 6. The effect of salt concentration on permeate flux.

5. CONCLUSION

A theoretical analysis of VMD process was carried out with the aim of studying mass transfer phenomenon in the VM distillation. A simple 1-D model was used for mathematical modeling, and the influence of feed temperature, feed concentration and vacuum side pressure on the permeate flux were studied for brackish water (18 ppt) and sea water (40 ppt). The results showed an increase in VMD flux with an increase in feed bulk temperature and consequently a decrease in VMD flux with an increase in permeate side vacuum pressure and salt concentration of the feed. The simulated results closely matched with experimental data.

Furthermore, the following conclusions can be drawn based on this study: salt concentration has the least effect on the VMD flux as compared to bulk feed temperature or permeates side pressure. There is a specific operating range of permeate flux for a fixed bulk feed temperature. The operating vacuum pressure range changes if the inlet bulk feed temperature is changed and VMD flux reaches a zero value if the interface temperature of the membrane and the saturation temperature of vacuum pressure are the same. Highest VMD flux is achieved at lowest permeate pressure and highest bulk feed temperature.

ACKNOWLEDGEMENTS

The authors would like to thank Higher Education Commission (HEC), Govt. of Pakistan for the financial support in the form of NRPU # 5550 and Ghulam Ishaq Khan Institute of Engineering Sciences and Technology for providing support during the preparation of this work.

REFERENCES

References

[1] O. Institute. (2018). *Aqua Facts: How much of the earth is water?. https://www.oceanicinstitute.org/aboutoceans/aquafacts.html. Accessed on 8th November 2018.*

[2] NOAA. (2018). *How much water is in the ocean?. https://oceanservice.noaa.gov/facts/oceanwater.html; Accessed on 30 October 2018.* .

[3] K. W. Lawson and D. R. Lloyd, "Membrane distillation," *Journal of membrane Science,* vol. 124, pp. 1-25, 1997.

[4] M. El-Bourawi, Z. Ding, R. Ma, and M. Khayet, "A framework for better understanding membrane distillation separation process," *Journal of membrane science,* vol. 285, pp. 4-29, 2006.

[5] S. Al-Obaidani, E. Curcio, F. Macedonio, G. Di Profio, H. Al-Hinai, and E. Drioli, "Potential of membrane distillation in seawater desalination: thermal efficiency, sensitivity study and cost estimation," *Journal of Membrane Science,* vol. 323, pp. 85-98, 2008.

[6] L.-H. Cheng, Y.-H. Lin, and J. Chen, "Enhanced air gap membrane desalination by novel finned tubular membrane modules," *Journal of membrane science,* vol. 378, pp. 398-406, 2011.

[7] H. Maab, L. Francis, A. Al-Saadi, C. Aubry, N. Ghaffour, G. Amy, *et al.*, "Synthesis and

fabrication of nanostructured hydrophobic polyazole membranes for low-energy water recovery," *Journal of membrane science,* vol. 423, pp. 11-19, 2012.

[8] M. Bahrami, J. Karimi-Sabet, A. Hatamnejad, A. Dastbaz, and M. A. Moosavian, "Optimization and modification of PVDF dual-layer hollow fiber membrane for direct contact membrane distillation; application of response surface methodology and morphology study," *Korean Journal of Chemical Engineering,* vol. 35, pp. 2241-2255, 2018.

[9] B.-G. Im, J.-G. Lee, Y.-D. Kim, and W.-S. Kim, "Theoretical modeling and simulation of AGMD and LGMD desalination processes using a composite membrane," *Journal of Membrane Science,* vol. 565, pp. 14-24, 2018.

[10] M. Safavi and T. Mohammadi, "High-salinity water desalination using VMD," *Chemical Engineering Journal,* vol. 149, pp. 191-195, 2009.

[11] S. Shukla, J. Méricq, M. Belleville, N. Hengl, N. Benes, I. Vankelecom, *et al.*, "Process intensification by coupling the Joule effect with pervaporation and sweeping gas membrane distillation," *Journal of membrane science,* vol. 545, pp. 150-157, 2018.

[12] R. B. Saffarini, E. K. Summers, and H. A. Arafat, "Technical evaluation of stand-alone solar powered membrane distillation systems," *Desalination,* vol. 286, pp. 332-341, 2012.

[13] X. Chen, X. Gao, K. Fu, M. Qiu, F. Xiong, D. Ding, *et al.*, "Tubular hydrophobic ceramic membrane with asymmetric structure for water desalination via vacuum membrane distillation process," *Desalination,* vol. 443, pp. 212-220, 2018.

[14] E. Hoffmann, D. Pfenning, E. Philippsen, P. Schwahn, M. Sieber, R. Wehn, *et al.*, "Evaporation of alcohol/water mixtures through hydrophobic porous membranes," *Journal of membrane science,* vol. 34, pp. 199-206, 1987.

[15] N. Qureshi, M. Meagher, and R. Hutkins, "Recovery of 2, 3-butanediol by vacuum membrane distillation," *Separation science and technology,* vol. 29, pp. 1733-1748, 1994.

[16] Y. Wu, Y. Wei, J. Liu, and J. Xu, "An experimental-study on membrane distillation for treatment of ginseng dew and ginseng washing water," *CHINESE SCIENCE BULLETIN,* vol. 34, pp. 640-644, 1989.

[17] Z.-P. Zhao, F.-W. Ma, W.-F. Liu, and D.-Z. Liu, "Concentration of ginseng extracts aqueous solution by vacuum membrane distillation. 1. Effects of operating conditions," *Desalination,* vol. 234, pp. 152-157, 2008.

[18] Z.-P. Zhao, C.-Y. Zhu, D.-Z. Liu, and W.-F. Liu, "Concentration of ginseng extracts aqueous solution by vacuum membrane distillation 2. Theory analysis of critical operating conditions and experimental confirmation," *Desalination,* vol. 267, pp. 147-153, 2011.

[19] R. Bagger-Jørgensen, A. S. Meyer, M. Pinelo, C. Varming, and G. Jonsson, "Recovery of volatile fruit juice aroma compounds by membrane technology: Sweeping gas versus vacuum membrane distillation," *Innovative Food Science & Emerging Technologies,* vol. 12, pp. 388-397, 2011.

[20] R. Bagger-Jørgensen, A. S. Meyer, C. Varming, and G. Jonsson, "Recovery of volatile aroma compounds from black currant juice by vacuum membrane distillation," *Journal of Food Engineering,* vol. 64, pp. 23-31, 2004.

[21] N. Diban, O. C. Voinea, A. Urtiaga, and I. Ortiz, "Vacuum membrane distillation of the main pear aroma compound: Experimental study and mass transfer modeling," *Journal of Membrane Science,* vol. 326, pp. 64-75, 2009.

[22] A. Hasanoğlu, F. Rebolledo, A. Plaza, A. Torres, and J. Romero, "Effect of the operating variables on the extraction and recovery of aroma compounds in an osmotic distillation process coupled to a vacuum membrane distillation system," *Journal of food engineering,* vol. 111, pp. 632-641, 2012.

[23] Y.-R. Chen, L.-H. Chen, C.-H. Chen, C.-C. Ko, A. Huang, C.-L. Li, *et al.*, "Hydrophobic alumina hollow fiber membranes for sucrose concentration by vacuum membrane distillation," *Journal of Membrane Science,* vol. 555, pp. 250-257, 2018.

[24] A. Criscuoli and E. Drioli, "Vacuum membrane distillation for the treatment of coffee products," *Separation and Purification Technology,* vol. 209, pp. 990-996, 2019/01/31/ 2019.

[25] F. A. Banat and J. Simandl, "Removal of benzene traces from contaminated water by vacuum membrane distillation," *Chemical Engineering Science,* vol. 51, pp. 1257-1265, 1996.

[26] N. Couffin, C. Cabassud, and V. Lahoussine-Turcaud, "A new process to remove halogenated VOCs for drinking water production: vacuum membrane distillation," *Desalination,* vol. 117, pp. 233-245, 1998.

[27] Z. Jin, S. H. Zhang, and X. G. Jian, "Removal of 2, 4-dichlorophenol from wasterwater by vacuum membrane distillation using hydrophobic PPESK hollow hiber membrane," *Chinese Chemical Letters,* vol. 18, pp. 1543-1547, 2007.

[28] G. Sarti, C. Gostoli, and S. Bandini, "Extraction of organic components from aqueous streams by vacuum membrane distillation," *Journal of Membrane Science,* vol. 80, pp. 21-33, 1993.

[29] J.-j. Tang, K.-g. Zhou, Q.-x. Zhang, and Q.-g. Li, "Study on the removal of MIBK from aqueous solution by vacuum membrane distillation," *Journal of Central South University of Technology,* vol. 7, pp. 178-181, 2000.

[30] A. Urtiaga, E. Gorri, G. Ruiz, and I. Ortiz, "Parallelism and differences of pervaporation and vacuum membrane distillation in the removal of VOCs from aqueous streams," *Separation and Purification Technology,* vol. 22, pp. 327-337, 2001.

[31] A. Urtiaga, G. Ruiz, and I. Ortiz, "Kinetic analysis of the vacuum membrane distillation of chloroform from aqueous solutions," *Journal of Membrane Science,* vol. 165, pp. 99-110, 2000.

[32] B. Wu, X. Tan, K. Li, and W. Teo, "Removal of 1, 1, 1-trichloroethane from water using a polyvinylidene fluoride hollow fiber membrane module: Vacuum membrane distillation operation," *Separation and Purification Technology,* vol. 52, pp. 301-309, 2006.

[33] B. Wu, X. Tan, W. Teo, and K. Li, "Removal of benzene/toluene from water by vacuum membrane distillation in a PVDF hollow fiber membrane module," *Separation science and technology,* vol. 40, pp. 2679-2695, 2005.

[34] R. Baghel, S. Upadhyaya, S. P. Chaurasia, K. Singh, and S. Kalla, "Optimization of process variables by the application of response surface methodology for naphthol blue black dye removal in vacuum membrane distillation," *Journal of Cleaner Production,* vol. 199, pp. 900-915, 2018.

[35] Z. Cui, Y. Zhang, X. Li, X. Wang, E. Drioli, Z. Wang, *et al.*, "Optimization of novel composite membranes for water and mineral recovery by vacuum membrane distillation," *Desalination,* vol. 440, pp. 39-47, 2018.

[36] J. Zhou, X. Zhang, B. Sun, and W. Su, "Performance analysis of solar vacuum membrane distillation regeneration," *Applied Thermal Engineering,* vol. 144, pp. 571-582, 2018.

[37] R. Lefers, N. M. S. Bettahalli, N. Fedoroff, S. P. Nunes, and T. Leiknes, "Vacuum membrane distillation of liquid desiccants utilizing hollow fiber membranes," *Separation and Purification Technology,* vol. 199, pp. 57-63, 2018.

[38] R. Schofield, A. Fane, and C. Fell, "Heat and mass transfer in membrane distillation," *Journal of Membrane Science,* vol. 33, pp. 299-313, 1987.

[39] A. S. Alsaadi, L. Francis, G. L. Amy, and N. Ghaffour, "Experimental and theoretical analyses of temperature polarization effect in vacuum membrane distillation," *Journal of Membrane Science,* vol. 471, pp. 138-148, 2014.

[40] S. G. Lovineh, M. Asghari, and B. Rajaei, "Numerical simulation and theoretical study on simultaneous effects of operating parameters in vacuum membrane distillation," *Desalination,* vol. 314, pp. 59-66, 2013.

[41] I. Wangnick Consulting, "2002 IDA Worldwide desalting plants inventory report No. 17," International Desalination Association, Gnarrenburg, Germany2002.

[42] Z. Trikia, M. Bouaziza, and M. Boumazab, "On the use of solar vacuum membrane distillation as an integrated desalination process for the treatment of reverse osmosis brines: A case study from the south of Algeria."

[43] A. S. Alsaadi, N. Ghaffour, J.-D. Li, S. Gray, L. Francis, H. Maab, *et al.*, "Modeling of air-gap membrane distillation process: A theoretical and experimental study," *Journal of membrane science,* vol. 445, pp. 53-65, 2013.

[44] Y.-D. Kim, K. Thu, and S.-H. Choi, "Solar-assisted multi-stage vacuum membrane distillation system with heat recovery unit," *Desalination,* vol. 367, pp. 161-171, 2015.

[45] Y. Wang, Z. Xu, N. Lior, and H. Zeng, "An experimental study of solar thermal vacuum membrane distillation desalination," *Desalination and Water Treatment,* vol. 53, pp. 887-897, 2015/01/23 2015.